Report No. FRA-OR&D 75-94

CONCRETE TUNNEL LINERS

STRUCTURAL TESTING OF CAST-IN-PLACE LINERS

AUGUST, 1975

FINAL REPORT

Prepared for

Department of Transportation
FEDERAL RAILROAD ADMINISTRATION
Washington, D.C. 20590

NOTICE

Technical Report Documentation Page

1. Report No.	2. Government Accession No.	3. Recipient's Catalog No.
FRA OR&D 75-94		

4. Title and Subtitle	5. Report Date
CONCRETE TUNNEL LINERS: STRUCTURAL TESTING OF CAST-IN-PLACE LINERS	August 1975
	6. Performing Organization Code
7. Author(s)	8. Performing Organization Report No.
S. L. Paul and R. A. Ferrera-Boza	UILU ENG-75-2014
9. Performing Organization Name and Address	10. Work Unit No. (TRAIS)
Department of Civil engineering University of Illinois at Urbana-Champaign Urbana, Illinois 61801	11. Contract or Grant No. DOT FR 30022
	13. Type of Report and Period Covered Aug. 1974 - Aug. 1975 Final Report
12. Sponsoring Agency Name and Address Federal Railroad Administration Department of Transportation Washington, D. C. 20590	14. Sponsoring Agency Code

15. Supplementary Notes

16. Abstract

A series of 4 tests on circular steel-fiber-reinforced concrete tunnel liners without conventional bar reinforcement is described. The specimens simulate cast-in-place liners made by a slipform system, and were 10 ft (3.05 m) OD and had a 6-in. (152 mm) uniform thickness. Radial loads were applied with hydraulic rams at 12 equally spaced locations around the liner with some rams active and some passive to represent active ground loads above a tunnel and lateral resistance on the sides. Rams that represented the passive soil resistance were given a predetermined load-deflection relationship. Overall deformability, distribution of loads around the specimens and computed internal forces are presented for the tests.

A computer program that will calculate the moment-thrust-curvature relations for a concrete section taking into account the nonlinear character of the compression and tension stress-strain behavior was written and used to obtain the moment-thrust failure envelope. For this analysis it was necessary to determine the compression and flexural tension stress-strain curves for steel-fiber-reinforced concrete, and these curves and the technique used to obtain them are described. These studies are preliminary to development of an analysis that will take into account the nonlinear character of the liner due to material behavior and geometry change and that will predict ultimate load.

17. Key Words	18. Distribution Statement
Tunnel Liners, Liner Tests, Steel-Fiber Concrete, Liner Analysis	Document is available to the public through the National Technical Information Service, Springfield, VA 22151

19. Security Classif. (of this report)	20. Security Classif. (of this page)	21. No. of Pages	22. Price
Unclassified	Unclassified	119	

Form DOT F 1700.7 (8-72) Reproduction of completed page authorized

PREFACE

Research described in this report was performed by the Department of Civil Engineering at the University of Illinois at Urbana-Champaign, Urbana, Illinois from August 1974 to August 1975. The project was sponsored by the Federal Railroad Administration, Department of Transportation, through contract No. DOT FR 30022. Mr. William N. Lucke was the technical representative for the Federal Railroad Administration. He helped to formulate the research goals and made many helpful suggestions during the work. His help is greatly appreciated.

Assistance was provided by Professor C. P. Siess in planning the structural tests and by Professor E. J. Cording who provided geotechnical input into the planning and evaluation of the tests. Much of the work in preparing the test specimens was done by research assistants and student hourly employees. The research assistants who helped in the testing program were H. Nikooyeh, I-B. Park and R. Prado; hourly student employees were D. Coultas, D. Guse and M. Baxter.

Dual-unit format is employed in the presentation of all data, figures, and tables included in this report. Data and tables are presented in the English system, with International System of Units (SI) values included in parentheses. Large tables are presented with SI values in a separate table. For example, the English values may be presented in Table 3 and the SI values in Table 3-SI. Figures are presented with auxiliary scales for SI units.

TABLE OF CONTENTS

LIST OF TABLES

LIST OF FIGURES

LIST OF SYMBOLS

α	angle that the principal tension stress makes from the liner axis
D	average diameter of the liner
ΔD	diameter change
E	initial tangent modulus of elasticity
f'_c	ultimate compressive strength of the concrete
f_d	tensile stress immediately after cracking, for long beam tests (see Section 4.1.2)
f_p	maximum stress at cracking load (proportional limit), for long beam tests (see Section 4.1.2)
f_r	modulus of rupture from standard beam tests
f_r^*	modulus of rupture from long beam tests (see Section 4.1.2)
f_{sp}	splitting strength of the concrete
K_s	slope of the load-deformation relation for the passive force elements (see Fig. 5.3)
L5, L10, L15...	load increment number for data processing
M	bending moment
N,S,E,W	cardinal points (north, south, east and west)

OD	outside diameter
P	average active load applied to the liner (see Fig. 2.3)
P_{max}	maximum total load resisted by long beams (see Section 4.1.2
P_A, P_B, P_C	average passive loads applied to the liner (see Fig. 2.3)
ϕ	curvature at a section
σ_1	principal compression stress
σ_2	principal tension stress
T	axial thrust in a cross section
θ	angle to locate a cross section in the liner specimen

CHAPTER 1

INTRODUCTION

A system for slipforming a tunnel liner was described by Parker, et al. (1971) that requires the use of fast-setting cement concrete and the possible inclusion of steel fiber in the mix to provide additional tensile strength. The fast-setting cement would allow the liner to resist its own weight plus some ground load as it emerges from the slipform; the liner would continue to gain strength with time as the ground loads increase. The additional tensile strength resulting from the steel fiber may be particularly important during this early period.

A test program is in progress to determine the mechanical properties of steel-fiber-reinforced concrete and to study the mix design parameters and how they affect the mechanical properties (Parker et al., 1973; Paul, et al., 1974; Herring and Kesler, 1974). In addition, monolithic liners cast with fiber-reinforced concrete have been tested in a manner which roughly simulates the interaction of the liner and the surrounding medium.

The liner test program is incomplete. Two tests have been performed and reported previously (Paul, et al., 1974). Four additional tests will be described in this report. Two concrete strengths have been used; a low strength to simulate the rapid-setting concrete strength at an early age shortly after leaving the slipform, and a high strength to simulate the liner after complete hardening. The fiber content was 1.5 percent by volume for all specimens. In the year that follows, 2 additional tests will be performed and the analysis and design recommendations completed.

The test program was planned to develop a better understanding of the structural behavior of cast-in-place liners in the ground. Interaction with the ground strongly influences the structural response, so inclusion of a passive resisting mechanism was considered necessary. Inclusion of the liner in a real soil would be more realistic, but measurement of passive forces would be very uncertain. It would then be difficult to analyze fully the observed structural response. It was decided that a less realistic resisting mechanism that can be adjusted easily, and the forces measured accurately, would be preferable. The structural response and failure conditions in the structure could then be determined. The resisting mechanism that was used is described in Chapter 2 and consisted of hydraulic rams that apply loads distributed over about 8 in. (203 mm) circumferentially. The load-deflection response of these rams can be controlled.

Application of the test results to the more realistic conditions in the ground will be accomplished with a computer analysis. Comparison of the test results with the analysis will confirm the adequacy of the structural analysis model, that can then be used to study continually varying passive pressure and other variables. One analysis based on an existing computer program will be described in Chapter 5.

Design of a liner for given loading conditions requires an estimate of the loads at which cracking and failure occur. Serviceability of a liner depends on the extent of cracking, spalling and deformation, while the safety is a function of the factor of safety against collapse. An adequate analysis must provide a means of predicting cracking as well as ultimate load.

Redistribution of moments within an indeterminate structure that has a ductile section behavior has been studied previously in connection with steel frames and conventionally reinforced concrete buildings, but little of the work has been applied to tunnel supports. In a previous report (Paul, et al., 1974) it was shown that steel-fiber-reinforced concrete liners demonstrate ductile behavior in which the liner shape changes to accommodate the passive resisting mechanism. The load capacity in the test is much larger than that predicted from a linear analysis when failure is assumed to result from material failure in tension. This behavior results from a ductile material and a highly redundant structure that allows the moment-thrust path of the critical sections to follow the moment-thrust failure envelopes and the moments to redistribute in the liner as the thrust continues to increase.

In order to predict the ultimate load on the liner, it is necessary to know where the moment-thrust path of critical sections leave the failure envelope and where the path lies within the region enclosed by it. This would provide a means to predict the complete structural behavior of the liner including the ultimate load, and it is to this end that the test program is generally directed. In the previous tests mentioned above, the liner loading was carried well into the nonlinear range of behavior and the critical sections moment-thrust path followed the failure envelope. However, a hydraulic failure of the loading system occurred during those tests that prevented carrying the test to failure under the desired conditions. The tests described in this report were successfully completed and provide good data for comparison with an analysis that is being developed.

CHAPTER 2

DESCRIPTION OF TESTS

2.1 SPECIMEN FABRICATION

The forms used to cast the specimens consisted of two metal cylinders made of 11 gage smooth sheet metal, 36 in. (915 mm) high, 120 in. (3048 mm) outside diameter and 108 in. (2743 mm) inside diameter. The form is shown in Fig. 2.1. Triangular vertical braces were welded to the forms and bolted to a wood platform after the two cylinders were positioned concentrically. A vertical butt splice facilitated removal of the forms from the specimen. The 6 in. (152 mm) thickness was maintained at

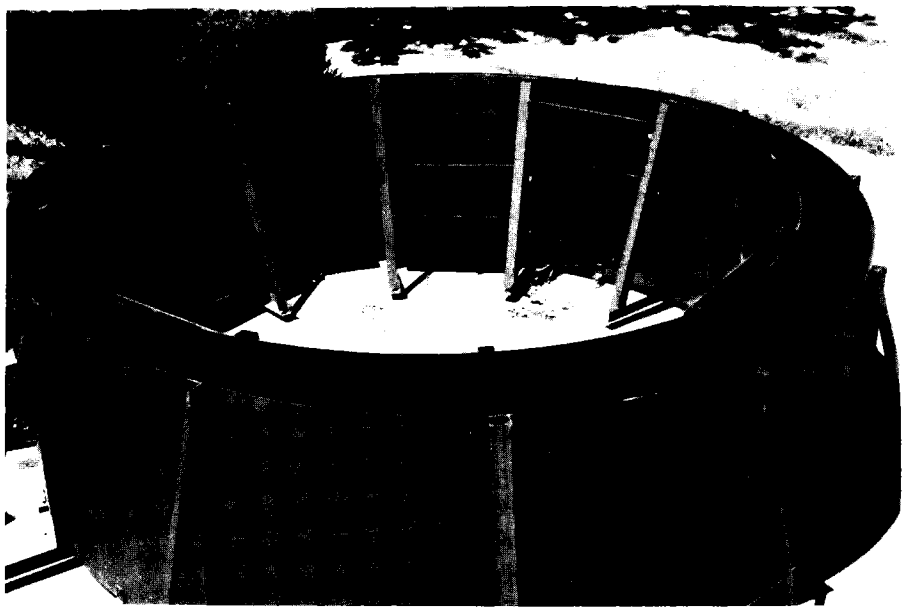

FIGURE 2.1 FORMS USED FOR CASTING THE SPECIMEN

the bottom by closely spaced clip angles bolted to the platform and at the top by metal separators between the cylinders.

As part of the general instrumentation, pairs of pipes 3/8 in. (9.5 mm) OD and 6 in. (152 mm) long were placed at midheight between the two forms. These pairs of pipes were 12 in. (305 mm) apart horizontally and centered at sections 90 deg apart on the specimens; the resulting holes through the specimen were used to support devices for measuring the relative rotation between these sections. These pipes also helped to control the specimen thickness.

Two different mix proportions were used to obtain two different concrete strengths. The concrete was purchased from a local ready-mix plant and transported to the laboratory in a transit mix truck. The truck arrived with the proper amount of aggregate that contained some natural water. The remaining ingredients were added at the laboratory. Water was added first, calculated to provide an adequate slump, after which steel fiber was sprinkled into the transit mix hopper. After a short time of mixing, the cementitious materials were added. Fly ash was substituted for part of the cement in the mix for the 2 specimens that were to have low strength (designated C3 and C6). This material provides reduced strength and maintains the proportion of cementitious solids. For the other two specimens of high strength (designated C4 and C5) standard ingredients were used.

The specimens were cast in two lifts of 18 in. (450 mm). Each lift was vibrated at its mid-height with two form vibrators attached to the walls of the inside form and opposite one another. When the vibrators were

raised for the second lift, they were rotated 90 deg from the previous position. Both lifts were vibrated for approximately 20 seconds.

The forms were removed after one day and the specimens were cured under moist conditions by covering them with wet burlap and vinyl sheeting for a period of 20 days, after which the cover was removed. Further curing took place in the laboratory air which is maintained at approximately 50 percent relative humidity.

2.2 MATERIAL PROPERTIES

For the liners and control specimens 2.4 cu yd (1.8 m^3) of concrete was mixed with Type 1 cement and 1.5 percent steel fiber by volume or approximately 200 lb/cu yd (118.6 kg/m^3). The basic mix and properties of the fresh concrete are shown in Table 2.1. A summary of the properties of the hardened concrete is shown in Table 2.2. The fly ash not only reduced the strength of the concrete, but also rendered a modulus of elasticity comparable to fast-setting cement concrete at an early age. The steel fiber used was U. S. Steel Fibercon, which is 1 in. (25 mm) long and 0.022 x 0.010 in. (0.56 x 0.25 mm) in cross section.

The mechanical properties in Table 2.2 were obtained by testing control specimens at various times before and after the liner test and picking from the graphed results the values at the time of test. Each test point for compressive strength was the average of 3 or more individual tests. The modulus of rupture is the average of 3 or more tests of 6 x 6 x 21 in. (152 x 152 x 533 mm) flexure specimens and the split tensile strength

TABLE 2.1

MIX PROPORTIONS FOR LINER SPECIMENS*

	Spec C3	Spec C4	Spec C5	Spec C6
Sand, lb (kg)	2080 (945)	1462 (663)	1470 (666)	1994 (904)
Pea gravel, lb (kg)	549 (250	1045 (474)	1063 (481)	622 (282)
Fly ash, lb (kg)	358 (163)			308 (139.5)
Cement, type 1, lb (kg)	179 (81.5)	793 (359)	805 (364)	282 (127.7)
Free water, lb (kg)	441 (200)	439 (199)	439 (199)	427 (193.5)
Fibers, lb (kg)	200 (90.8)	197 (89.2)	200 (90.8)	197 (89.2)
Unit weight, lb/cu ft (kg/cm^3)	141 (2258)	146 (2335)	147 (2350)	142 (2270)
Slump, in. (mm)	5 (127)	6 (152)	5.25 (133)	8.25 (210)
Air entrained, percent	2.8	0.2	0.7	0.1

*Quantities for 1 cu yd batch (0.76 m^3), for saturated surface-dry aggregates.

TABLE 2.2

PROPERTIES OF HARDENED CONCRETE

Specimen	Compressive strength, f'_c, psi (kPA)	Modulus of rupture, f_r, psi (kPA)	Splitting tensile strength, f_{sp}, psi (kPA)	Initial modulus of elasticity, E, ksi (MPa)	Modulus of elasticity from ACI formula, ksi (MPa)
C3	2200 (15150)	500 (3450)	265 (1800)	1520 (10500)	2580 (17760)
C6	2400 (16600)	610 (4170)	340 (2320)	1720 (11700)	2730 (18800)
C4	6660 (45500)	855 (5850)	765 (5230)	3000 (20500)	4760 (32800)
C5	7630 (52200)	850 (5820)	795 (5840)	3100 (21200)	5150 (35500)

is the average of 6 tests of 6 x 6 in. (152 x 152 mm) split cylinder specimens. The initial modulus of elasticity was obtained from the average of 3 or more tests on standard cylinders in a 600 kip (2,670 kN) hydraulic testing machine with a constant head movement of 0.03 in./min (0.76 mm/min). The load and strain were recorded on a X-Y recorder.

2.3 INSTRUMENTATION

The instrumentation had two objectives. The first was to determine the overall behavior of the liner in terms of loads and deformations. The second was to make measurements that would allow the calculation of internal forces. The liner, as loaded, is indeterminate to the third degree providing that all the external forces are measured. It is necessary to determine three internal quantities in order to calculate internal forces at any point. In the tests performed previously strain gages were placed at the quarter points so that the moments and thrusts could be computed at these locations. To do this a knowledge of the modulus of elasticity of the concrete was required.

In the tests described in this report a series of strain gages was placed circumferentially about 2-1/4 in. (56 mm) apart near the four quarter points of the liner on the inside and out. These gages allowed the location of the section that had the same strain on the inside and out, and therefore were sections with moment equal to zero. With three of these sections (inflection points) located, the internal forces could be computed from equilibrium. The actual mid-height location of the gages for specimens C3 and C4 is shown in Fig. 2.2(a). After the testing of C4 a better knowledge of the location of the inflection points was obtained

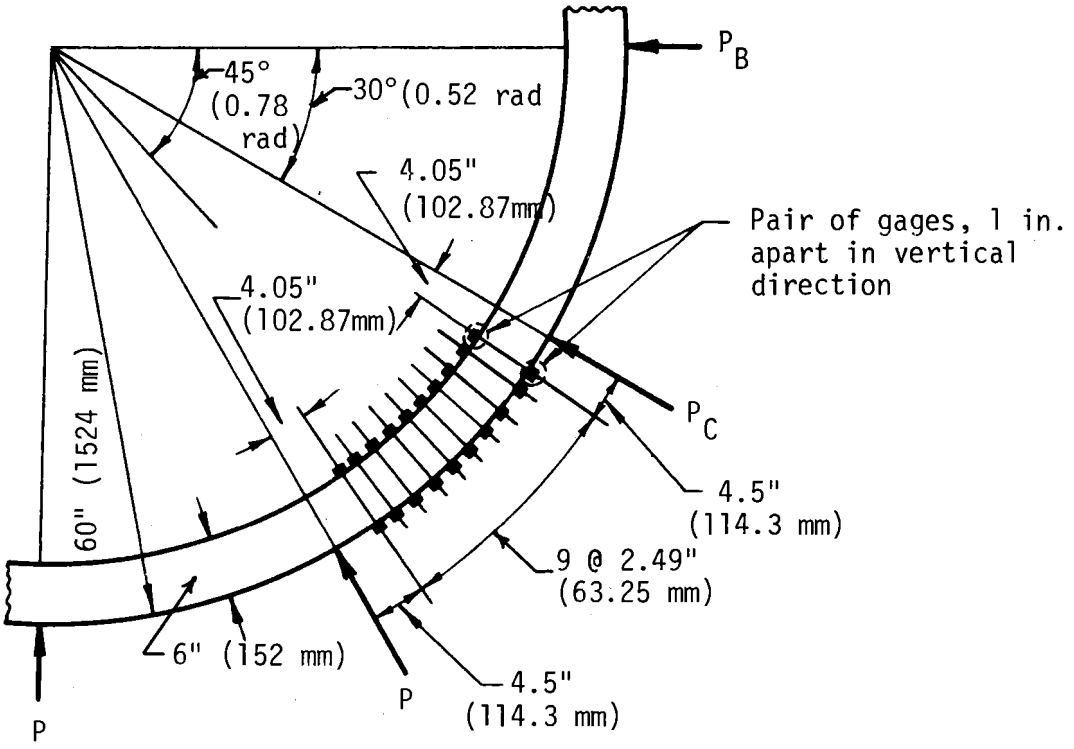

a) Specimens C3 and C4

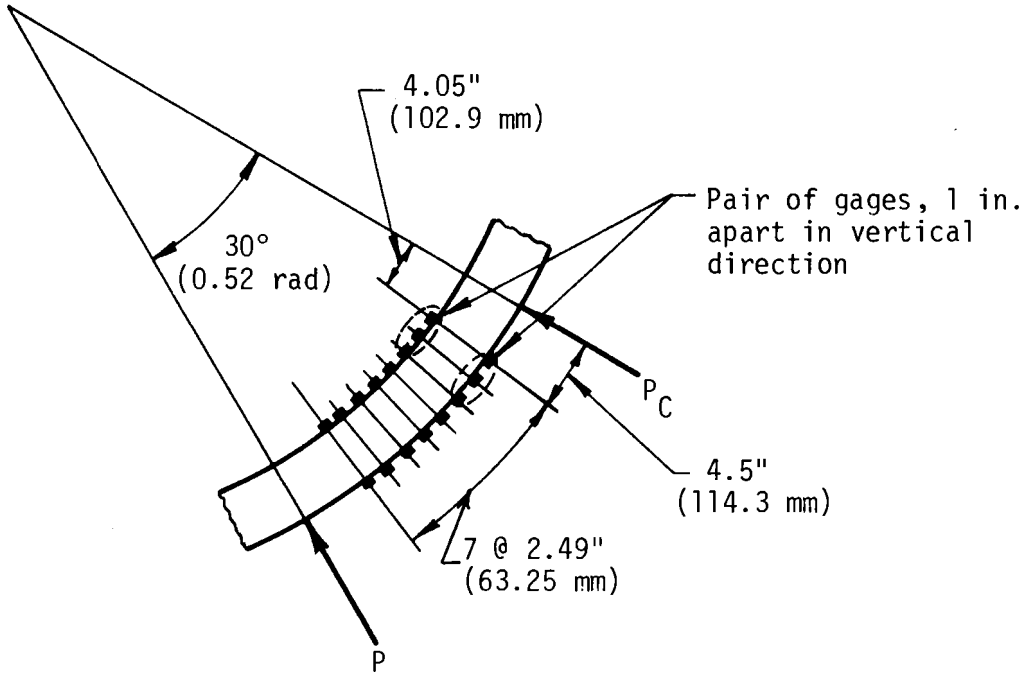

b) Specimens C5 and C6

FIGURE 2.2 STRAIN GAGE LOCATIONS FOR DETERMINING INFLECTION POINTS

and the gage locations were altered as shown in Fig. 2.2(b). A few gages were also located near the top and bottom of the liner specimen to study the vertical distribution of loading.

The overall structural response was monitored by measuring the diameter change at all six loaded diameters. Linear variable differential transformers (LVDT's) connected to tensioned wires across the diameters were used for these measurements and checked with dial gage measurements. The LVDT's located on the passive load diameters were also used to control the passive load-deflection behavior as discussed in Section 2.4.

The loads applied by each of the 24 rams were measured with load cells placed between the ram and the load spread beams. The loads were recorded at each increment. Sensitivity of the load measurements is indicated by the calibration factors for the load cells which averaged 68 micro-inches of strain per kip of load (388 micromm/kN).

All measurements were taken at each load increment. The output of the LVDT's, strain gages and load cells were connected to automatic switching and balancing equipment. The sequence of reading consisted of first the load cells, then the strain gages and LVDT's and finally the load cells again. This process took about ten minutes and the second set of load cell readings allowed the calculation of loss of load due to creep of the specimen. Unless otherwise specified all the loads reported herein will correspond to the first set of load readings. The changes in voltage read by the balancing and reading equipment were automatically recorded by a teletype which produced a punched paper tape and typed copy. The data was then transmitted to a computer where it was converted to more usable

information and transmitted back to the test site immediately. In this way the information obtained for one loading increment was used to plan the next.

2.4 TEST PROCEDURE

The procedure used for loading the specimens and controlling the passive forces was the same as described by Paul, et al. (1974) in previous tests. The liner section was oriented so the longitudinal direction in the tunnel is vertical in the test. The location of active and passive forces relative to north and the number of load points is shown in Fig. 2.3; a photograph of the load arrangement is shown in Fig. 2.4.

The specimens were 3 ft (914 mm) high, and loads were applied at 30-deg increments as shown in Fig. 2.3. There were two 60-ton rams at each load point, located 6 in. (152 mm) and 30 in. (762 mm) above the bottom of the specimen, that applied load to the test specimen through a ball joint and a W8x48 (203 x 1219 mm) spread beam. The load was spread over a width of 8 in. (203 mm). The ram reactions were resisted by concrete abutments bolted to the test floor as shown in Fig. 2.4. Cylindrical bearings were placed between the ram and abutment to prevent transfer of a shearing force to the specimen at all load points except those at the north, south, east and west. These sections were constrained to move in only the radial direction so the base of the rams were flat. The spread beam was grouted to the specimen to assure uniform bearing.

The weight of the specimen rested on nests of rollers between steel plates located 90 deg apart at the cardinal directions and oriented

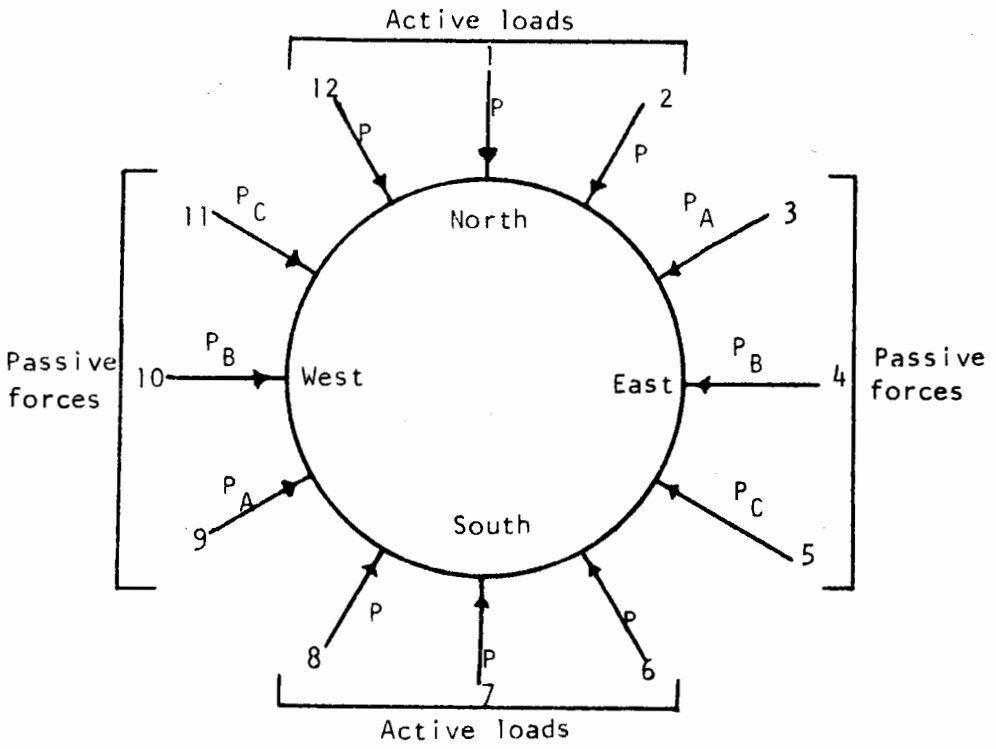

FIGURE 2.3 LOADING OF THE LINER SPECIMEN

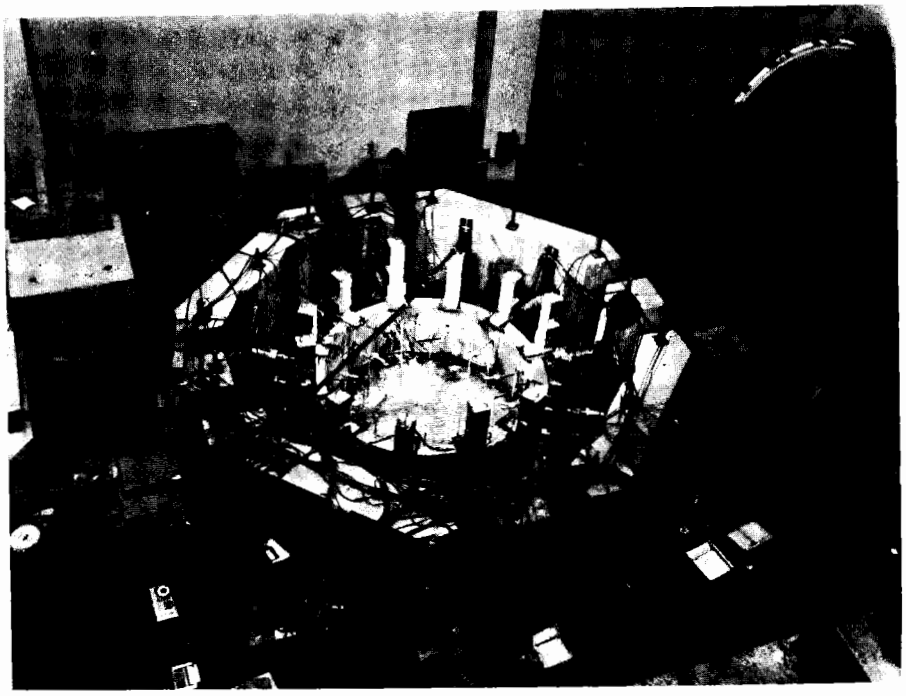

FIGURE 2.4 OVERALL VIEW OF TEST ARRANGEMENT

to roll in the radial direction. During previous tests the loading arrangement had a tendency to become unstable because of translational movement of the specimen. The loads were applied so that they were self equilibrating, but friction in the hydraulic rams caused slightly nonsymmetrical forces and the resulting movement accentuated the problem. Thus, brackets of the type shown in Fig. 2.5 were placed at the north, south, east and west sections to prevent the translation. Lateral rollers in the brackets reduced the frictional resistance to radial movement. The forces on the brackets, although small in magnitude, influence the internal forces in the liner as will be explained later.

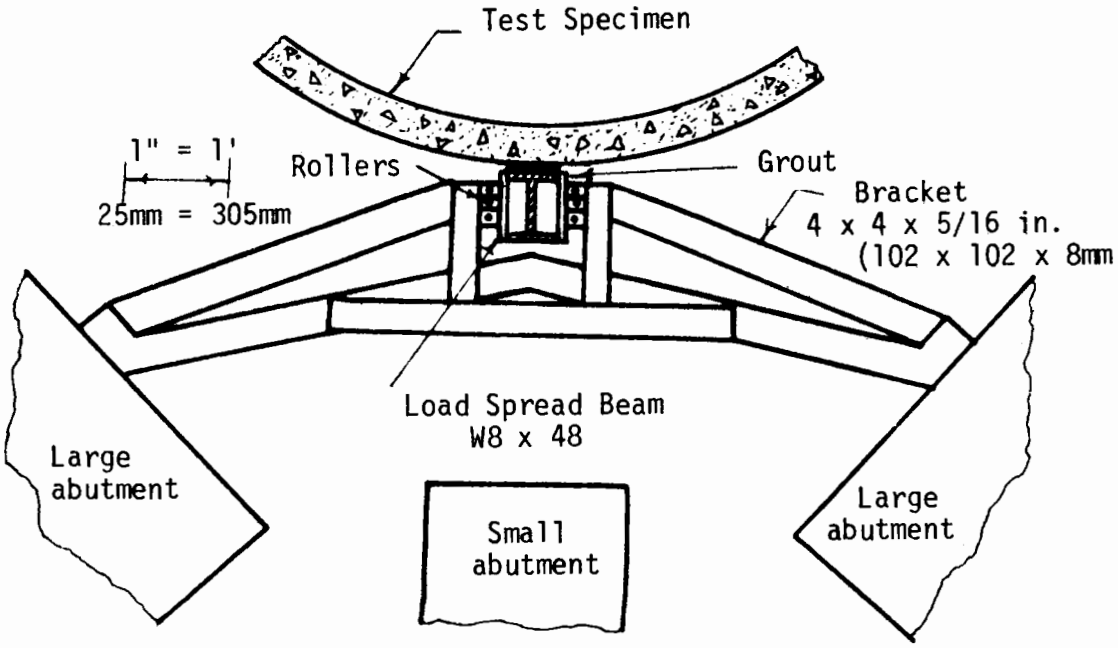

FIGURE 2.5 BRACKETS LOCATED AT THE NORTH, SOUTH, EAST AND WEST SECTIONS TO PREVENT RIGID-BODY MOTION OF THE SPECIMEN

The 4 passive force rams located at each end of each loaded diameter were connected hydraulically. Therefore, they should have the same load, but the friction in the rams vary so there is some small variation in the load. The passive loads P_A, P_B and P_C that will be discussed in later sections are the total passive load at a load point (one end of the diameter) obtained as 2 times the average of the 4 ram loads on the corresponding diameter. All 12 of the active rams were connected hydraulically so the loads varied only slightly due to differences in the ram friction. The active load "P" that will be discussed is the load in two of the rams at one active load point obtained as 2 times the average of 12 active rams.

All passive forces in all tests were adjusted so that they would have a linear load-deflection relationship. This relationship was controlled separately for P_A, P_B, P_C (Fig. 2.3), as mentioned before. The load-deflection control was accomplished by connecting the load point displacement to the X axis, and the ram load to the Y axis of an X-Y recorder, so that the load and displacement could be continuously monitored. The load-deflection relationship desired was drawn on the graph paper of the recorder and the loads were adjusted by manipulating the ram pressure with a manual pump so that the pen of the recorder followed the predetermined line.

Load increments were applied by increasing pressure in the active rams while the passive loads were adjusted. When the active loads reached a predetermined value, some time was taken to allow the hydraulic system to attain equilibrium, after which all hydraulic valves were closed and the instrumentation readings taken. This process, from the beginning of load application to the end of the readings required from 20 to 25 minutes.

At high load levels, the creep of the specimen allowed some loss of load during the period when the readings were taken.

CHAPTER 3

TEST RESULTS

Four monolithic steel-fiber-reinforced liners were tested to failure. Two specimens designated C3 and C6 had low strength and physical properties similar to that of rapid-setting cement concrete at a relatively early age. The other two, designated C4 and C5, had strength and physical properties typical of fully cured concrete. Properties of the materials in each specimen are summarized in Table 2.2.

All four tests were performed in the manner described in Section 2.3, with active loads on the north and south, and passive forces on the east and west as shown in Fig. 2.3. The passive forces were adjusted so that they had a linear load-displacement relationship that was 100 kips/in. (17.5 kN/mm) for the high strength specimens and 250 kips/in. (43.7 kN/mm) for the low strength ones. The active load P used in the discussion that follows is the load that occurs at one active load point or the load in the two rams at the location and is calculated as twice the average of all 12 active ram loads. The passive loads P_A, P_B and P_C are calculated as twice the average of the 4 ram loadings in the corresponding locations shown in Fig. 2.3.

The tests are summarized in Table 3.1. In the following sections the results will be presented by discussions of first the overall behavior, then the deformation of the specimens as they are related to loads, and finally, the internal forces. In these presentations, the load increments are labeled on some of the graphs. The purpose is to correlate various

TABLE 3.1

SUMMARY OF LINER TEST RESULTS

Specimen	Compressive strength, f'_c, psi (kPa)	Stiffness of the passive forces, kips (kN/mm)	Maximum average active load, P, kips (kN)	Diameter change at failure ΔD/D	
				N-S direction	E-W direction
C3	2200 (15150)	250 (43.7)	129 (576)	0.0202	0.0106
C6	2400 (16600)	250 (43.7)	140 (625)	0.0213	0.0115
C4	6660 (45500)	100 (17.5)	115 (514)	0.0367	0.0273
C5	7630 (62200)	100 (17.5)	137 (609)	0.0526	0.0370

events among the graphs and observations. The load increment designated with an L in some figures are those assigned to the files for computer processing of the data. The first load is usually designated L3 or L4, and occasionally there is a number missing.

3.1 OBSERVATIONS OF BEHAVIOR

3.1.1 TEST C3

Failure occurred at an average active load P of 129 kips (575 kN) after considerable cracking had occurred, and after the last readings were taken at increment 23 with an average active load of 127.4 kips (565 kN). The location of tension cracking and crushing of the concrete is shown in Fig. 3.1. The extent of cracking during loading is shown in the photographs of Figs. 3.2 and 3.3. Heavy cracking occurred on the inside at the north and south, 20 deg south of east and 45 deg south of west. An example of this inside cracking is shown in Fig. 3.3(a). On the outside crushing occurred on each side of the north and south load spread beams. There was also minor cracking on the outside 45 deg south of west and minor crushing at other locations as shown in Fig. 3.1. Collapse occurred when the region failed just east of the south load spread beam as shown in Fig. 3.3(b). This failure occurred progressively, so that the initial crushing just prior to failure and movement along the failure surface was observed, but final failure and large movement beyond this initial stage was sudden. The peak load at failure was reached after the readings were taken at increment 23 and after an additional 2 kips (8.9 kN) were applied. The bar shown in the

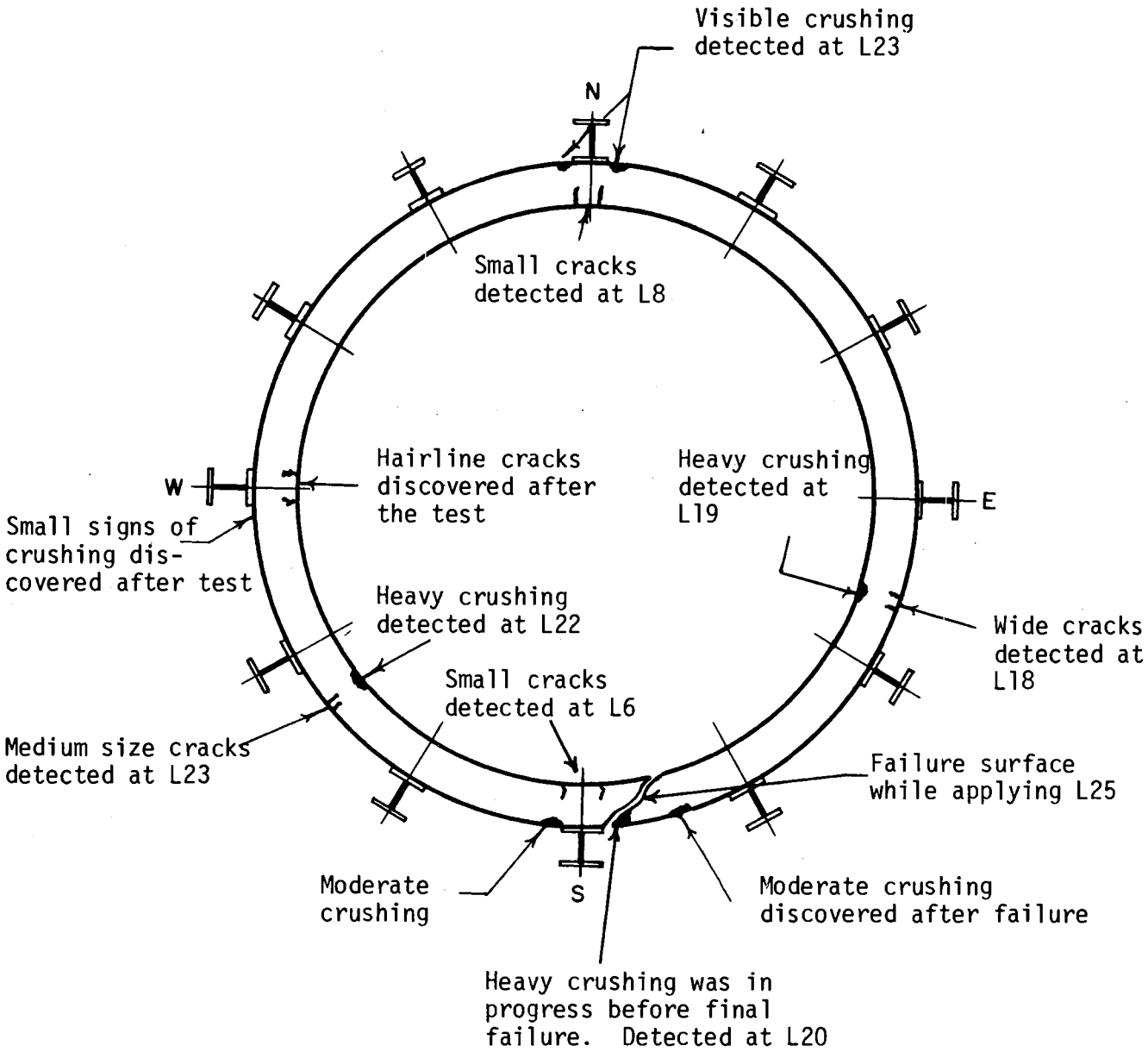

FIGURE 3.1 SPECIMEN C3 DAMAGE DURING TESTING

(a) South portion

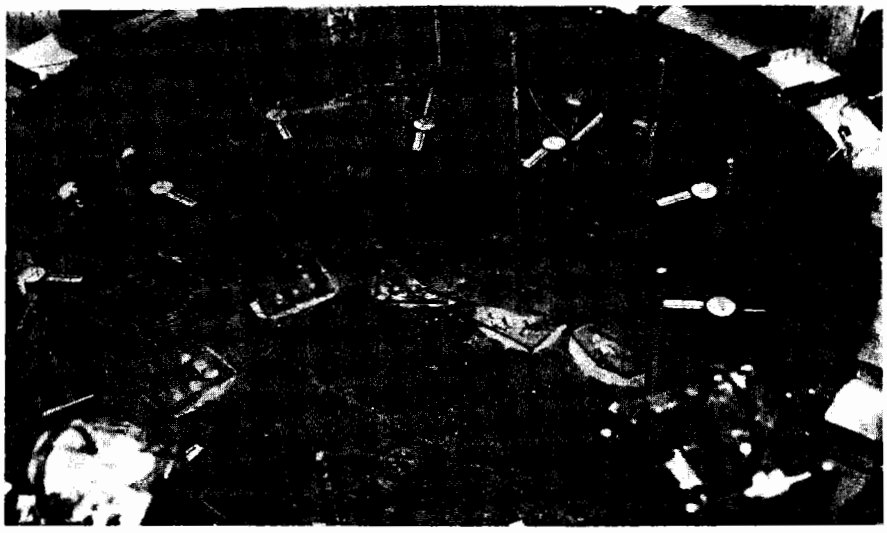

(b) North portion

FIGURE 3.2 SPECIMEN C3 AFTER TESTING

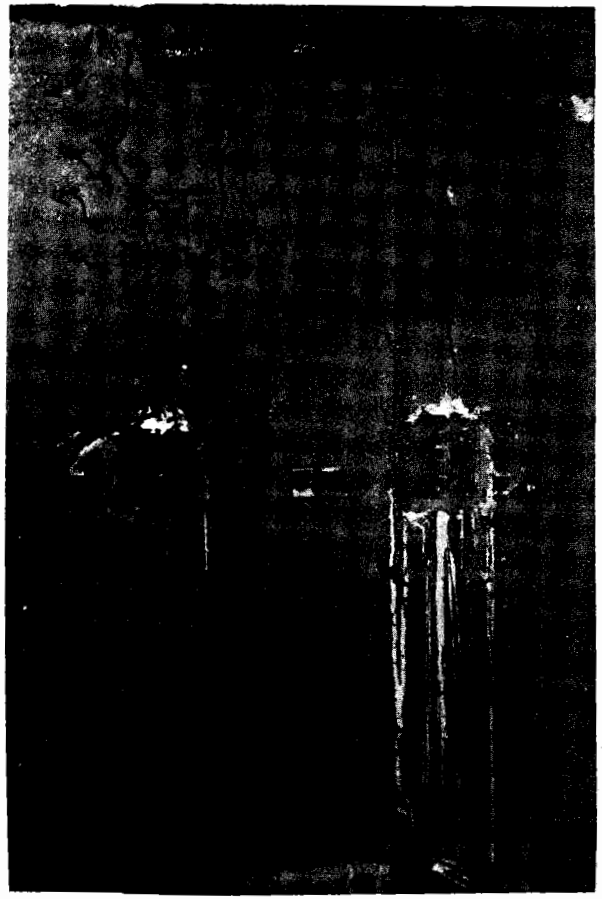

(a) Inside south

(b) Top

FIGURE 3.3 FAILURE REGION FOR SPECIMEN C3

photograph is a pick-up eye used to handle the specimen, and was embedded about 18 in. (457 mm) in the specimen.

3.1.2 TEST C6

Failure occurred while taking the readings at increment 20. The complete set of readings were not taken, but the maximum average active load was recorded to be 140 kips (625 kN).

As before, extensive and progressive cracking and crushing occurred during the test. The extent and sequence of damage is shown in Fig. 3.4 and the photographs in Fig. 3.5. Thin tensile cracks were detected inside at the south and north locations at loads of 19.5 and 24.5 kips (86.8 and 109.6 kN) respectively. The cracks at north never widened appreciably and moderate crushing appeared just east of the north load spread beam at a load P of 117.1 kips (521 kN). At a load of 53.6 kips (240 kN) one of the inside cracks at the south became clearly visible and extended the height of the specimen. This crack constituted the major tensile crack and opened to about one fourth of an inch. Opposite the latter tensile crack, heavy crushing occurred just east of the south load spread beam, and moderate crushing just west of the south load spread beam was detected initially at loads of 117.1 and 124.4 kips (421 and 554 kN) respectively.

Tensile cracks also appeared on the outside, south of the east load spread beam at a load of 73.4 kips (328 kN). There were several cracks and though they were visible to the eye did not widen appreciably. Opposite these cracks moderate crushing occurred, first detected at a load of 124.4 kips (556 kN).

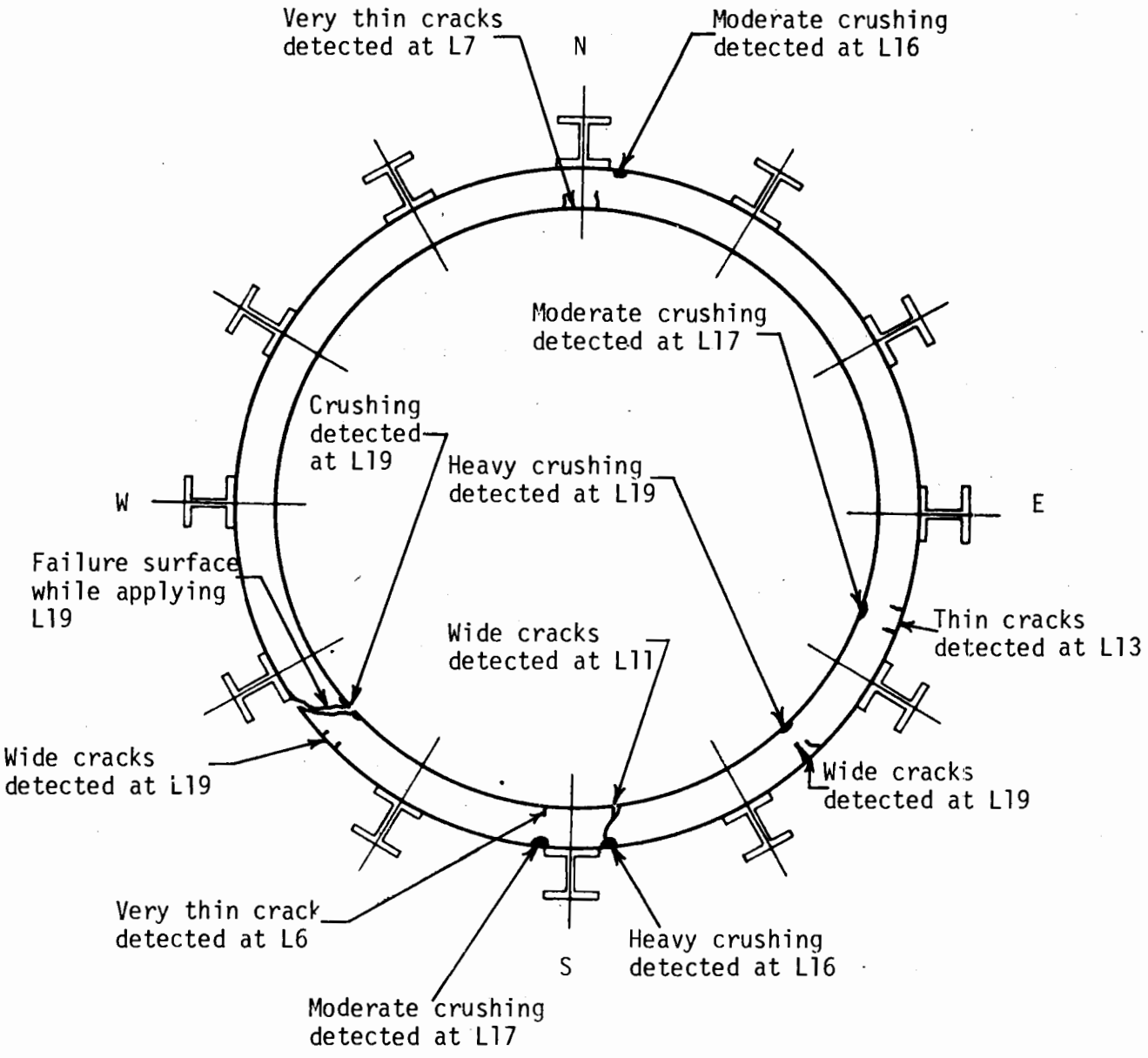

FIGURE 3.4 SPECIMEN C6 DAMAGE DURING TESTING

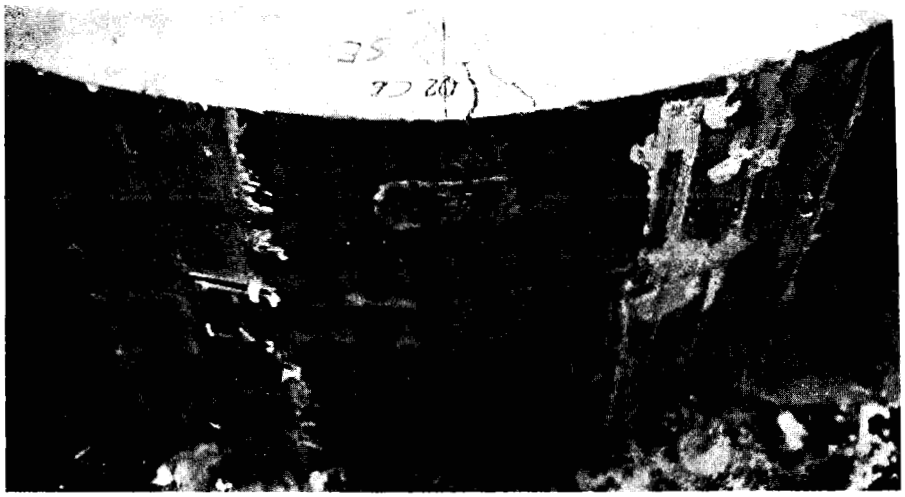

(a) Southeast outside

(b) South outside

FIGURE 3.5 SPECIMEN C6 AFTER TESTING

Final failure occurred near the middle of the southwest quadrant; clearly visible tensile cracks appeared at the outside of the specimen rather suddenly at a load of 132.4 kips (592 kN). At the same load, corresponding to load increment 19, crushing was detected on the inside opposite these cracks. Final failure occurred during the application of the next load increment in a way similar to that described for C3, along a diagonal surface through the thickness, ending at the inside where the initial crushing was detected. Photographs of the failed section are shown in Fig. 3.6.

At the end of load increment 19, corresponding to a load of 132.4 kips (592 kN), tensile cracks on the outside and crushing on the inside appeared suddenly in the middle of the southeast quadrant. During the application of the last load increment these cracks opened rapidly and the crushing increased, but final failure occurred at the location described before and not at this section.

3.1.3 TEST C4

Failure occurred while applying increment 25 at a negligible increase in active load over increment 24. The maximum average active load recorded was 115 kips (514 kN) at both of the last two increments (23 and 24).

Extensive and progressive cracking, crushing and spalling occurred during the test. The extent and sequence of damage is shown in Fig. 3.7 and in the photographs in Fig. 3.8. Extensive tensile cracking occurred on the inside at the north and south positions at early stages of loading that widened

(a) Outside

(b) Top

FIGURE 3.6 FAILURE SECTION OF SPECIMEN C6

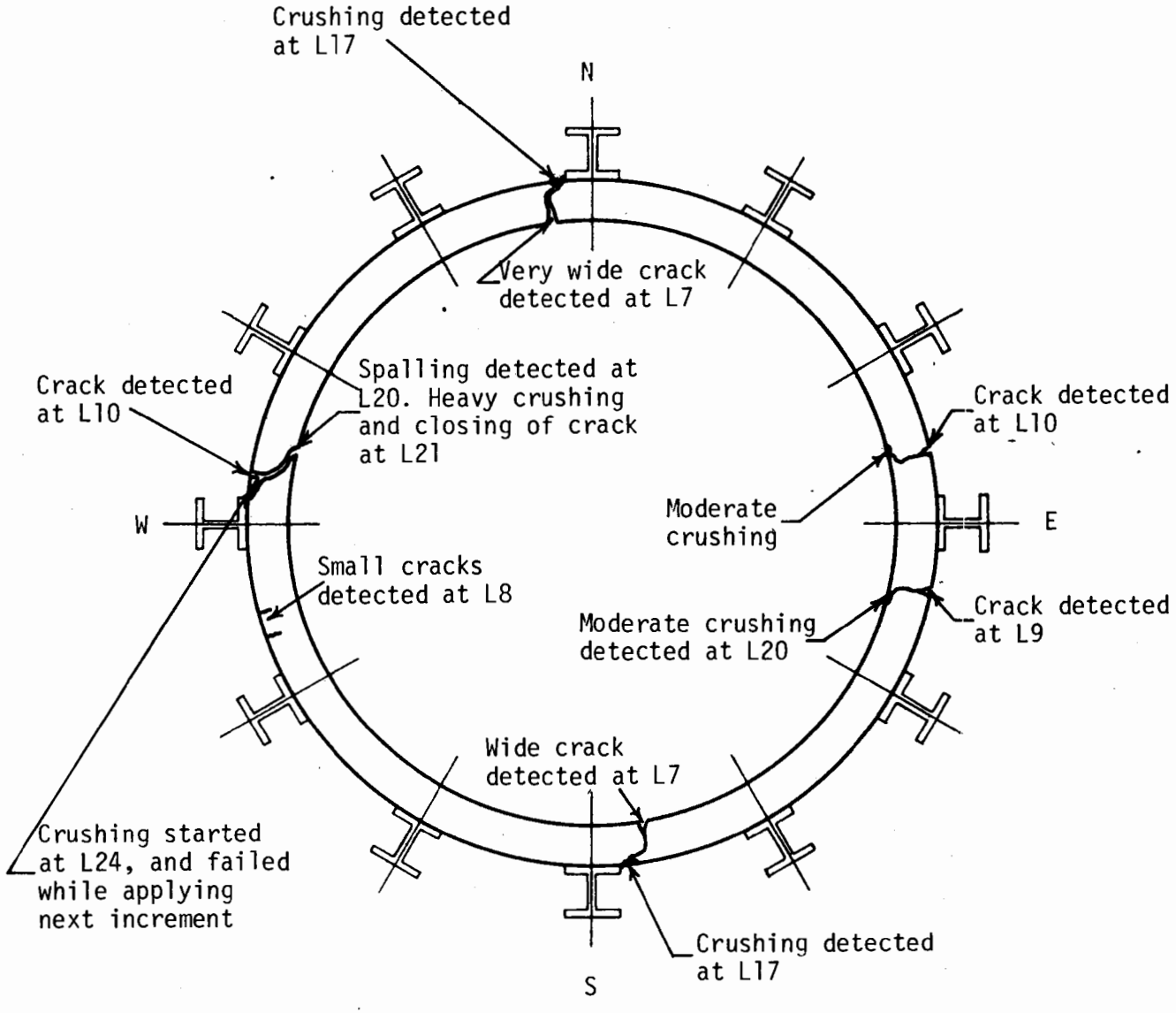

FIGURE 3.7 SPECIMEN C4 DAMAGE DURING TESTING

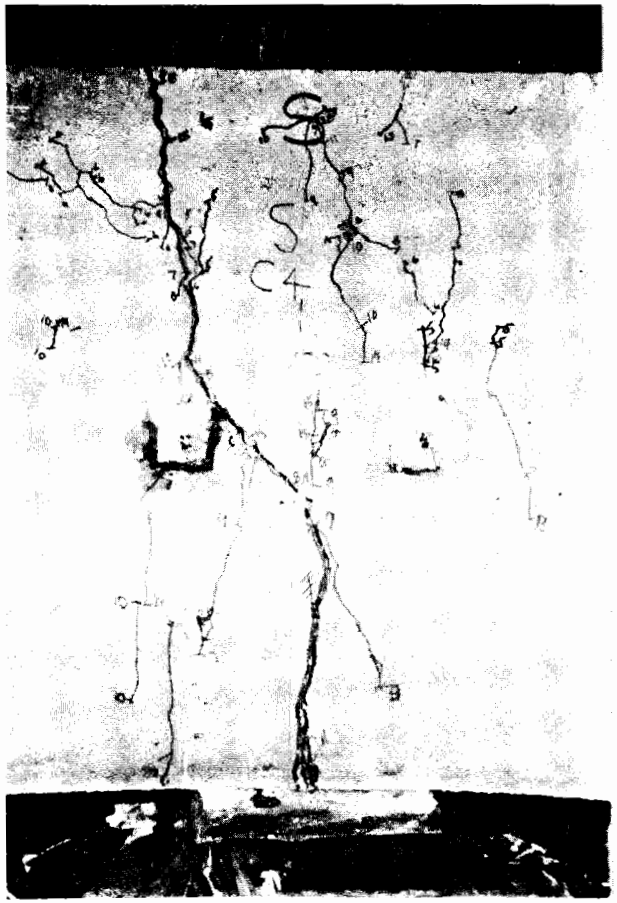

(a) South inside

(b) North inside

FIGURE 3.8 SPECIMEN C4 AFTER TESTING

progressively up to one-fourth of an inch. Late in the test, crushing appeared in the compression zone opposite these cracks. Tensile cracks also appeared outside, at both sides of the east load spread beam at a higher load after the occurrence of the main cracks already described. These cracks also widened progressively, but not as much as those at the north and south, positions as crushing occurred opposite them late in the test.

Final failure occurred just north of the west load spread beam. First, a flexural crack appeared on the outside at a load P of 23.5 kips (105 kN), the cracks opened progressively and spalling occurred on the inside opposite the crack, at a load P of 94 kips (419 kN). At a load of 103.8 kips (461 kN) sudden crushing of the spalled zone on the inside was clearly observed, and the tensile crack closed. As a result of this, the surfaces of the original cracks came in contact and bearing developed. At increment 24, corresponding to an average active load of 115.1 kips (513 kN), the thrust across the crack caused crushing on the outside of the liner and the section failed during the application of the next increment of loading by spalling a wedge of concrete on the outside. Photographs of the failure section are shown in Fig. 3.9.

3.1.4 TEST C5

Failure occurred just as increment 29 began. The average active load P never increased beyond a value of 134.9 kips (600 kN) recorded at increment 28. However, the maximum P had already occurred and was 136.6 kips (609 kN) recorded at increment 27.

Tensile cracking started early in the test, followed by sizable

(a) Outside

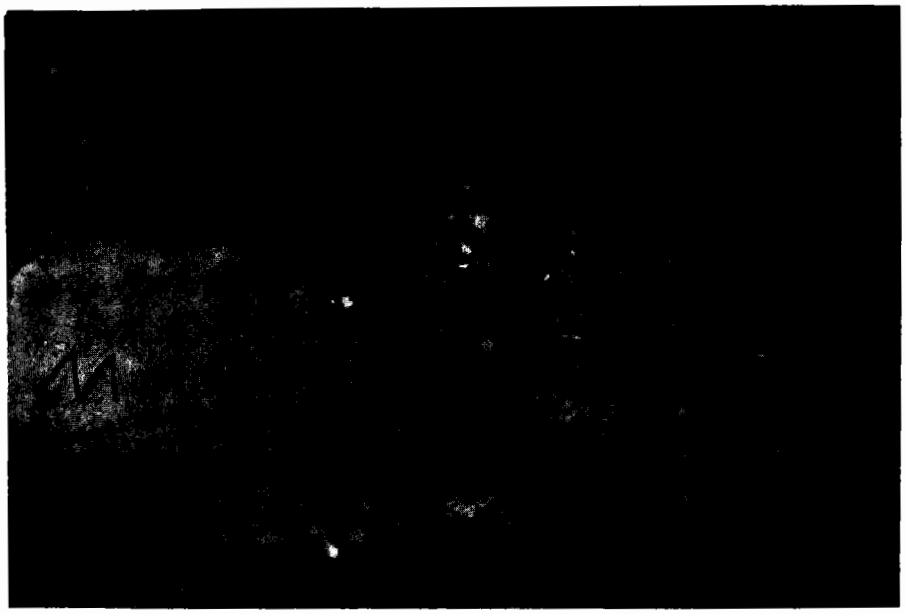

(b) Top

FIGURE 3.9 FAILURE SECTION OF SPECIMEN C4

widening of the cracks, and spalling and crushing toward the end of the test. The extent and sequence of damage is shown in Fig. 3.10 and photographs in Fig. 3.11.

Tensile cracks were detected at the inside north and south, at a load of 9.4 kips (42 kN). These cracks progressively widened and penetrated deeply, reaching a width of more than a quarter of an inch. After the test was completed and the load spread beams removed, crushing was discovered hidden by the beams and opposite the tensile cracks at the north and south positions.

At loads of 21.6 and 27.7 kips (96.5 and 123.8 kN), tensile cracks appeared on the outside near the south and then at the north of the east load spread beam. The crack to the south of the east position never widened appreciably. The crack to the north of the east position opened progressively, while crushing appeared opposite it at a load of 78.3 kips (349 kN). This crushing also increased progressively, and at a load of 110.2 kips (493 kN) a sudden and large amount of crushing occurred and the tensile crack closed. However, final failure did not occur at this section.

Final failure occurred at a section north of the west load spread beam. A tensile crack was detected on the outside at a load of 27.7 kips (123 kN). One of these cracks opened progressively, while crushing appeared opposite it at a load of 78.3 kips (349 kN). This crushing also progressed and after a load of 84.2 kips (660 kN) closing of the tensile crack was observed. As a result of this, the surfaces of the crack came in contact, and bearing developed across it. During the beginning of increment 29 the section finally failed by spalling of a wedge of concrete on

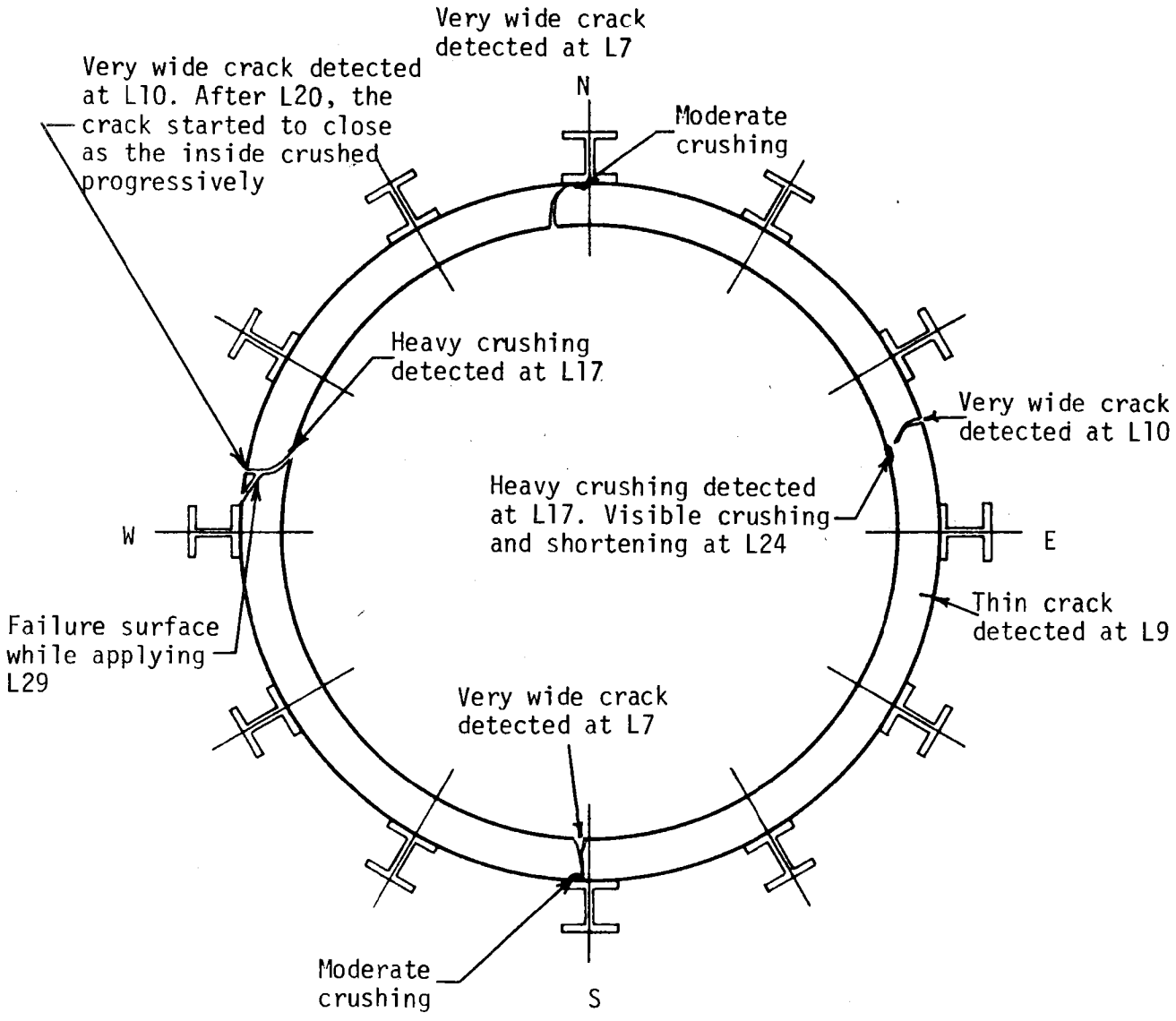

FIGURE 3.10 SPECIMEN C5 DAMAGE DURING TESTING

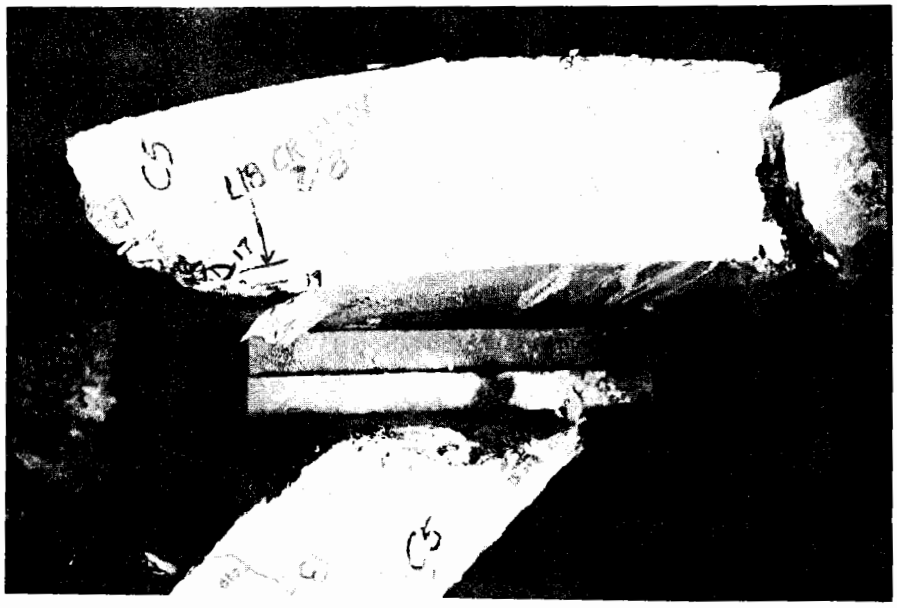

(a) Top

(b) Outside

FIGURE 3.12 FAILURE SECTION OF SPECIMEN C5

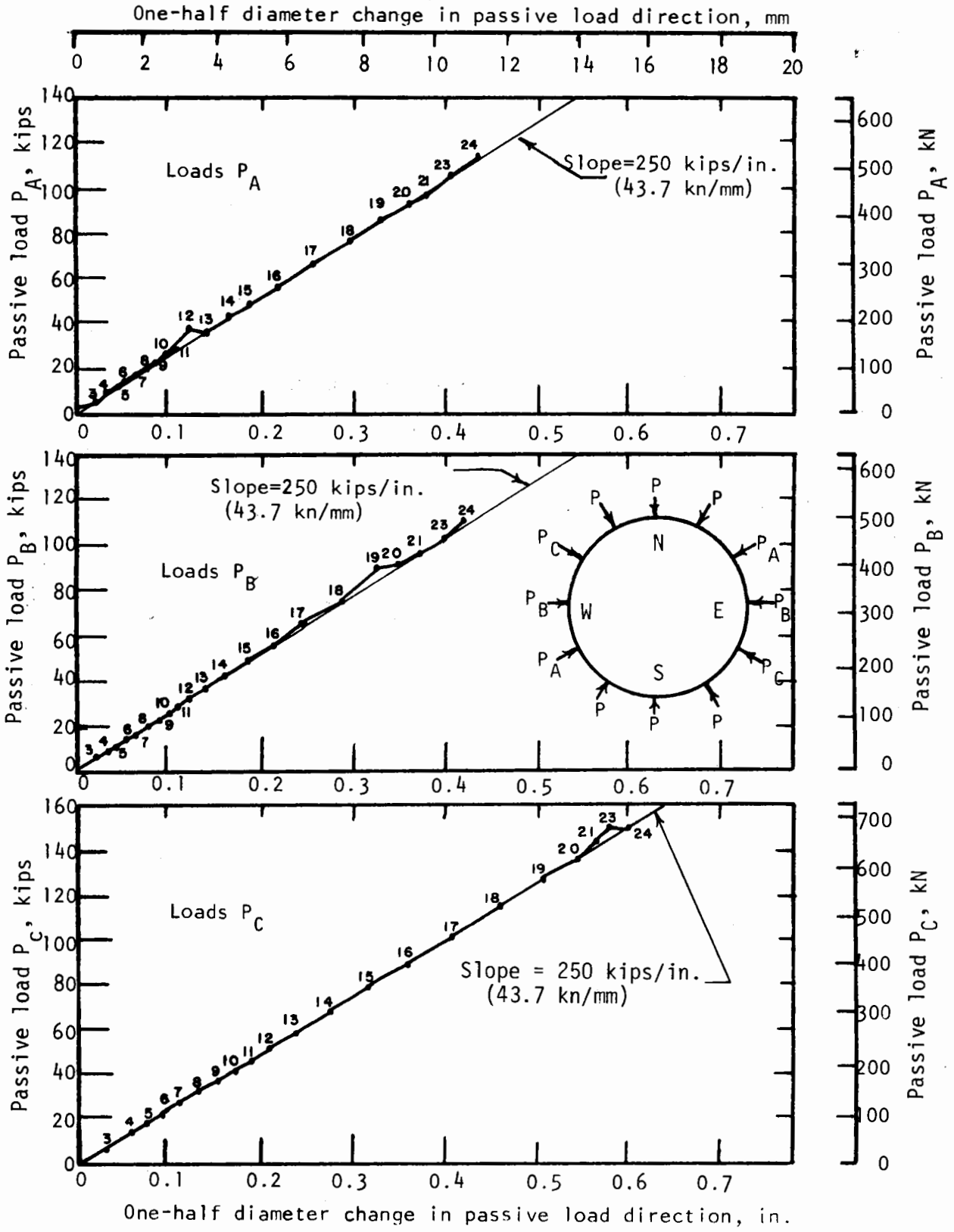

FIGURE 3.13 LOAD-DEFORMATION FOR PASSIVE FORCES IN TEST C3

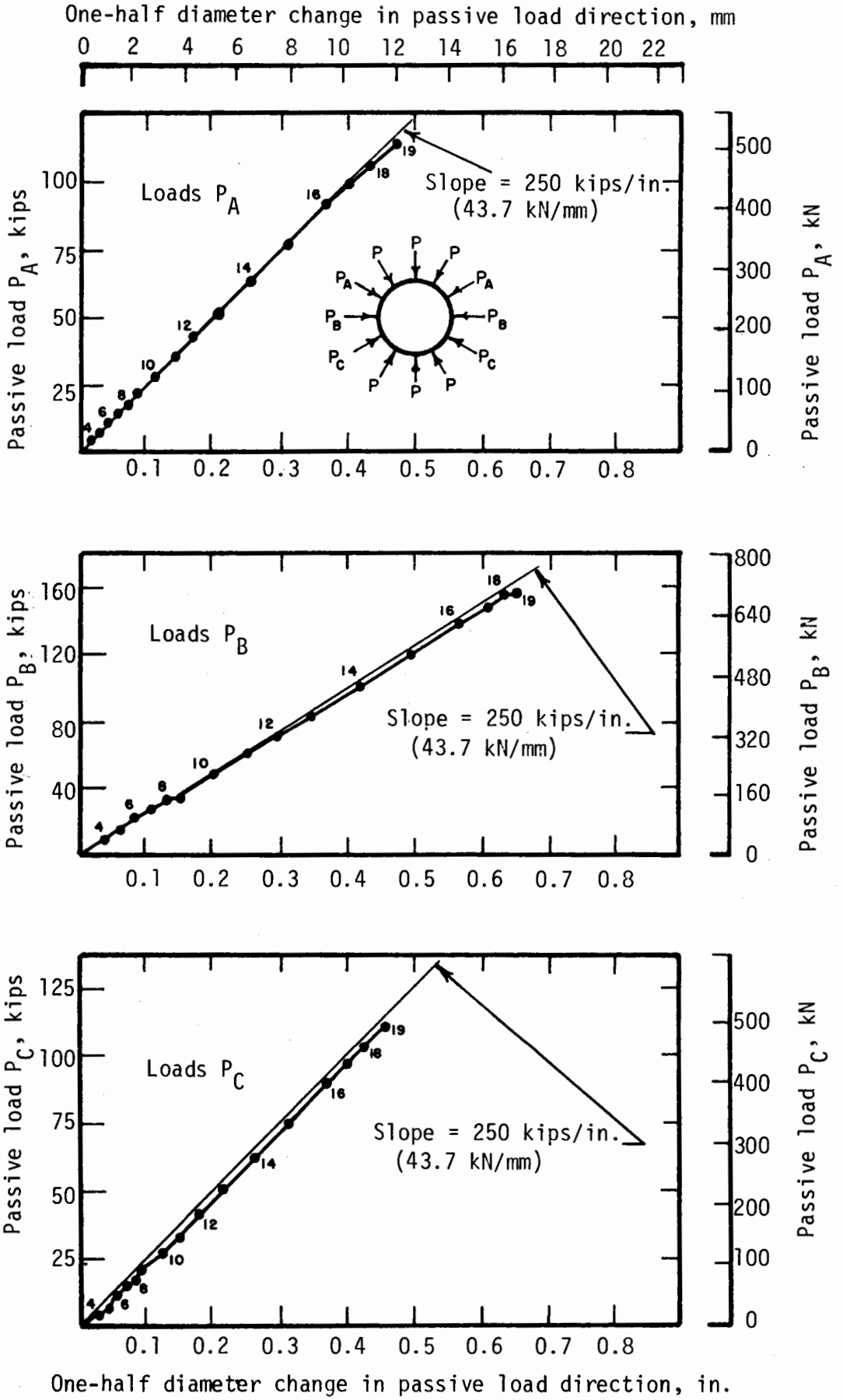

FIGURE 3.14 LOAD-DEFORMATION FOR THE PASSIVE FORCES IN TEST C6

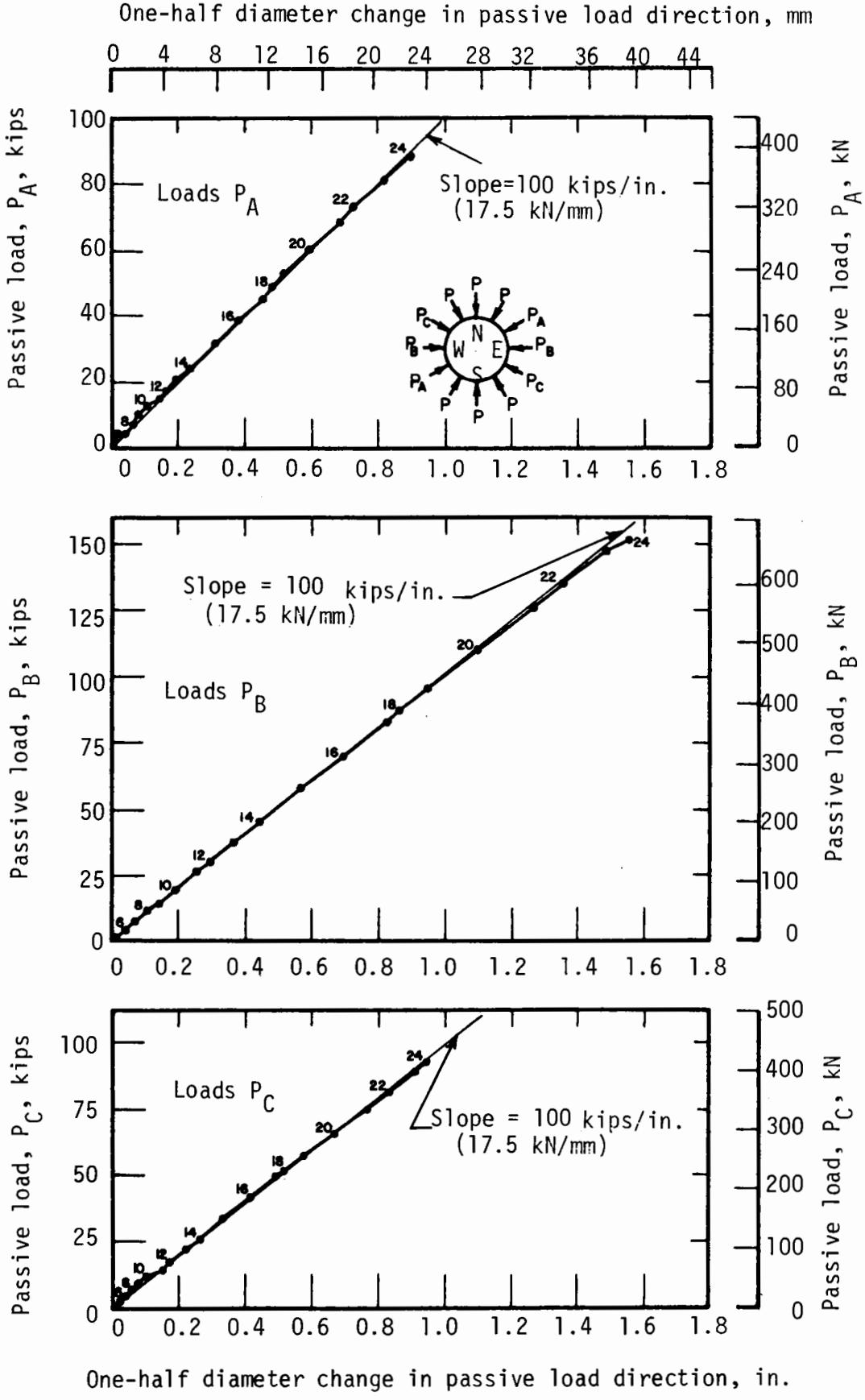

FIGURE 3.15 LOAD-DEFORMATION FOR PASSIVE FORCES IN TEST C4

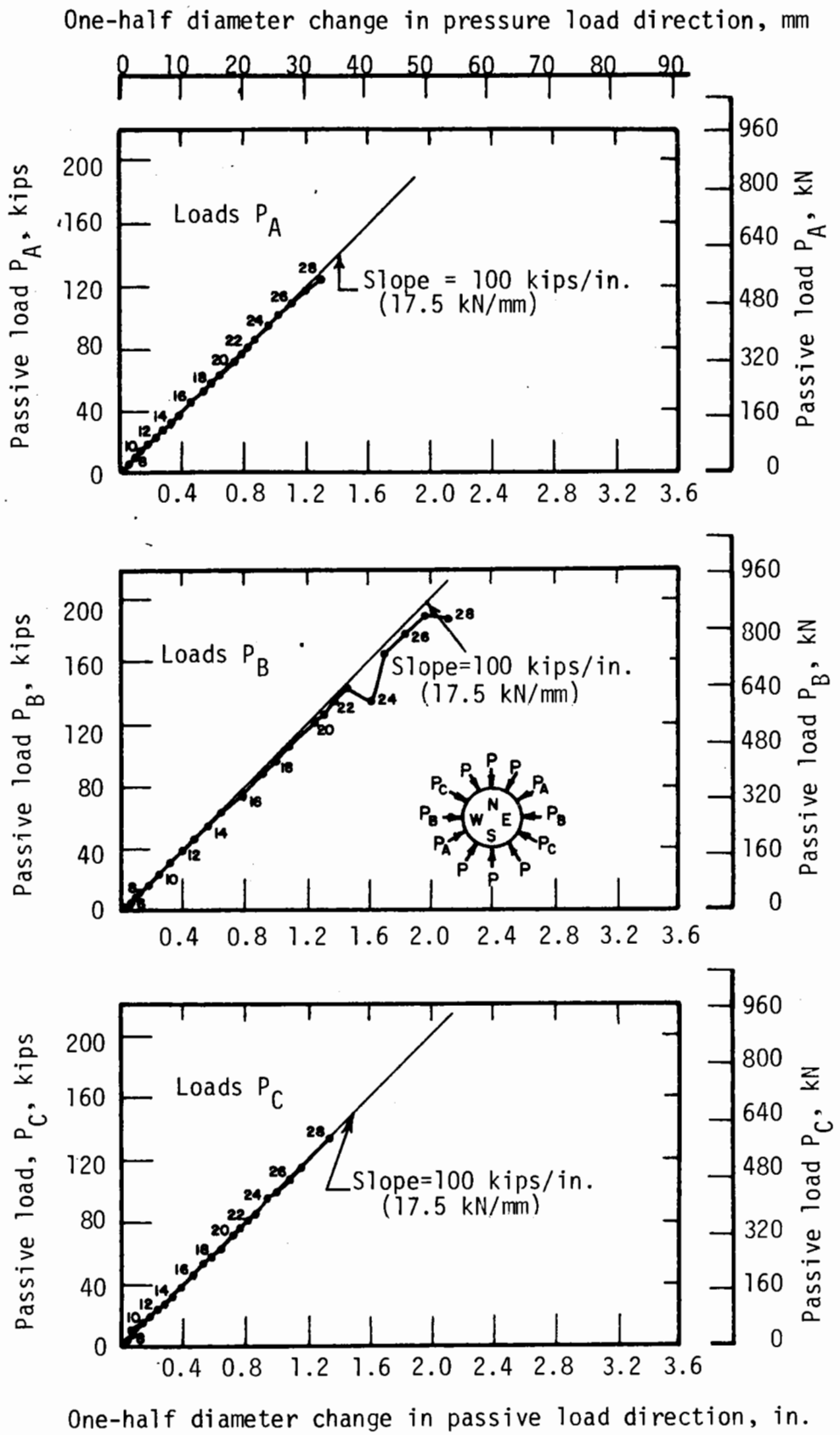

FIGURE 3.16 LOAD-DEFORMATION FOR PASSIVE FORCES IN TEST C5

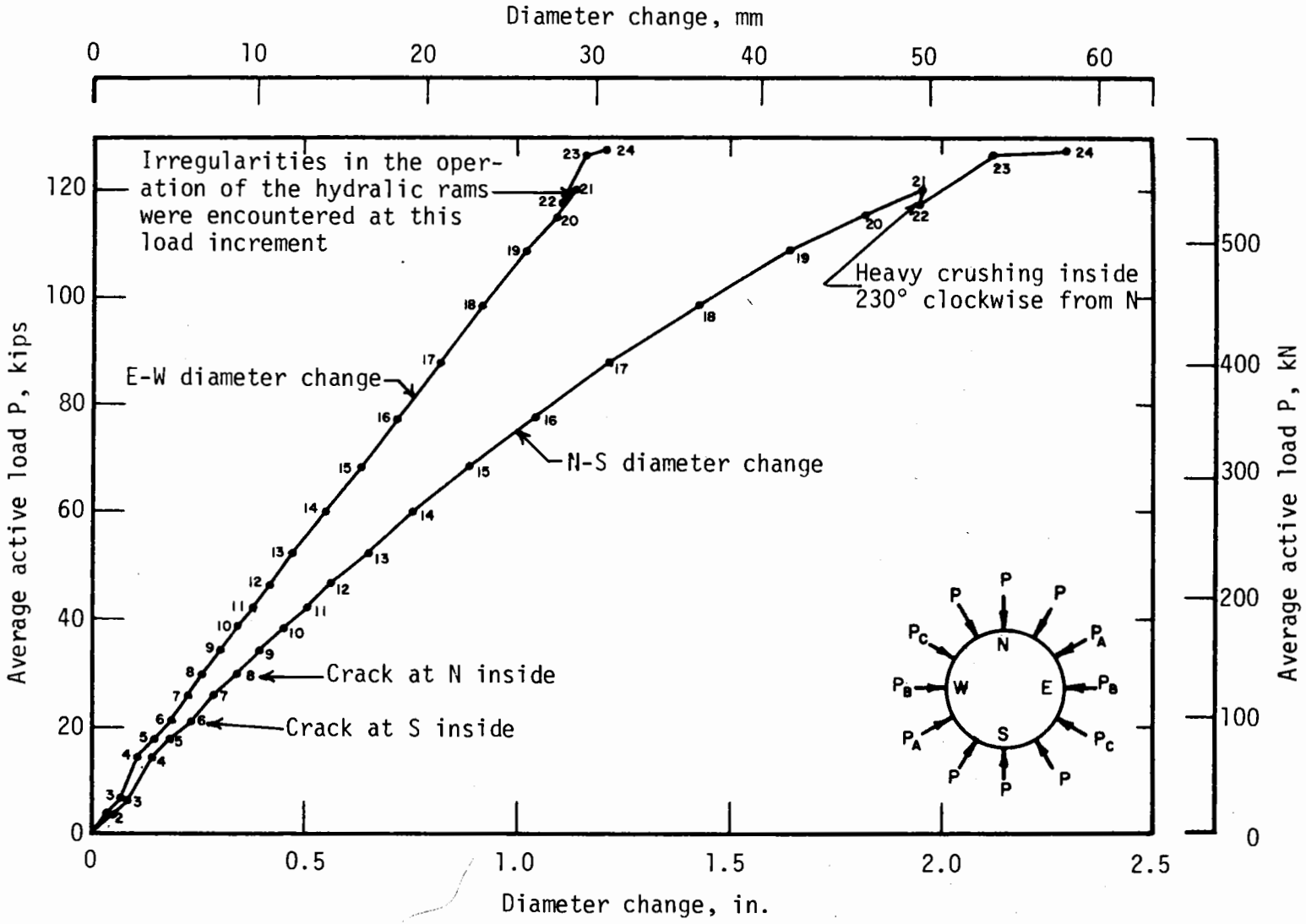

FIGURE 3.17 LOAD-DEFORMATION FOR TEST C3

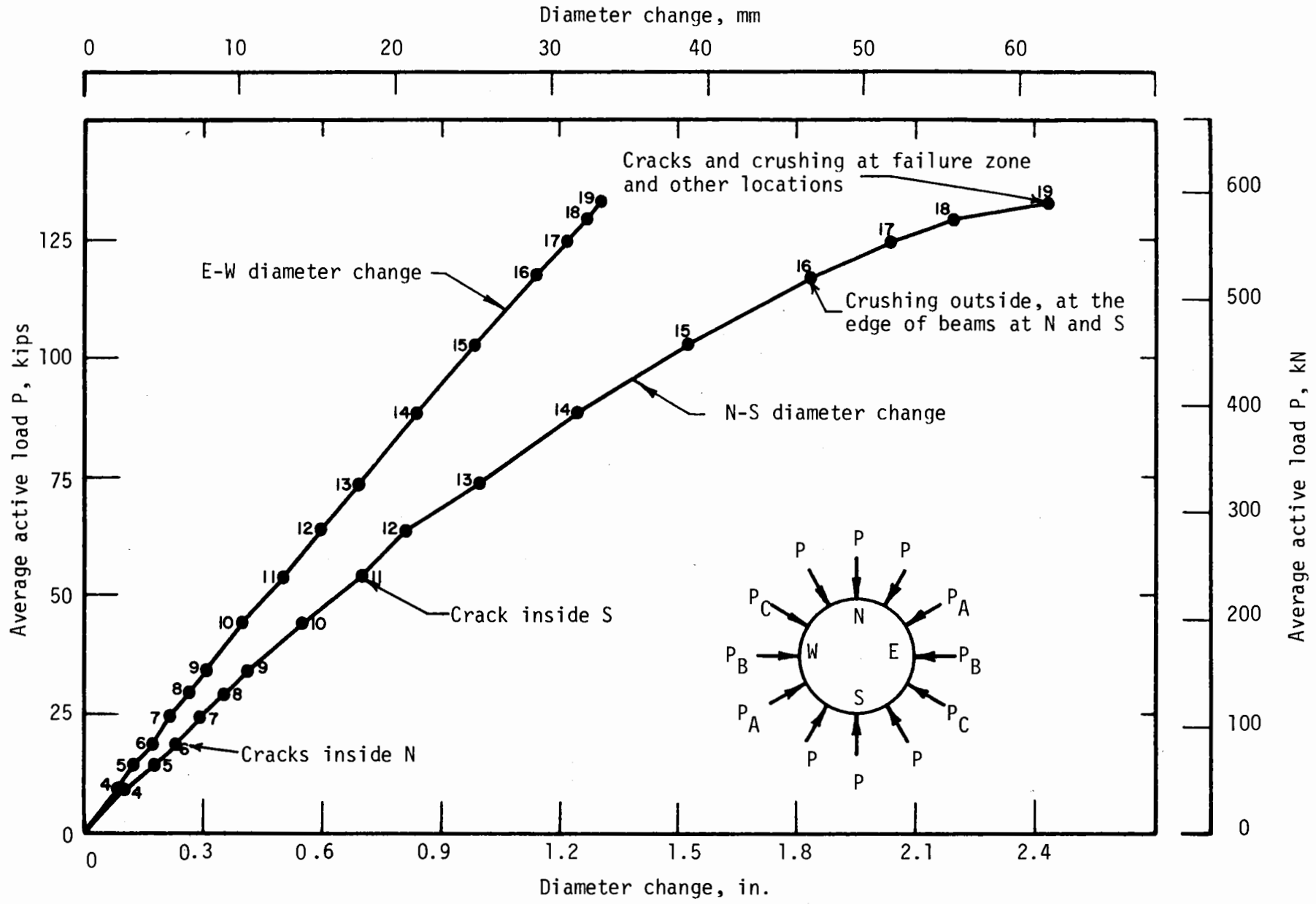

FIGURE 3.18 LOAD-DEFORMATION FOR TEST C6

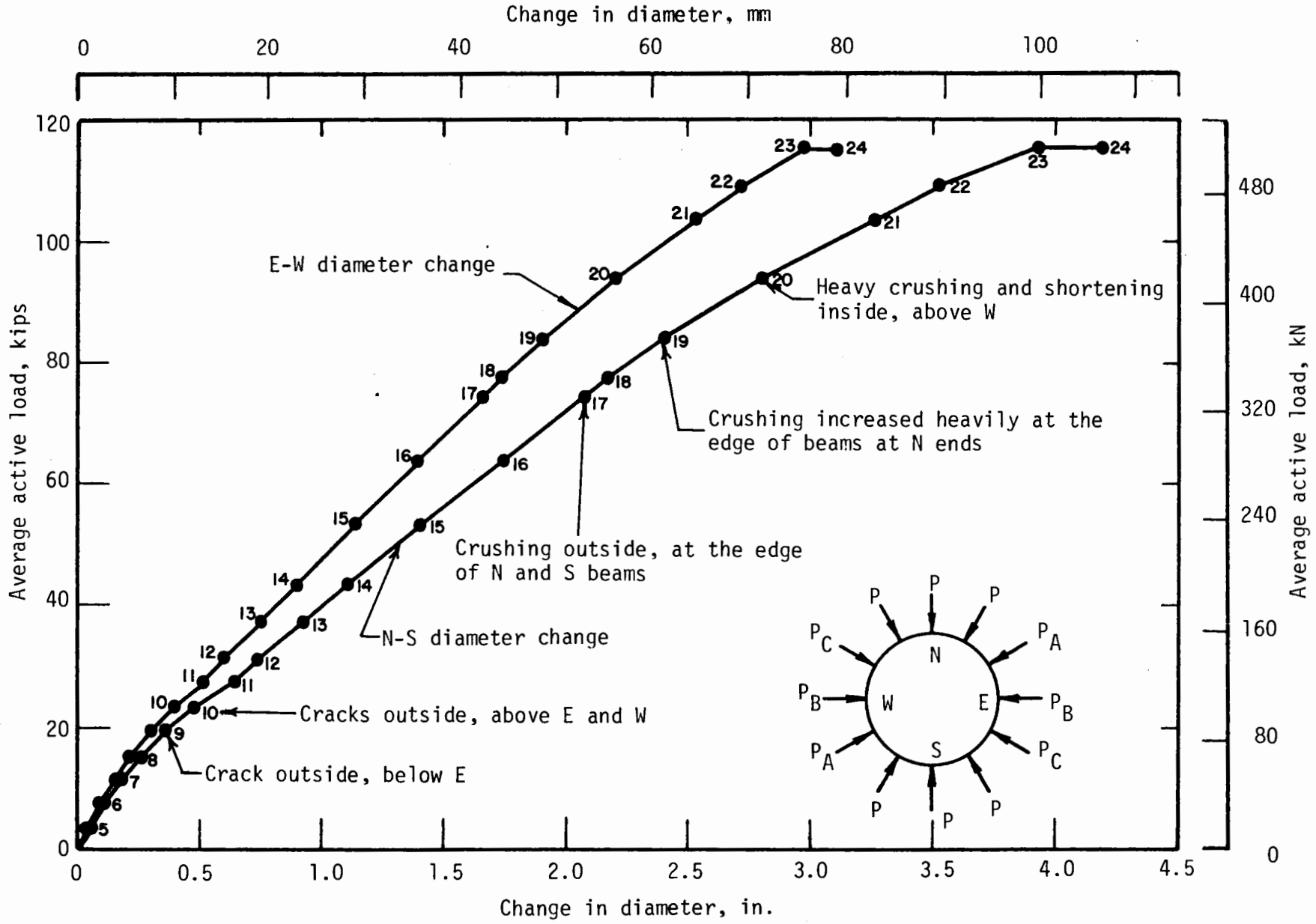

FIGURE 3.19 LOAD-DEFORMATION FOR TEST C4

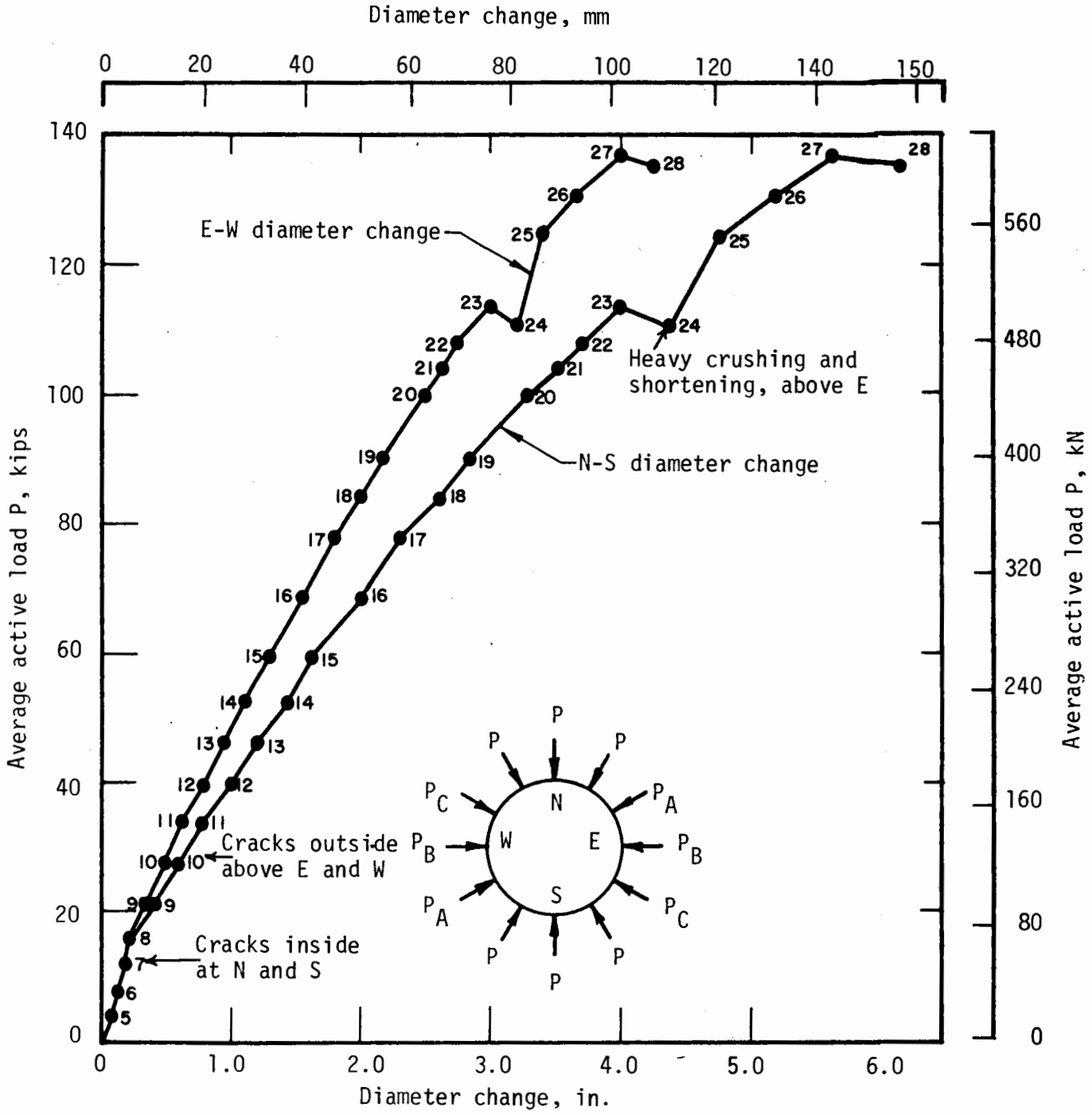

FIGURE 3.20 LOAD-DEFORMATION FOR TEST C5

For the low strength specimens, C3 and C6, the north-south diameter change curves are smooth and nonlinear with the deformation increasing faster than a linear relationship. The flexural cracks are associated with small changes in slope at relatively low load as noted on the curves in Fig. 3.17 and 3.18. In contrast the east-west diameter change curves are almost linear throughout the test. The drop in active load at increment 22 for specimen C3 (Fig. 3.17) is associated with irregularities in the operation of the hydraulic rams.

For the higher strength specimens, C4 and C5, both load-diameter change curves are rather smooth and nonlinear with the same general shape as the curves for the weak concrete specimens. The occurrence of events such as initiation of large flexural cracks, heavy crushing and spalling can be associated with sudden and well defined changes in slope in the path as shown in Figs. 3.19 and 3.20. During the application of load increment 21 for specimen C4 sudden crushing of the compression side at a flexural crack, followed by closing of the tension crack was observed but did not produce an irregularity in the curve because instrumentation readings were not taken at that load. During the testing of C5 this phenomenon was observed more carefully, and it occurred during application of load increment 24. Instrumentation readings were taken just after this occurred which indicate an abrupt drop in average active load P and an increase in deformation, as shown in Fig. 3.20. As in the low strength specimens, at high load levels, especially at the load increment preceding failure, the curves flatten considerably.

3.3 LOAD DISTRIBUTION DURING TESTS

The relations between the average active load P and the passive forces (P_A, P_B, P_C) are presented in Figs. 3.21 to 3.24. The east-west loads (P_B) are always larger than those on either side of it (P_A and P_C) for all the tests. The curves for P_A and P_C are close together for all the tests, which is an indication of the symmetry of loading. The distribution of loads on all the specimens, i.e., the ratio between the various passive forces and the active load, changed during the test as a result of the changing stiffness of the specimen due to cracking, non-linear material properties and geometry change.

The variation of the P_A/P and P_B/P ratios, as the active load P increased, is shown in Figs. 3.25 and 3.26 for the low-strength specimens, and in Figs. 3.27 and 3.28 for the high-strength specimens. On those figures the occurrence of major cracks, presented in Figs. 3.1, 3.4, 3.7 and 3.10, is also noted.

3.4 INTERNAL FORCES

3.4.1 DETERMINATION OF INTERNAL FORCES

Twelve external radial forces were applied to the liner specimens as shown in Fig. 2.3 and tangential forces were introduced at the north, south, east and west positions by the reactions of brackets preventing the specimens from rotating, as discussed in Section 2.3. The specimen thus loaded was statically indeterminate both externally and internally. There were 4 external unknown bracket forces (tangential forces) and three internal

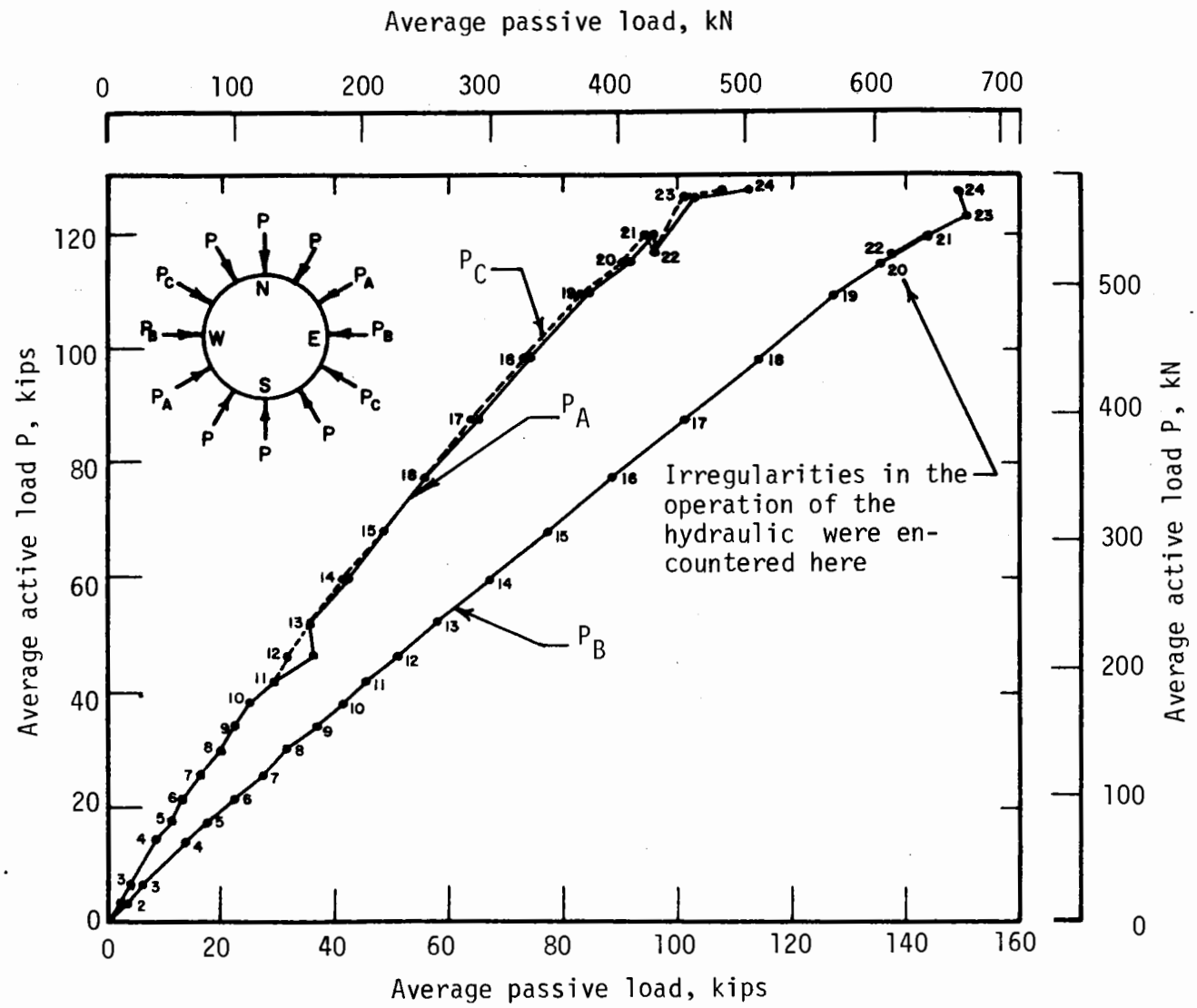

FIGURE 3.21 ACTIVE-PASSIVE LOADS FOR TEST C3

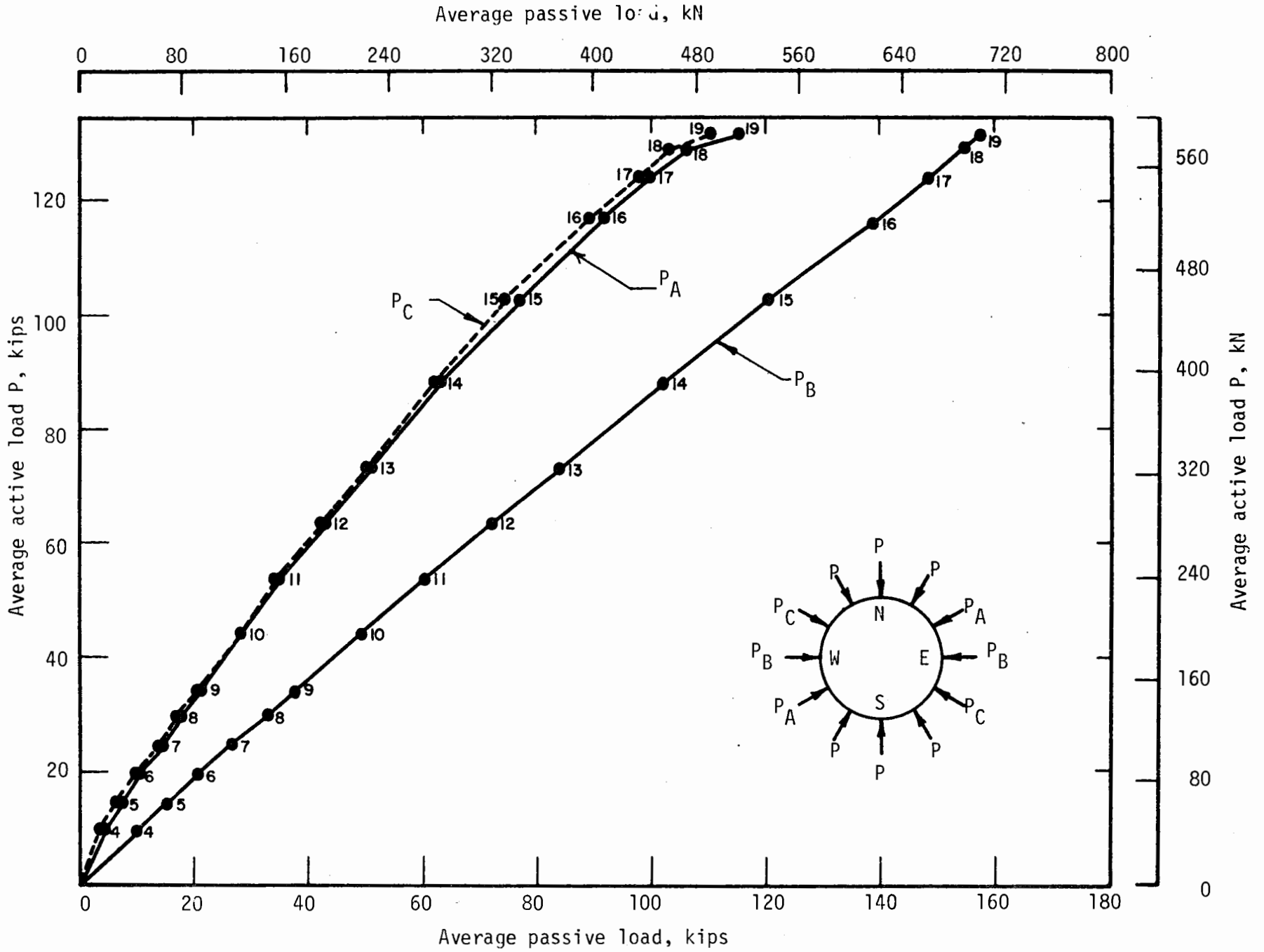

FIGURE 3.2 2 ACTIVE-PASSIVE LOADS FOR TEST C6

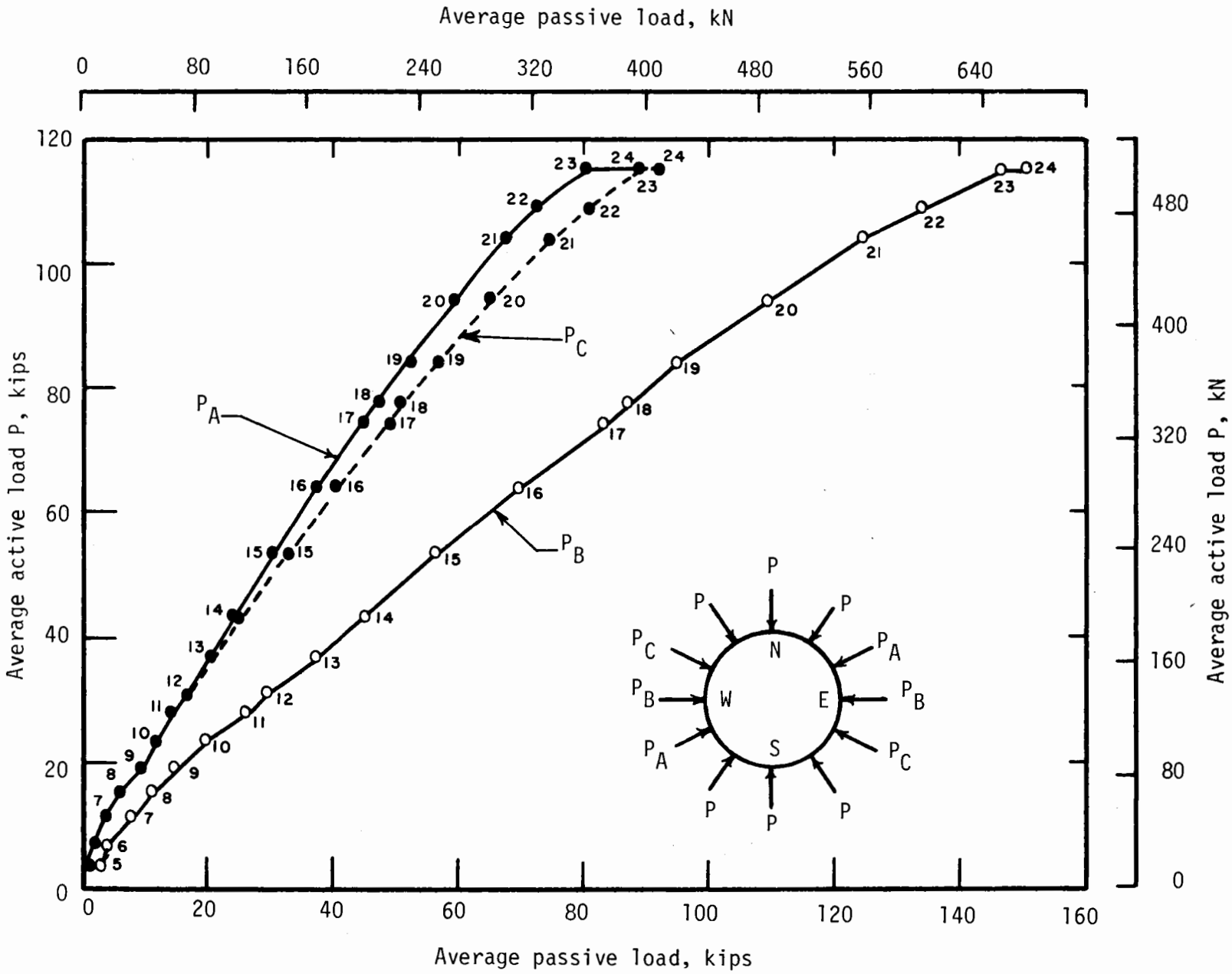

FIGURE 3.23 ACTIVE-PASSIVE LOADS FOR TEST C4

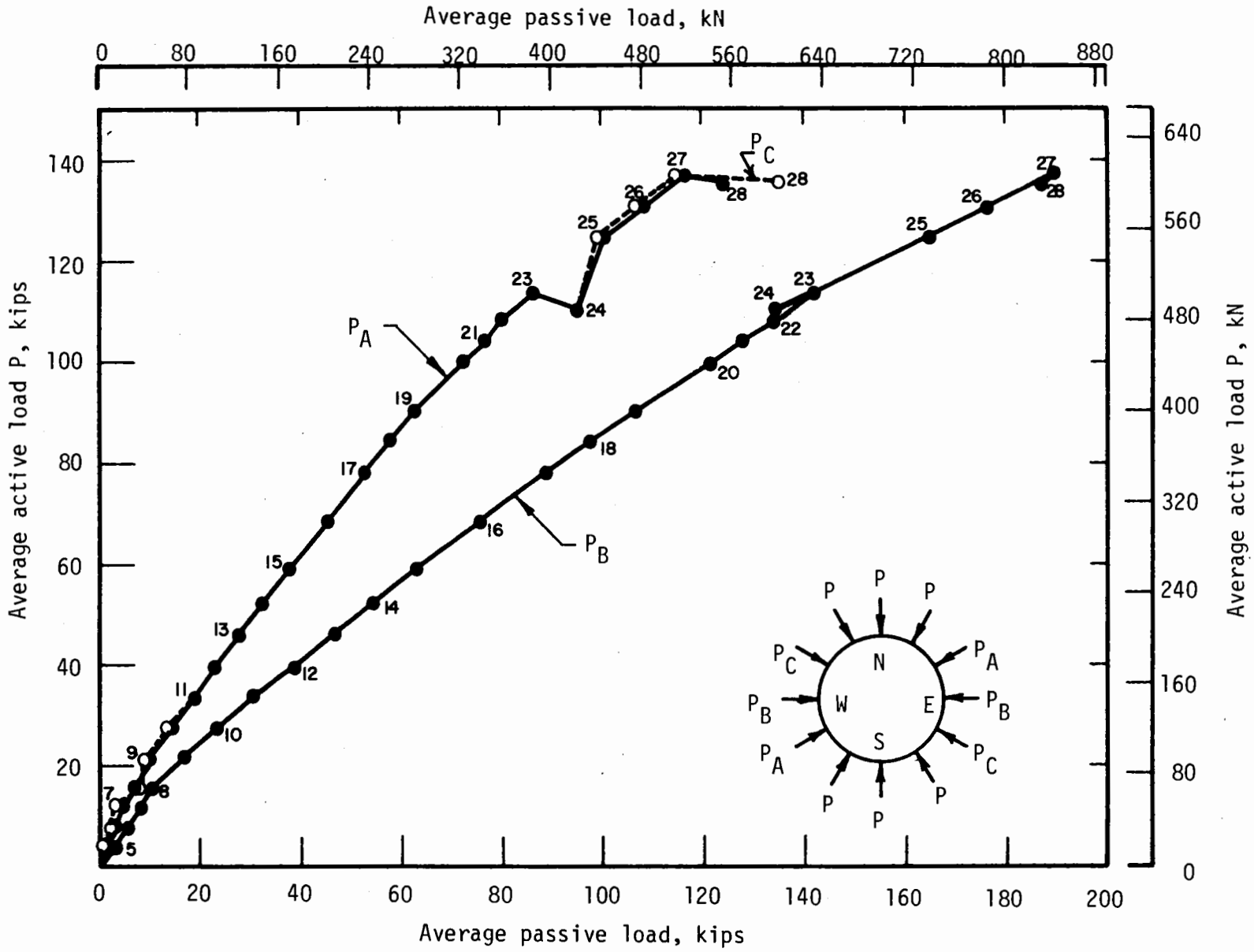

FIGURE 3.24 ACTIVE-PASSIVE LOADS FOR TEST C5

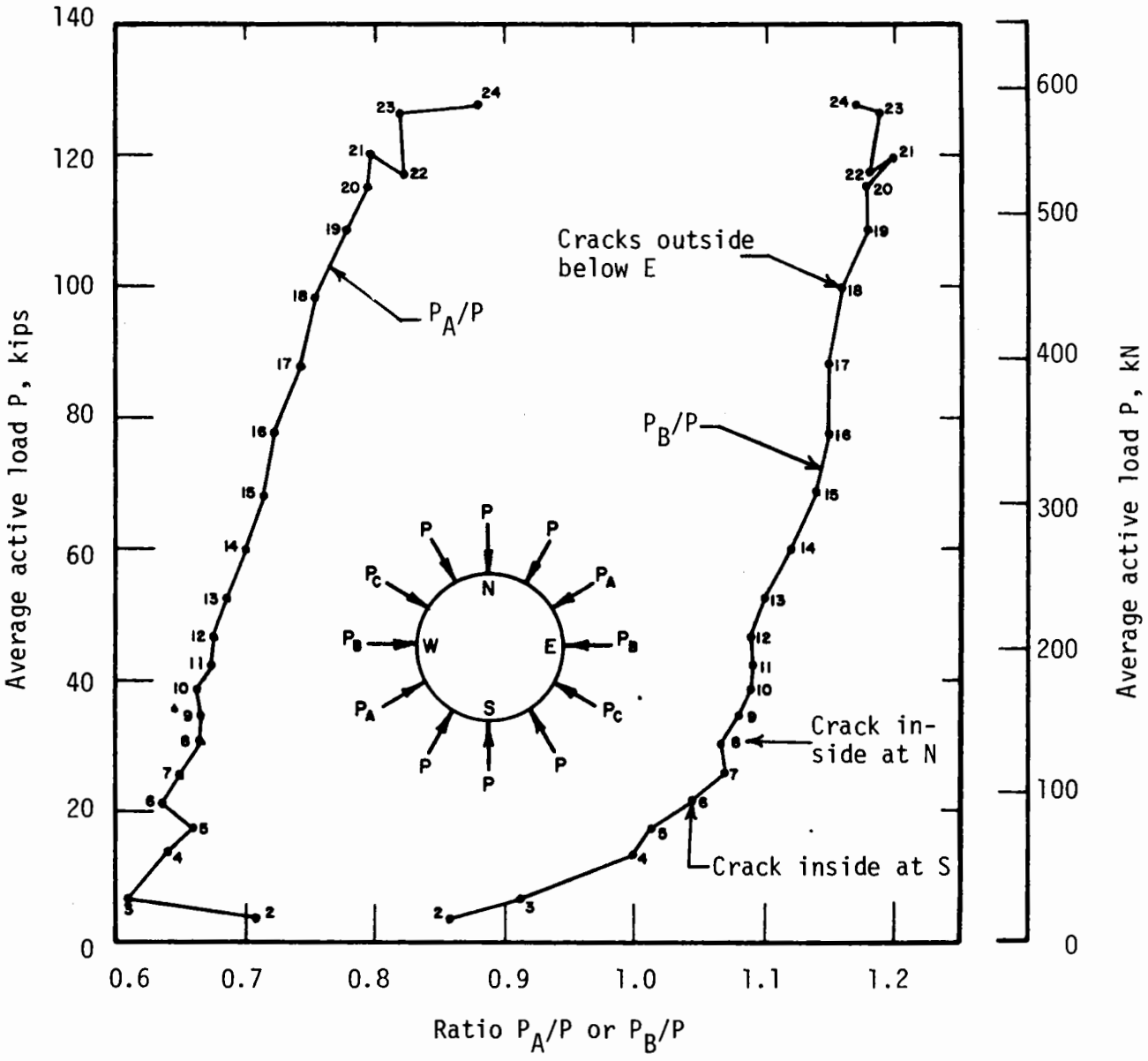

FIGURE 3.25 VARIATION OF PASSIVE-ACTIVE LOAD RATIO DURING TEST C3

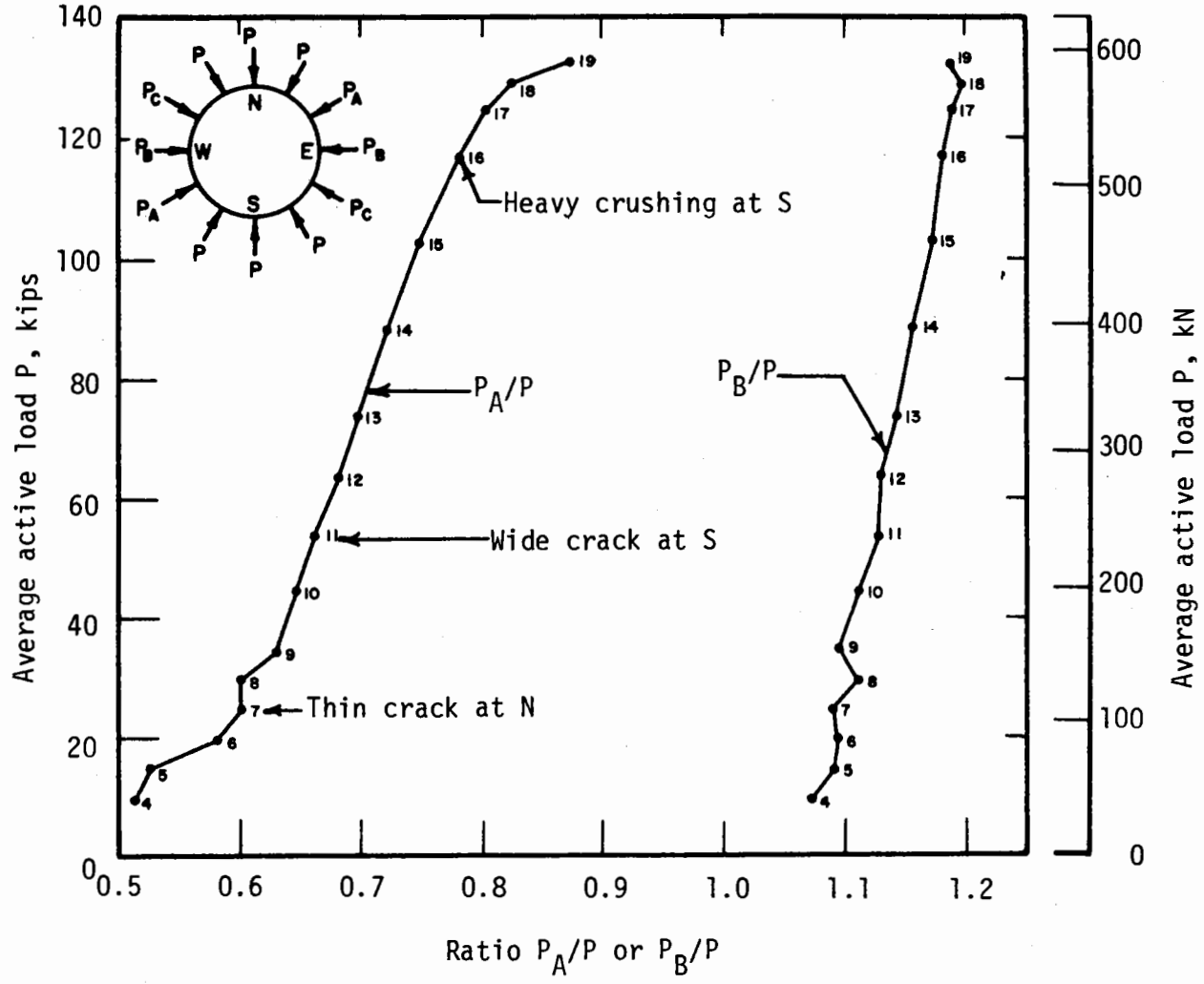

FIGURE 3.26 VARIATION OF PASSIVE-ACTIVE LOAD RATIO DURING TEST C6

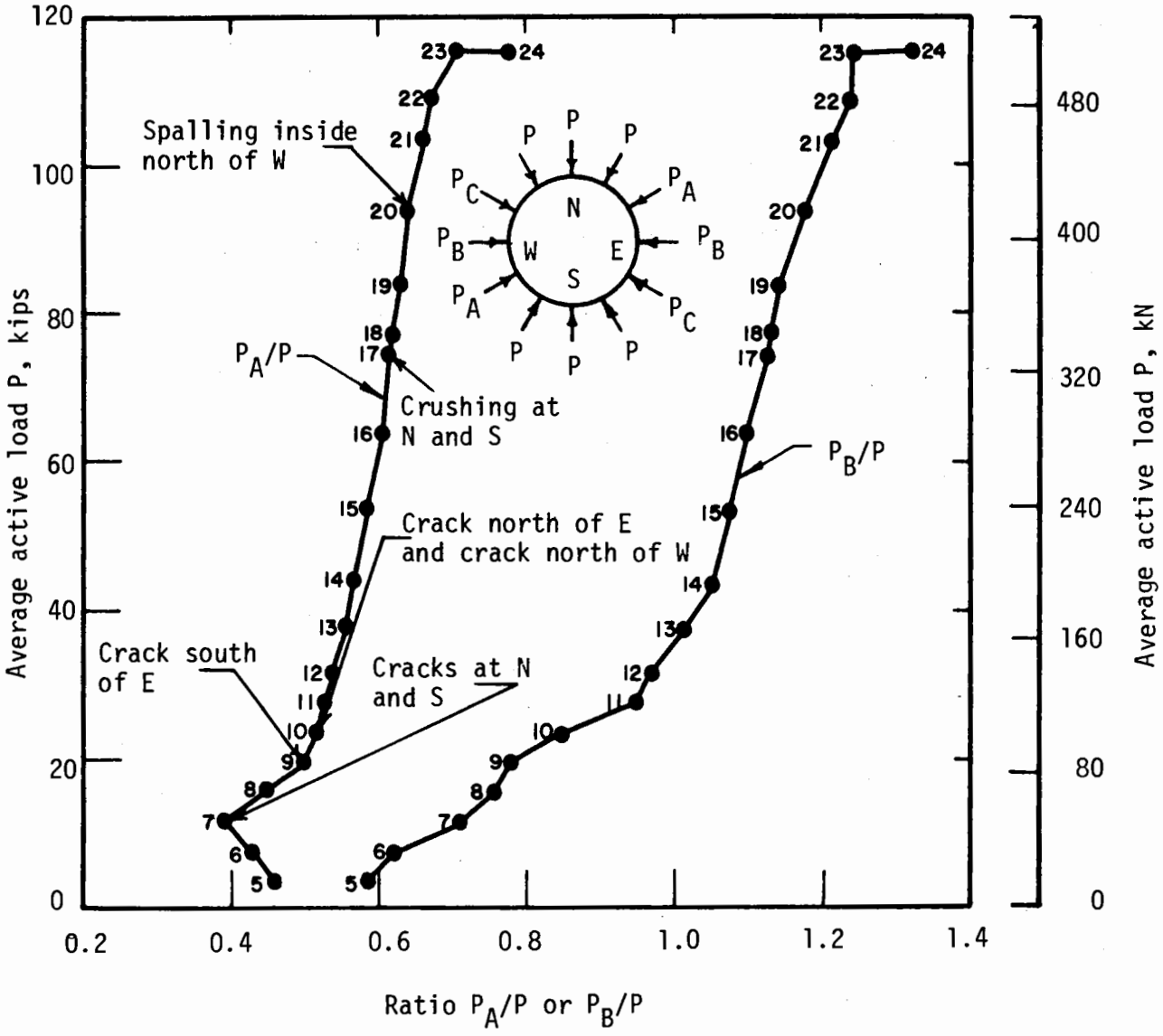

FIGURE 3.27 VARIATION OF PASSIVE-ACTIVE LOAD RATIO DURING TEST C4

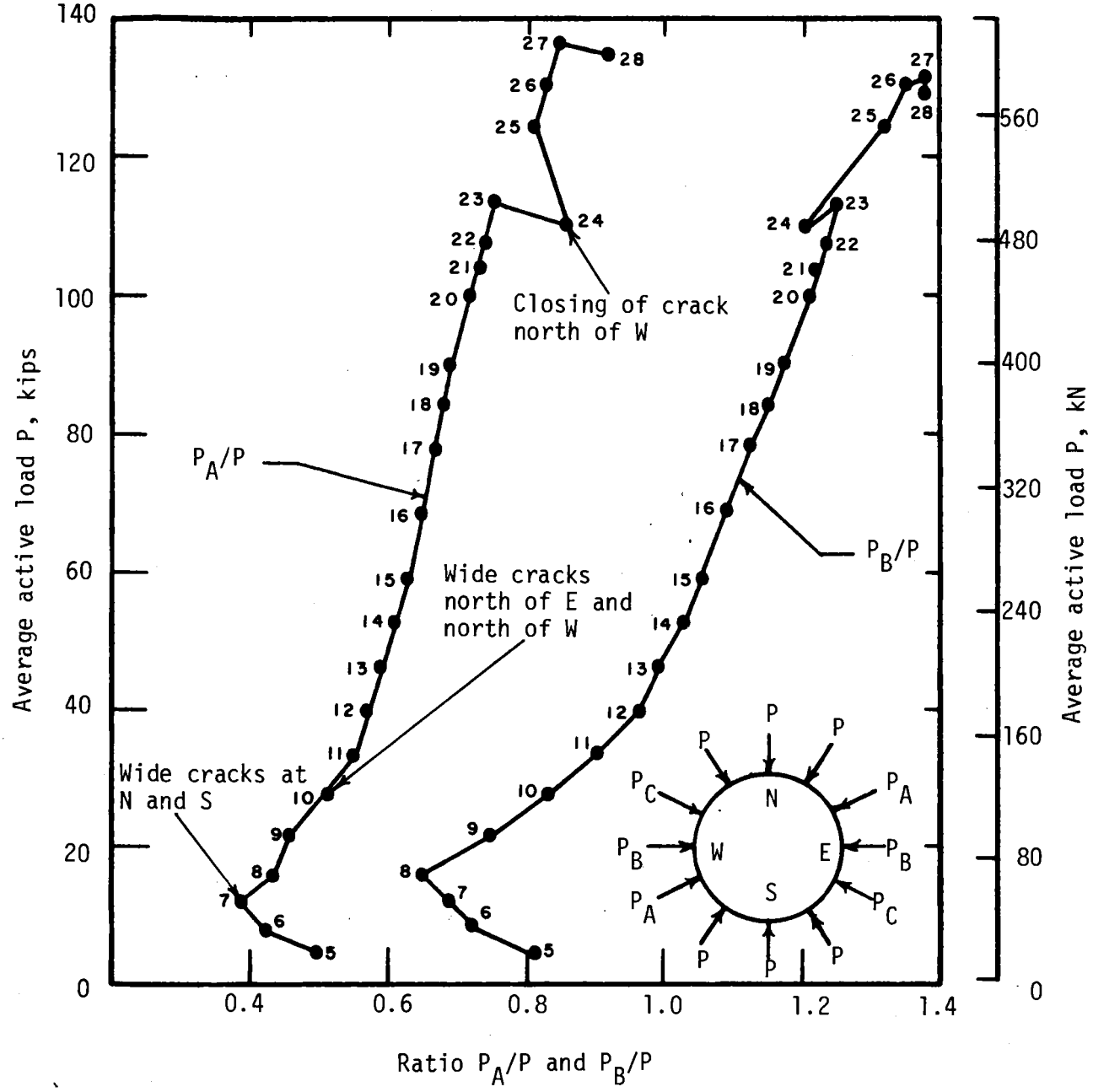

FIGURE 3.28 VARIATION OF PASSIVE-ACTIVE LOAD RATIO DURING TEST C5

unknowns (axial thrust, shear and moment at any section). Four inflection points were located in the specimens by placing strain gages near the quarter points, in order to locate points where inside and outside strains were equal. Location of these four points provides four additional moment equations, and these combined with the three external equilibrium equations provide sufficient information to determine all the unknowns. Also, with the internal forces known at one section in this process, it was possible to determine from statics the thrust, shear, and moment at any other section in the liner. These quantities were then calculated at 5-deg intervals around the liner and at each edge of the load spread beams.

The points of zero moment were located by plotting the strain measured on the inside and outside of the specimen against the position on the specimen in the same graph. The position on the specimen that had constant strain through the section occurred where the curves through these two sets of data crossed. There were twelve data points for each curve, which allowed determination of reasonably accurate curves and a basis for discarding those strains that appeared to be incorrect. In some cases uncertainty existed as to the location of the inflection points, and graphs were plotted of load vs location of inflection point in order to establish the trend of inflection point movement so as to determine the location of those for which the data was inconclusive. However, some error in determining the internal forces may result from errors in location of points.

It was found by Paul, et al. (1974) that the inclusion of change of geometry in the computations gave differences in bending moments up to

25 percent from those which were based on the original geometry of the structure. To account for this, in performing the structural computation for each load increment, the specimen radius was corrected at each load point by one half the change in diameter measured during the test. This implies that the deformations were symmetrical. Between each measured diameter change the correction to the radius was assumed to vary linearly.

The magnitude of calculated internal thrust and shear was not sensitive to location of the inflection points or to the resulting calculated tangential forces. More sensitivity was noted in the moments, however, as a result of changes in the tangential forces. These forces were found to be in the range of 2 kips (90 kN) on less for most of the loading range, although at the last load increment some of them were as high as 8 kips (36 kN). Their effect on the moments was to produce a jump at the load spread beams equal to the force multiplied by the lever arm from the center of the liner section to the rollers on the bracket. The lever arm was about 6 in. (125 mm) long.

3.4.2 MOMENT THRUST

Graphs that show the moment-axial thrust paths for sections of greatest distress in each test specimen will be presented and discussed. Specimens C3 and C6 were made of concrete with about the same material properties and tested under the same condition. Specimens C4 and C5 were made of higher strength concrete with similar properties and were subjected to the same loading conditions. The material properties and loading are

summarized in Tables 2.2 and 3.1. The liner specimen sections that will be discussed and for which the moment-thrust paths are presented are located by central angles measured clockwise from the north position. Also shown on the moment-thrust graphs is an average calculated failure envelope for the specimen section. The basis for computations of these envelopes will be discussed in the next chapter.

SPECIMEN C3

In Fig. 3.29, the moment-thrust paths for four highly stressed sections in the specimen are presented. The sections are also shown in Fig. 3.1 where observed behavior is described. The most highly stressed section in the failure region was at the east edge of the south load beam, corresponding to an angle of 176.2 deg. The failure region occurred between this angle and 168 deg.

For about two thirds of the test the moment-thrust paths of sections with positive moment (tension inside), such as sections at 3.8 and 176.2 deg, progressed upward curving inward smoothly, and steadily approached the failure envelope. The paths at sections with negative moment, such as sections at 110 and 230 deg, began linear and parallel to the envelope. At load increment 18, the moment at the section at 110 deg reversed and began to decrease. At the same load cracking was detected on the inside, and also at the following increment a major region of crushing was detected on the outside (Fig. 3.1). At the same load increment, the path at the nearby section 176.2 deg (failure section) also changed the rate of increase of moment in the moment-thrust path. At load increment 20,

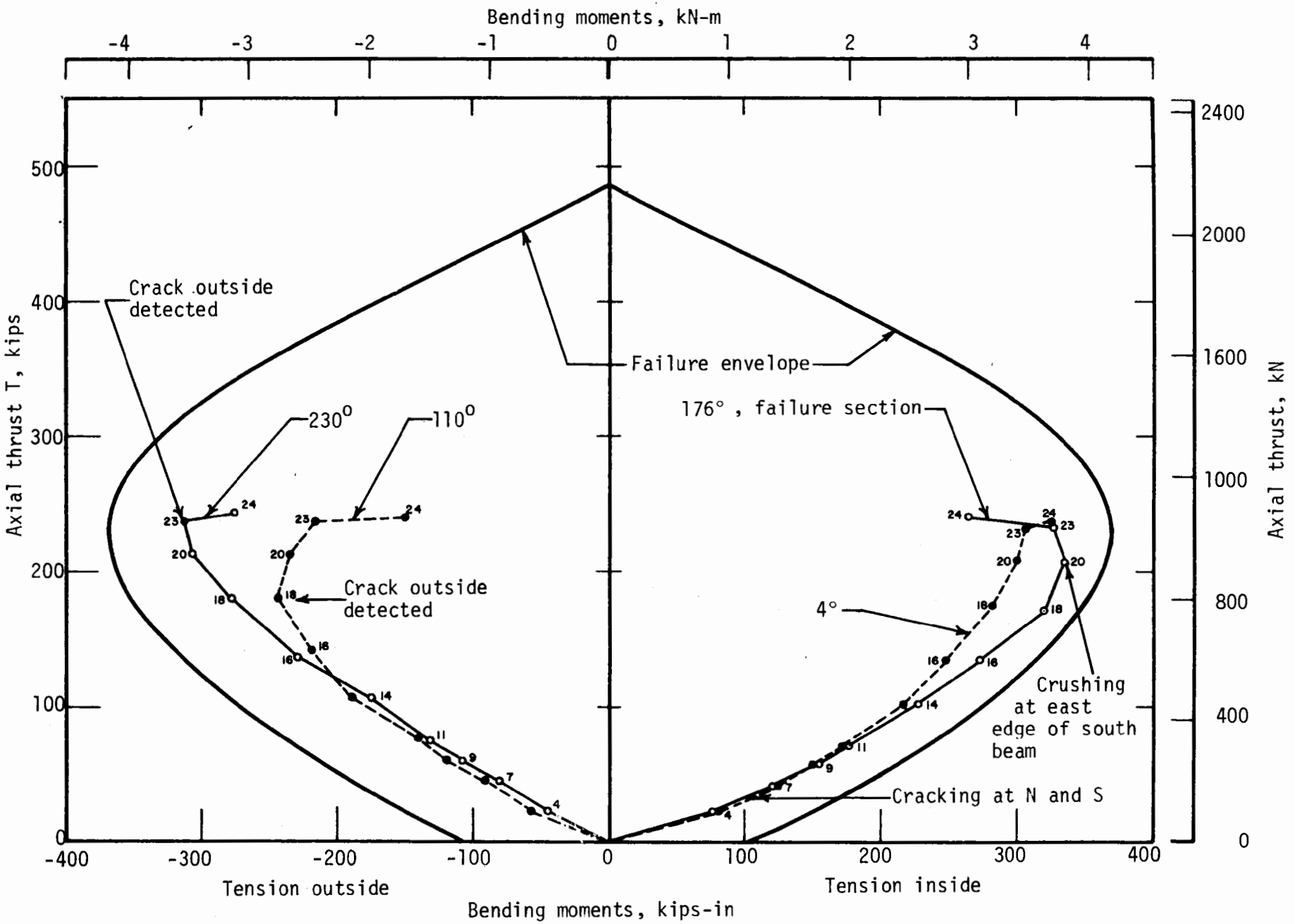

FIGURE 3.29 MOMENT-THRUST PATHS FOR CRITICAL SECTIONS OF SPECIMENS C3

the moment at this failure section reversed and moment began to decrease. It was at this increment that crushing was detected for the first time in that section. Further redistribution of moment began in the remaining paths at this loading. In increments 23 and 24 there occurred a small increase in thrust associated with a large decrease in bending moment at all four sections. This behavior in the last increment is also reflected in the load-deformation curves shown in Figure 3.17 by an increase in deflection at almost constant load.

SPECIMEN C6

Moment-thrust curves for five different sections in specimen C6 are presented in Fig. 3.30. These sections correspond to points of major cracking and/or crushing. Failure of the liner occurred in the region bounded by sections at 236.2 and 228 deg. Failure began in this region at the former section with crushing on the inside and tension cracking outside, and then traveled diagonally to the latter section (Fig. 3.4).

For the sections, at 4 and 176 deg, the paths started curving smoothly inward steadily approaching the envelope up to load increment 13. From that increment the paths separated and at 176 deg curved around as in the previous specimen, while at 4 deg remained almost linear, and toward the end of the test curved slightly outward. The sections were approximately opposite on the liner specimen.

The curves for sections with negative moment at 110, 135 and 228 deg were essentially parallel until the one for 110 deg curved inward, like those in specimen C3, while the curves for 135 and 228 deg remained linear

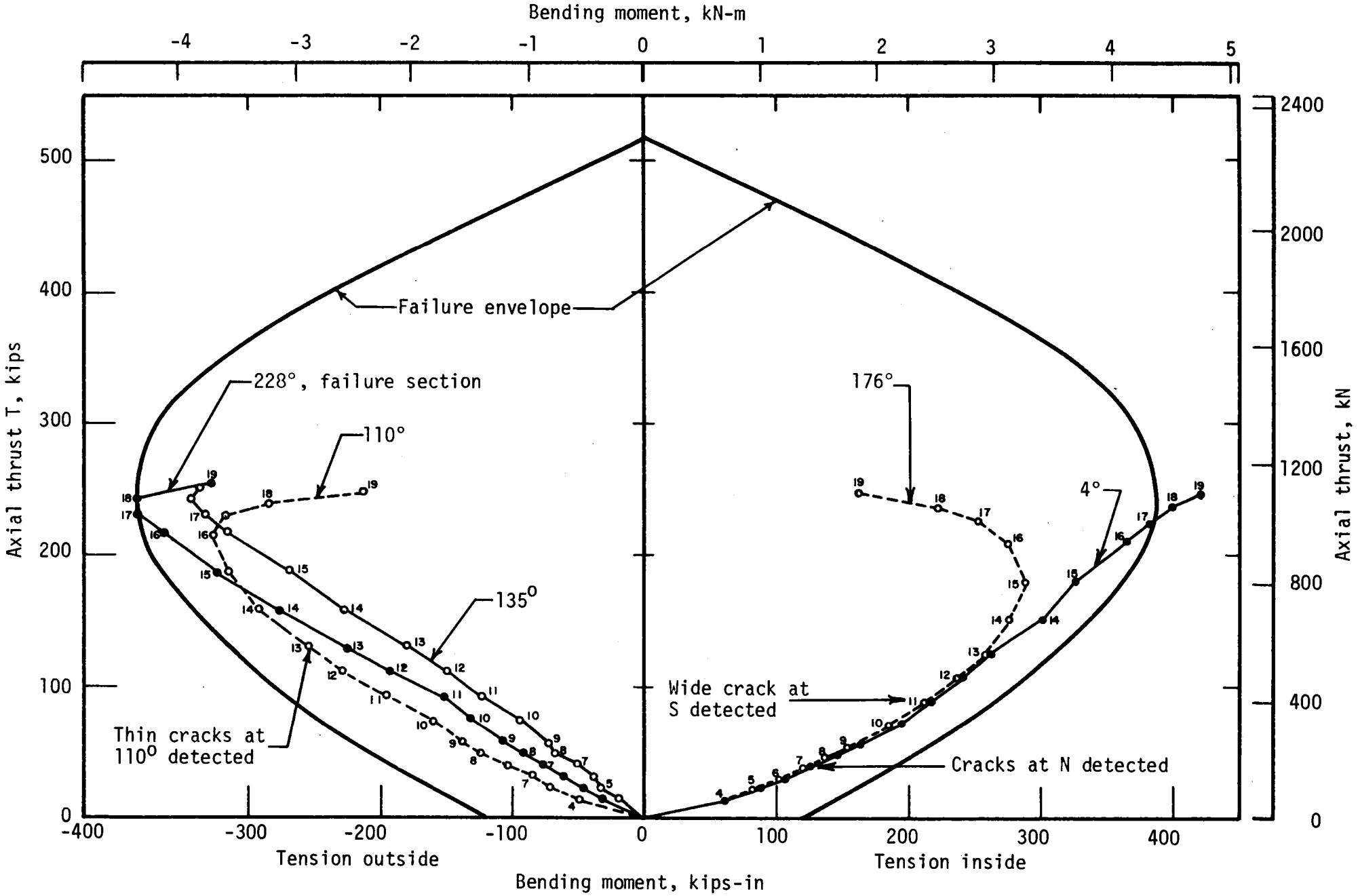

FIGURE 3.30 MOMENT-THRUST PATHS FOR CRITICAL SECTIONS OF SPECIMENS C6

up to increments 17 and 18. The latter two sections were at nearly symmetric locations on the specimen, 42 and 45 deg south of east and south of west, respectively.

At load increments 6 and 7 cracking was first detected on the inside at the north and south sections, but significant changes in the thrust-moment paths did not occur. At increment 11 cracking at the east side of the south beam was detected, but again there was little change in the paths.

At load increments 16, 17 and 19 crushing was observed at sections 176, 110 and 228 (failure) deg, respectively (see also Fig. 3.4). At each section, shortly before the corresponding distress was detected, the moment began to decrease. Each time crushing was detected at a section, changes in the rate of moment increase were observed at some other sections. That is, when crushing occurred at 176 deg, redistribution took place at 110 deg; when the section at 110 deg crushed, the section at 228 deg (failure) redistributed moment. The only section that did not decrease in moment was that at 4 deg, where the moment kept increasing until the end of the test.

Between load increments 18 and 19, a small increase in axial thrust was associated with a large decrease in moment for all sections except at 4 deg.

SPECIMEN C4

The moment-thrust relation for five sections of major cracking and/or crushing, shown in Fig. 3.7, are presented in Fig. 3.31. Positive

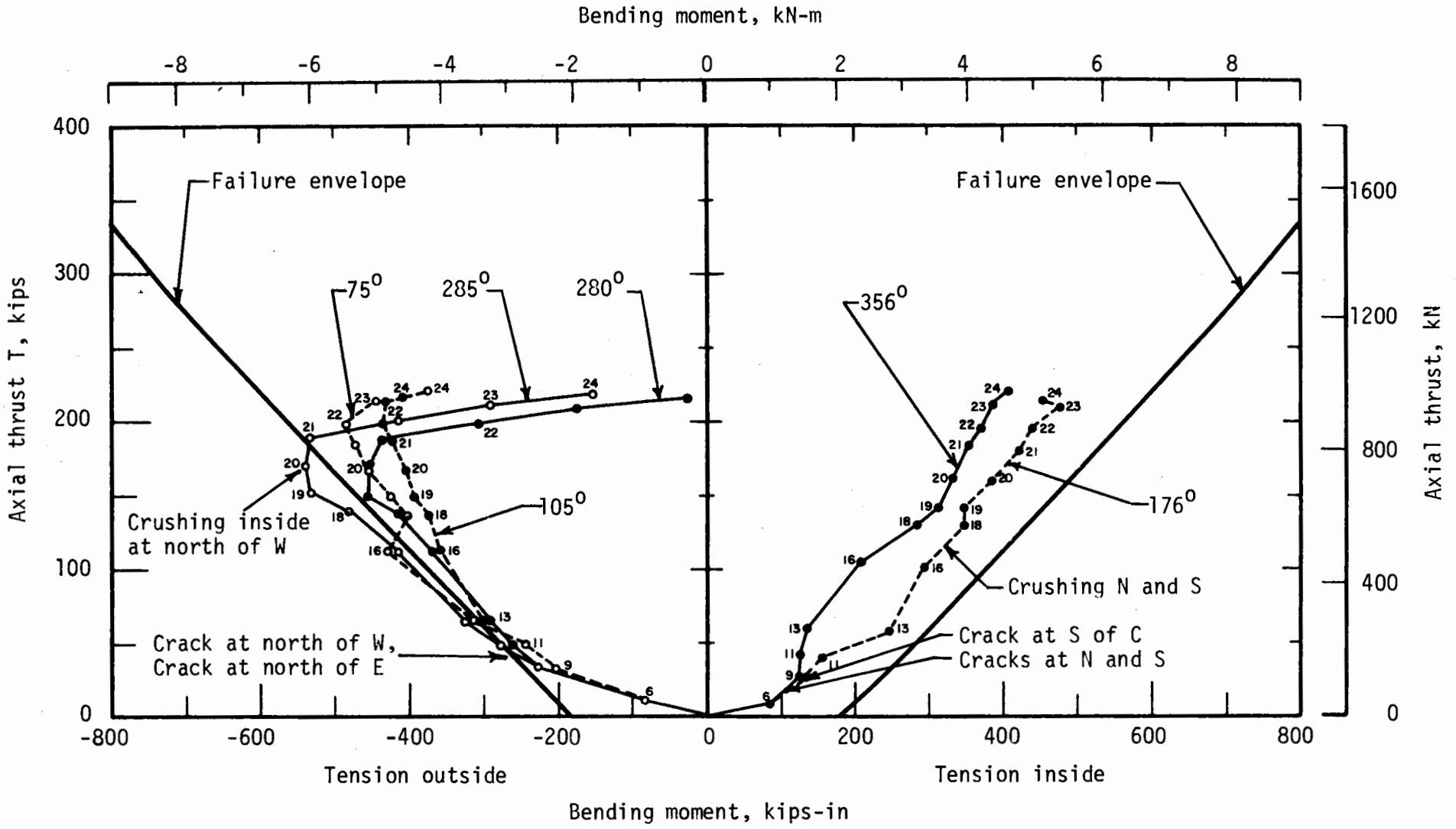

FIGURE 3.31 MOMENT-THRUST PATHS FOR CRITICAL SECTIONS OF SPECIMEN C4

moment occurred at sections at 356 and 176 deg (north and south approximately), and the moment-thrust curves were similar to those for the north section in specimen C6; both paths started with rather flat slopes and when cracking was detected at increment 7 the slopes changed abruptly and the curves became almost linear. The paths then continued without a significant amount of curvature, contrary to those in specimens C3 and C6, and were almost parallel to the failure envelope shown.

At load increments 9 and 10, tension cracking was detected on the outside of the specimen at the sections at 105 and 75 deg, respectively. These sections are symmetrically located 15 deg on each side of the east load point. Crushing occurred opposite the tension cracks at about load increments 22 to 23 when the moment-thrust paths curved inward sharply. Also, during the last increment of loading a large decrease in moment corresponded to a small increase in thrust. The closeness of these curves indicates that the loading and resulting internal forces were nearly symmetrical in this region.

The failure region occurred just north of the west loading beam between angles of 274 and 285 deg. In this negative moment region, cracking started outside at 280 deg and crushing occurred inside at 285 deg. Both paths began identically and linearly approached the envelope at about increment 11, and then curved upward and almost parallel to the envelope. At increment 12 cracking was detected at 280 deg. Spalling was detected on the inside at 280 deg at increment 20; this was also the increment for which the moment began decreasing at both sections in the failure region. At increment 21, when heavy cracking and closing of the tension crack were detected at 285 deg, a large decrease in moment occurred.

SPECIMEN C5

In Fig. 3.32 five moment-thrust curves are presented for the sections where major cracking and/or crushing occurred as shown in Fig. 3.10. At sections with positive moment near the north and south (sections at 356 and 180 deg) the paths began linearly, and at increment 7 when cracking was detected at both sections, the curves abruptly changed slop and continued upward. This behavior is similar to that of the sections at the same position in specimen C4. The curve for the section at 180 deg curved slightly inward, while that for 356 deg continued parallel to the envelope and then curved outward. In the last load increment both sections had an abrupt decrease in moment.

The failure region was bounded by the edge of the west load beam at 274 deg and the section at 285 deg, where crushing was detected inside. Cracking began on the outside at 280 deg. This failure region is the same as in specimen C4. The behavior of sections at 280 and 285 deg together with the section at 70 deg, where cracking outside and crushing inside were detected at the same loads as the failure region, is shown in the negative moment region. The section at 70 deg was located nearly symmetrically to that at 280 deg but on the other side of the specimen. The shape of the curves for these two sections are very similar, indicating reasonable symmetry.

All three curves in the negative moment region began linearly and are almost identical until the failure envelope is reached. Shortly after increment 10, cracking was detected at 280 and 70 deg and by the end of increment 11 all the curves had changed slope, separated and continued

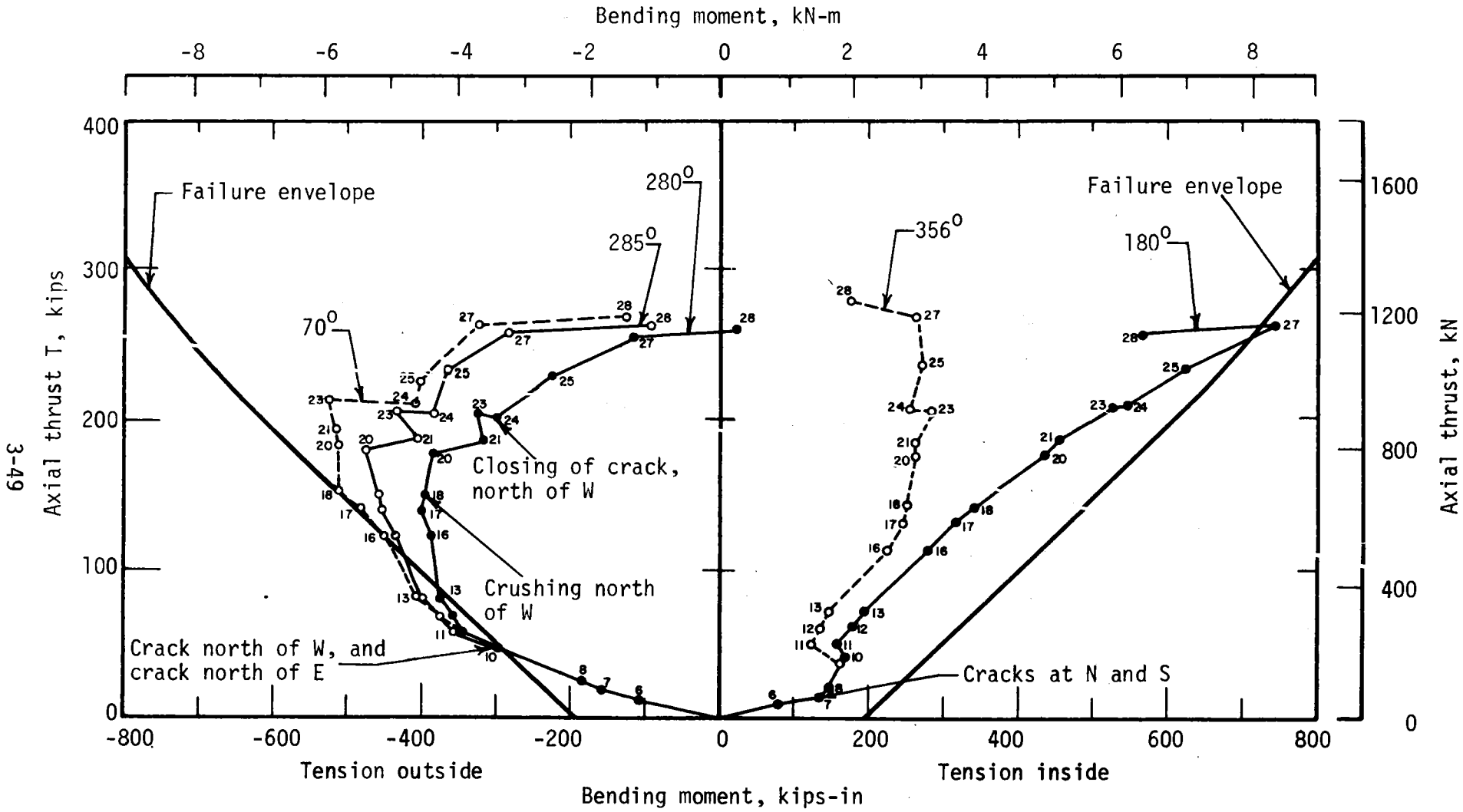

FIGURE 3.32 MOMENT-THRUST PATHS FOR CRITICAL SECTION OF SPECIMEN C5

with an inward trend. Crushing was observed at 70 and 285 deg at increment 17 and moment became constant at the 70 deg section. At load increment 21, heavy crushing and closing of the tension crack occurred at 285 deg and there was an abrupt decrease of moment that causes a jump in the curves for 280 and 285 deg at the same load. The same decrease in moment occurred for the section at 70 deg at increment 23, when crushing and shortening occurred at that section.

At the last increment recorded a large decrease in moment corresponded to a small increase in axial thrust. The general shape of the curves for the sections with negative moment is similar to those in specimen C4, though the curvature is more gradual in specimen C5.

CHAPTER 4

MOMENT-THRUST FAILURE ENVELOPE

4.1 DETERMINATION OF STRESS-STRAIN PROPERTIES

4.1.1 COMPRESSION

A series of concentrically loaded standard 6 x 12 in. (15.2 x 30.4 cm) compression cylinders were tested in a stiff testing machine with deformation control, to obtain the stress-strain curve in compression for representative samples of concrete used in the liner specimens. The cylinders were cast from the batch of concrete used for each liner specimen and cured under the same conditions. Load was applied in a 300 kip (1334 kN) capacity "MTS" testing machine with the capability to maintain a constant rate of head movement throughout the test. This capability of the machine and its large stiffness prevents large deformation when the peak of the curve is passed, so the specimen is not destroyed and the descending branch of the stress-strain curve can be recorded. A rather slow rate of deformation is also necessary near the peak load to get the descending branch, and this slower rate influences the peak stress obtained. For this reason the peak stress of the stress-strain curve does not agree with the f'_c obtained from averaging several standard control cylinder tests.

Two different deformation rates were used: they were 0.03 and 0.015 in./min (0.0762 and 0.0381 cm/min). It was found, especially for specimens with fly ash in the mix, that the specimen strength was smaller

with the slower rate, but the number of tests was not sufficient to establish a quantitative comparison.

Cylinder deformation was measured with a compressometer with a gage length of 6 in. (152 mm) centered at the midheight of the specimen. The compressometer consists of 2 rings 6 in. (152 mm) apart attached to the specimen with pointed set screws and provisions for measuring the relative movement of the rings with an LVDT. The output of the load cell of the testing machine, and of the LVDT, were connected to the 'Y' and to the 'X' axis, respectively, of a X-Y recorder. Thus, a continuous recording of the load and deformation was obtained.

The shape of the stress-strain curves obtained in this way were different from that of ordinary concrete in that the peak of the curve occurred at strains ranging from 0.0035 to 0.0045. These values are somewhat larger than that of 0.002 usually obtained for ordinary concrete specimens without steel fiber tested according to the ASTM standard rate (ASTM C39-72).

The modulus of elasticity listed in Table 2.2 was obtained as the initial slope of the curves. In the same table, the modulus as computed from the ACI formula is listed. The formula predicts values about 50 percent higher than the measured ones.

4.1.2 FLEXURAL TENSION

Flexural tension stress-strain curves for representative samples of the steel-fiber-reinforced concrete used in the liner specimens were obtained from tests and the computational procedures described in this section. The tension stress-strain properties of primary interest are

those for an element of beam surrounding a flexural crack. The objective is to obtain stress-strain curves that can be used to describe the behavior of elements in a tunnel liner that have cracked. If the curves obtained in these simple tests can be used to predict the structural behavior, then they will serve their purpose even if they do not accurately relate stress and strain at a point. It is with this idea that the technique for obtaining the curves was developed.

DESCRIPTION OF TESTS

Eleven 6 x 6 x 60 in. (15.2 x 15.2 x 152 cm) steel-fiber-reinforced concrete beams were tested with 2-point loading to obtain the load-deflection history. The beams were cast during the same operation as the liner specimens and cured under the same conditions; therefore the material properties of these specimens were representative of those of the corresponding liner specimens.

The testing scheme, geometry and instrumentation layout are shown in Fig. 4.1 and photographs of the test arrangement are shown in Fig. 4.2. Two symmetrically placed concentrated loads were placed 10 in. (254 mm) from each support to provide a long constant-moment region. The computational procedure was easier and more accurate if relative deflection of a portion of the beam in this constant-moment region was used. Thus, the loads were placed 40 in. (1016 mm) apart and the relative deformation measured was in a 36 in. (914 mm) portion centered between the loads.

The specimens were tested in a "MTS" hydraulic testing machine with 300 kips (1334 kN) capacity. The head movement of the machine was

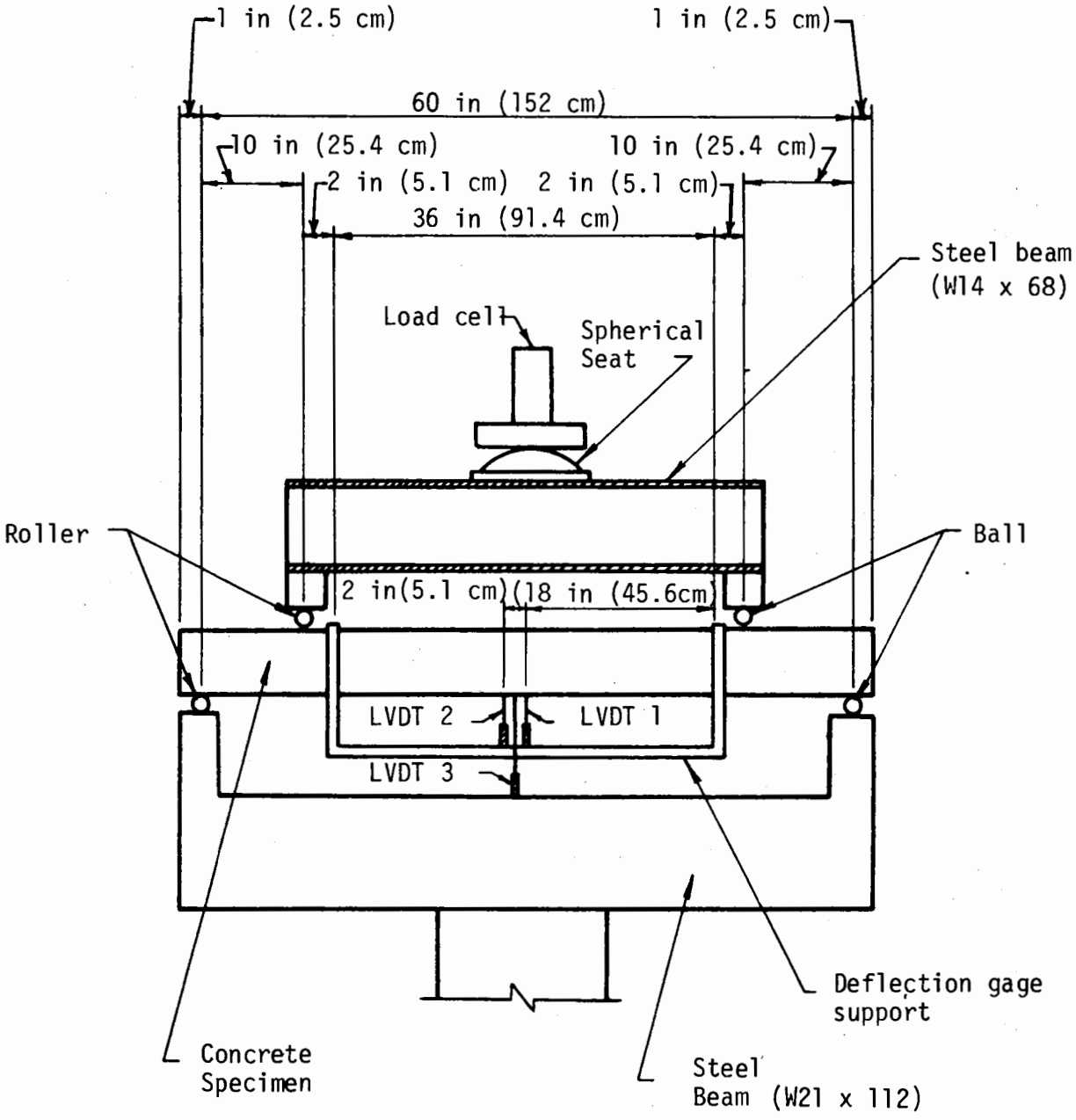

FIGURE 4.1 TEST ARRANGEMENT FOR BEAMS

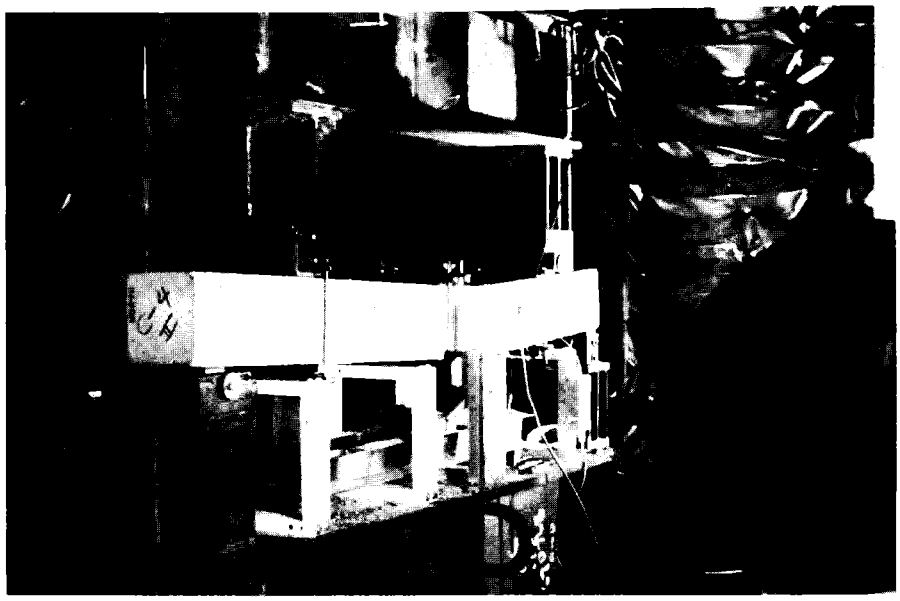

(a) Test arrangement

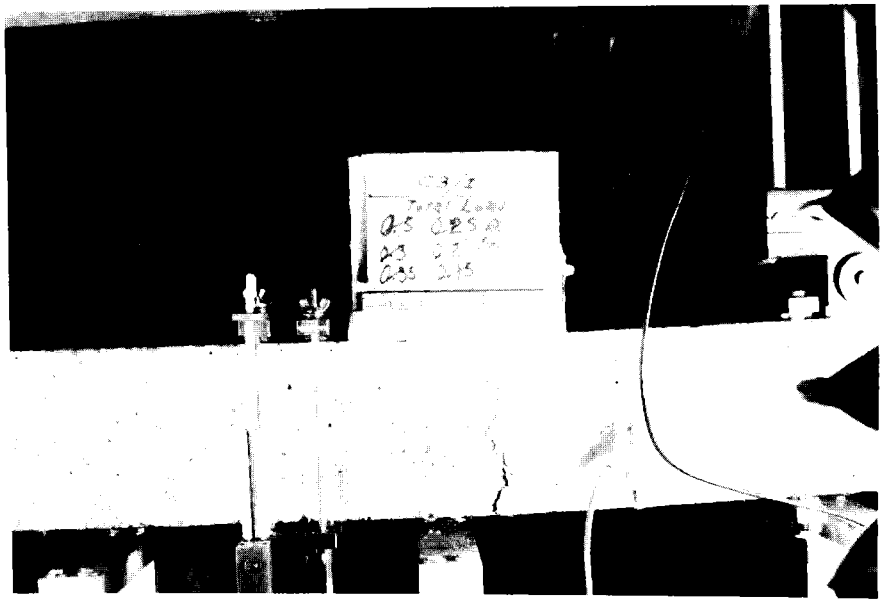

(b) Failed specimen

FIGURE 4.2 PHOTOGRAPHS OF BEAM TESTS

maintained constant at 0.03 in./min (0.76 mm/min) or less. The 0.03 in./min (0.76 mm/min) speed was found to be too fast to obtain the descending branch of the load deflection curve accurately, but one-half this speed was satisfactory. The reactions and load beam were made of very stiff and massive members in an effort to make the loading system rigid relative to the test specimen. The slow head movement of the machine, combined with the stiff load system, reduced the deformation at peak load due to energy release in the loading mechanism so that the descending branch of the load-deflection curve could be obtained. Load was measured with a load cell placed between the machine head and the load spread beam on top of the specimen. The weight of the load spread beam was not measured with this system, but the weight of the beam as well as the self weight of the test specimen were considered in the computations.

Deflections were measured with three LVDT's shown in Fig. 4.1. Measurements from LVDT Nos. 1 and 2 were used in the calculations; they provide deflection of the center of the beam relative to points 18 in. (457 mm) on each side of the center line where the yoke shown in Fig. 4.1 bears against the bottom of the beam. Thus, these instruments provide the deflection of the center of the beam relative to the yoke bearing points. Gage No. 1 had a high resolution and provided an accurate measurement up to slightly past the peak of the load-deflection curve. Gage No. 2 had a greater range but less accuracy and provided the entire load-deflection curve. Gage No. 3 measured the deflection of the center of the test specimen relative to the loading frame and was used for comparing overall beam performance and for checking purposes. It was not used for

calculating the stress-strain curve, however, as it contained the deformation of the support arrangement.

Deformations resulting from each LVDT were recorded graphically as a function of the load with an X-Y recorder. The output of the load cell was connected to the Y axis and that of the corresponding LVDT to the X axis; a typical set of load-deflection curves from Gage Nos. 1 and 2 is shown in Fig. 4.3. All measurements were also recorded on magnetic tape from which they can be taken directly for computational purposes.

In order to detect the extent and progress of cracking during the test, an acoustic counter was attached to the beam. This instrument counts the acoustic emissions in each predetermined time interval, accumulates them, and as output provides the integral of emission counts as a function of time. This data was recorded automatically during the test and was used to aid in determining the load at which cracking occurred.

Some aspects of the beam-test results are summarized in Table 4.1. The stress of the proportional limit, and cracking stress as well, is f_p. A drop in stress occurs after the matrix cracks and the resulting stress resisted by the fibers after cracking is f_d. In the table if f_d is not given, the curve for stress-strain was not calculated. Only 3 tests were considered good for obtaining the stress-strain curves because the descending branch of the load-deflection curves of the others were unreliable. The beam specimens for liner specimen C3 were precracked during handling. Some of the others were tested at a head movement rate that was too fast. The liner specimen C3 behaved similar to specimen C6, and the same concrete mixes were used. Therefore, the stress-strain curve ob-

TABLE 4.1

SUMMARY OF TEST RESULTS

Specimen	Machine head movement, in./min	Standard control tests				Long beam tests						
		f'_c, psi	f_r, psi	f_{sp}, psi	E, ksi	f_p, psi	f^*_r, psi	f_d, psi	E, ksi	f_d/f_p	f_p/f_{sp}	P_{max}, kips
C3-1	0.15	2200	500	265	1520	--	302	--	1310	--	--	2.18
C3-2	"	"	"	"	"	189	278	--	1200	--	0.71	2.00
C3-3	"	"	"	"	"	--	324	--	1560	--	--	2.33
C6-1	0.15	2400	610	340	1720	335	695	--	1620	--	0.99	5.01
C6-2	"	"	"	"	"	328	555	220	1778	0.67	0.97	4.01
C4-1	0.03	6600	855	765	3000	522	661	--	3120	--	0.68	4.76
C4-2	"	"	"	"	"	591	774	--	3430	--	0.72	5.57
C4-3	0.015	"	"	"	"	661	874	458	3076	0.69	0.86	6.29
C5-1	0.015	7630	850	795	3100	667	830	--	3460	--	0.84	5.98
C5-2	"	"	"	"	"	682	880	418	3633	0.61	0.86	6.33
C5-3	"	"	"	"	"	620	712	--	3160	--	0.78	5.13

TABLE 4.1 (S.I.)

SUMMARY OF TEST RESULTS

Specimen	Machine head movement, cm/min	Standard control tests				Long beam tests						P_{max}, kN
		f'_c, kPa	f_r, kPa	f_{sp}, kPa	E, MPa	f_p, kPa	f^*_r, kPa	f_d, kPa	E, MPa	f_d/f_p	f_p/f_{sp}	
C3-1	0.0762	15150	3450	1800	10500	--	2080	--	9020	--	--	9.7
C3-2	"	"	"	"	"	1290	1920	--	8260	--	0.71	8.9
C3-2	"	"	"	"	"	--	2230	--	10720	--	--	10.4
C6-1	0.0762	16600	4170	2320	11700	2310	4790	--	11130	--	0.99	22.3
C6-2	"	"	"	"	"	2260	3820	1510	12220	0.67	0.97	17.8
C4-1	0.0381	45500	5850	5230	20500	3590	4550	--	21500	--	0.68	21.2
C4-2	"	"	"	"	"	4070	5330	--	23600	--	0.72	24.3
C4-3	0.0762	"	"	"	"	4550	6010	3160	21150	0.69	0.86	28.0
C5-1	0.0762	52200	5850	5440	21200	4590	5710	--	23800	--	0.84	26.6
C5-2	"	"	"	"	"	4690	6060	2880	25000	0.61	0.86	28.2
C5-3	"	"	"	"	"	4270	4900	--	21750	--	0.78	22.8

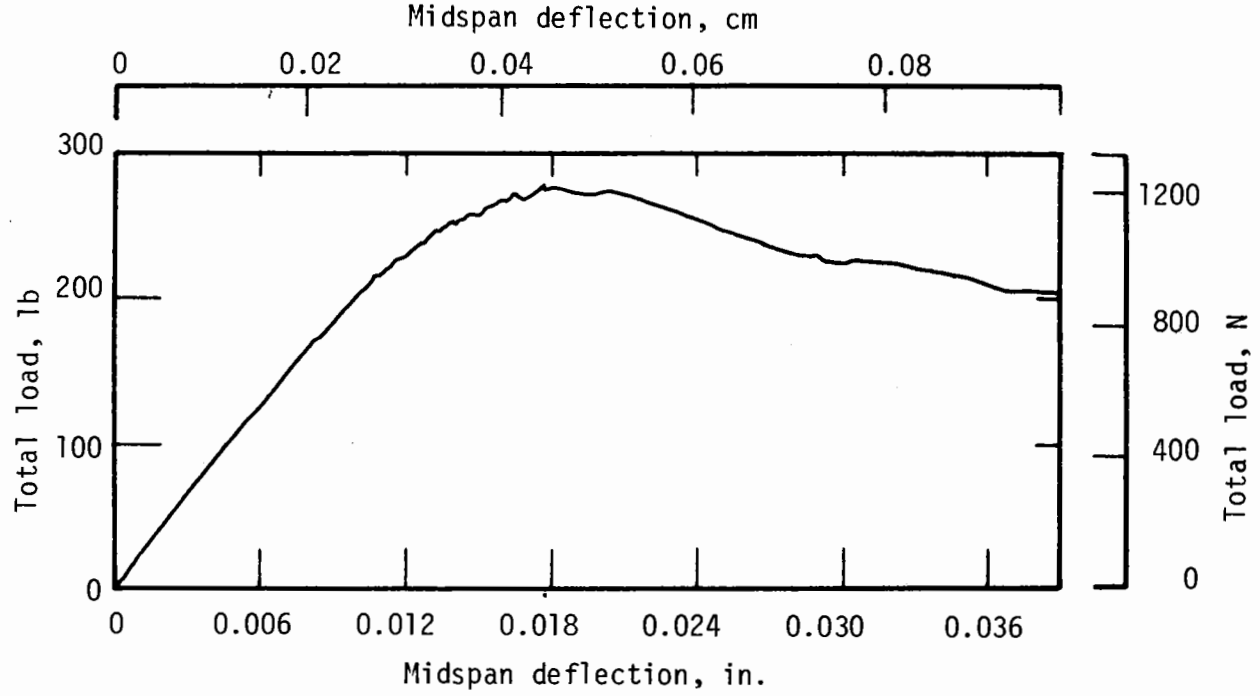

(a) Short range LVDT

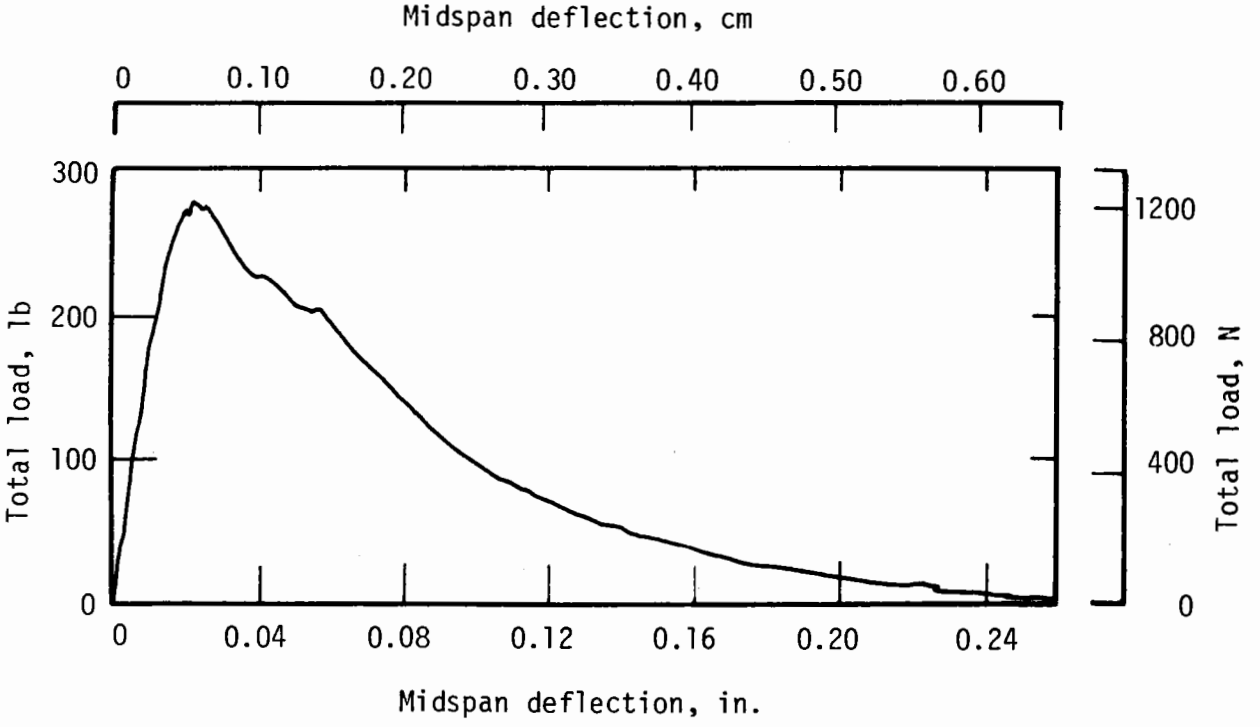

(b) Long range LVDT

FIGURE 4.3 TYPICAL LOAD-DEFLECTION CURVES FROM BEAM TEST

obtained for specimen C6 was also used for C3. Beam loads from specimens C4 and C5 were comparable, indicating similar tensile strengths.

COMPUTATION OF FLEXURAL STRESS-STRAIN CURVES

The basic method for computing the stress-strain curve is not greatly different from that used by Hognestad, Hanson, and McHenry (1955) for the compression stress-strain curve, though the tests to obtain the basic information are quite different. The approach is to test beams with a constant-moment region and determine the deflected shape within this region at 3 points. When a crack forms within the region, the moment remains constant, but the beam is divided into cracked and uncracked portions for computational purposes. The crack influences the beam adjacent to it for some distance, so the cracked portion is replaced in the computations by a homogeneous element with different properties. The length of this element in these studies was taken equal to the depth of the beam. The uncracked region is assumed to have the same properties as before the crack and the average properties of the "crack element" can be determined from the load-deflection behavior of the beam after cracking. If the computational procedure is reversed, using the calculated stress-strain curve, the load-deflection behavior of the test beam will be reproduced analytically. It is necessary to determine the moment-curvature relation for the crack element from the load-deflection curve. This requires an accurate measurement of deflection and of the location of the crack.

When a crack began to propagate from the tension side of the beam toward the neutral axis, the load-deflection curve changed slope. The

sudden drop in stress with cracking of the matrix is related to the slope change analytically, and a procedure is described for accurate determination of the drop by Herring and Kesler (1974). The peak stress just before the drop, was obtained from a straightforward computation based on a linear stress distribution and the moment at the proportional limit of the load-deflection curve.

After cracking, points on the stress-strain curves were found successively by using all the previously obtained points and determining the new stress value at the bottom fiber of the beam so that equilibrium and compatibility are satisfied on the section in terms of the moment and curvature obtained from the load-deflection curve. This is an iterative procedure and the Newton-Raphson procedure is used to speed up convergence. In addition, the calculation of stress is very sensitive, so special precautions must be taken in the computation to avoid wild fluctuations of the stress that build up as the computations proceed. It is not surprising that the computation is sensitive, because the reversed calculation of the moment-curvature curve is rather insensitive to the stress-strain curve used.

The stress-strain curve obtained in this section was used to calculate moment-curvature relations that allow determination of the moment-thrust failure envelope for the liner specimen. Each section in a liner has both thrust and moment, while the stress-strain curves were obtained for pure moment. Studies are planned to determine whether the thrust influences the stress-strain relationship by using the curves obtained from

beams to predict the behavior of beam-column specimens that have been tested. However, in this report it was assumed that there is no effect.

The stress-strain curves calculated in this way for the concrete specimens C4, C5 and C6 are shown in Fig. 4.4. The curves have a linear portion up to the initial peak, drop suddenly to a lower value when the concrete matrix cracks, and descend irregularly as the steel fibers resist stress across the crack. The stronger concrete specimens (C4 and C5) are similar and in all three curves the stress drops to 66 to 69 percent of the initial peak value. After cracking the weak concrete appeared to maintain a constant stress for a larger strain. The initial peak stress at cracking is not changed a great deal by the presence of the fibers. The post-crack stress is substantial and maintained over a large strain, so will influence the behavior of a structure.

4.2 COMPUTATION OF FAILURE ENVELOPE

The response of a reinforced concrete cross section to external loads can be computed from the application of ordinary principles of mechanics of materials. Because of the nonlinear stress-strain relations it is more convenient to reverse the process and define the relationship of moment, thrust and curvature by a number of discrete points obtained from assumed stress and strain on the section (Pfrang, Siess and Sozen, 1964). This approach has been used to define the behavior of steel-fiber-reinforced concrete cross sections.

A computer program was written that computed the moment-curvature curve for a specified axial load on the section. For an assumed linear

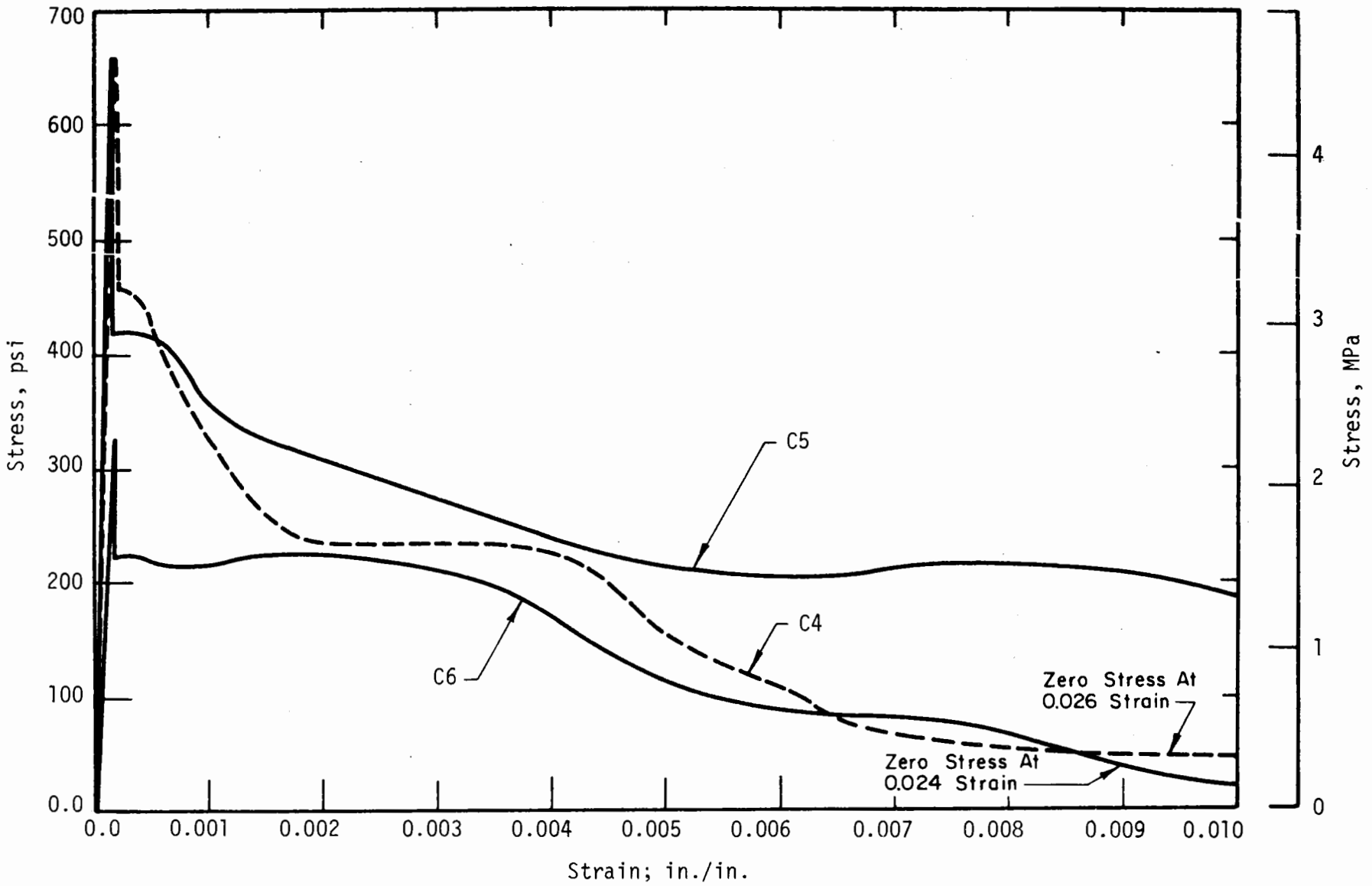

FIGURE 4.4 CALCULATED FLEXURAL TENSION STRESS-STRAIN CURVES FOR THE LINER SPECIMENS

strain distribution, the stress distribution is known from the stress-strain curve and the curvature is defined. The thrust and moment can be calculated. Maintaining that curvature (slope of the strain distribution) the neutral axis can be moved iteratively until the specified thrust is obtained. One desired moment-thrust-curvature point is then known. The curvature is changed and the process repeated until the specified thrust is again obtained. Once the moment-curvature relation throughout the desired range is found, the thrust is changed and the process repeated. The program allows any shape of stress-strain curve to be defined with a series of points and assumes the curve linear between them. Descending branches of the stress-strain curve and cut-off of the curve can be handled.

An example of a set of moment-curvature-thrust curves for a steel-fiber-reinforced cross section with the stress-strain curves of specimen C4 is shown in Fig. 4.5. These curves have shapes similar to those of conventionally reinforced concrete members (Pfrang, Siess, Sozen, 1964). The moment capacity increases with increasing thrust up to a point and then decreases.

The moment-thrust failure envelope can be derived from these curves if failure is defined as decrease in moment, because then the peak of each curve defines a point on the envelope. The failure envelope determined in this way for the concrete of specimen C4 is shown in Fig. 4.6 and has the typical shape of the curve for conventionally reinforced members. The moment at zero thrust was determined from the pure moment calculation, the zero moment point represents pure thrust, and the balance point is that of largest moment given by the highest curve in Fig. 4.5.

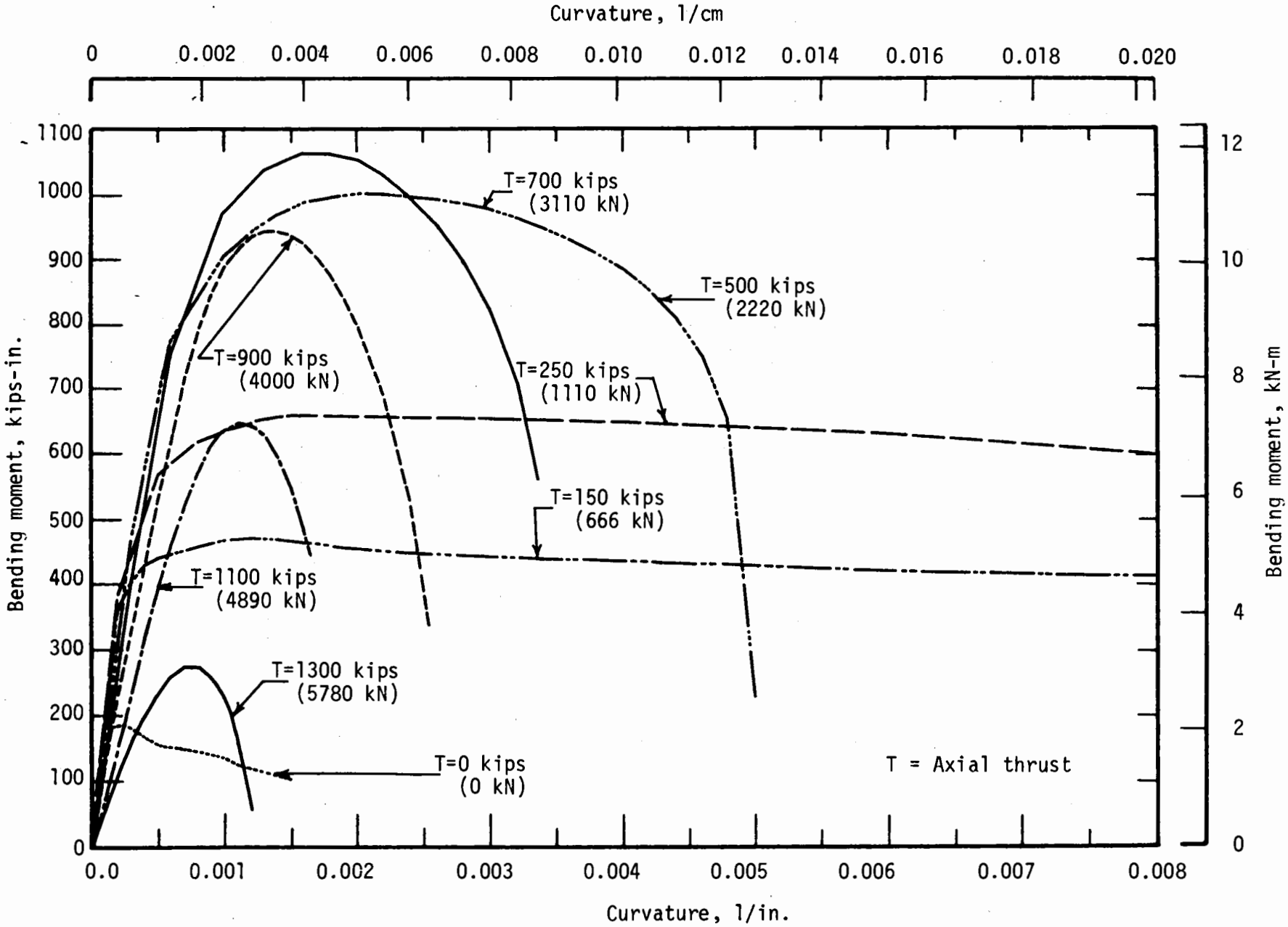

FIGURE 4.5 CALCULATED MOMENT-CURVATURE CURVES FOR LINER SPECIMEN C4

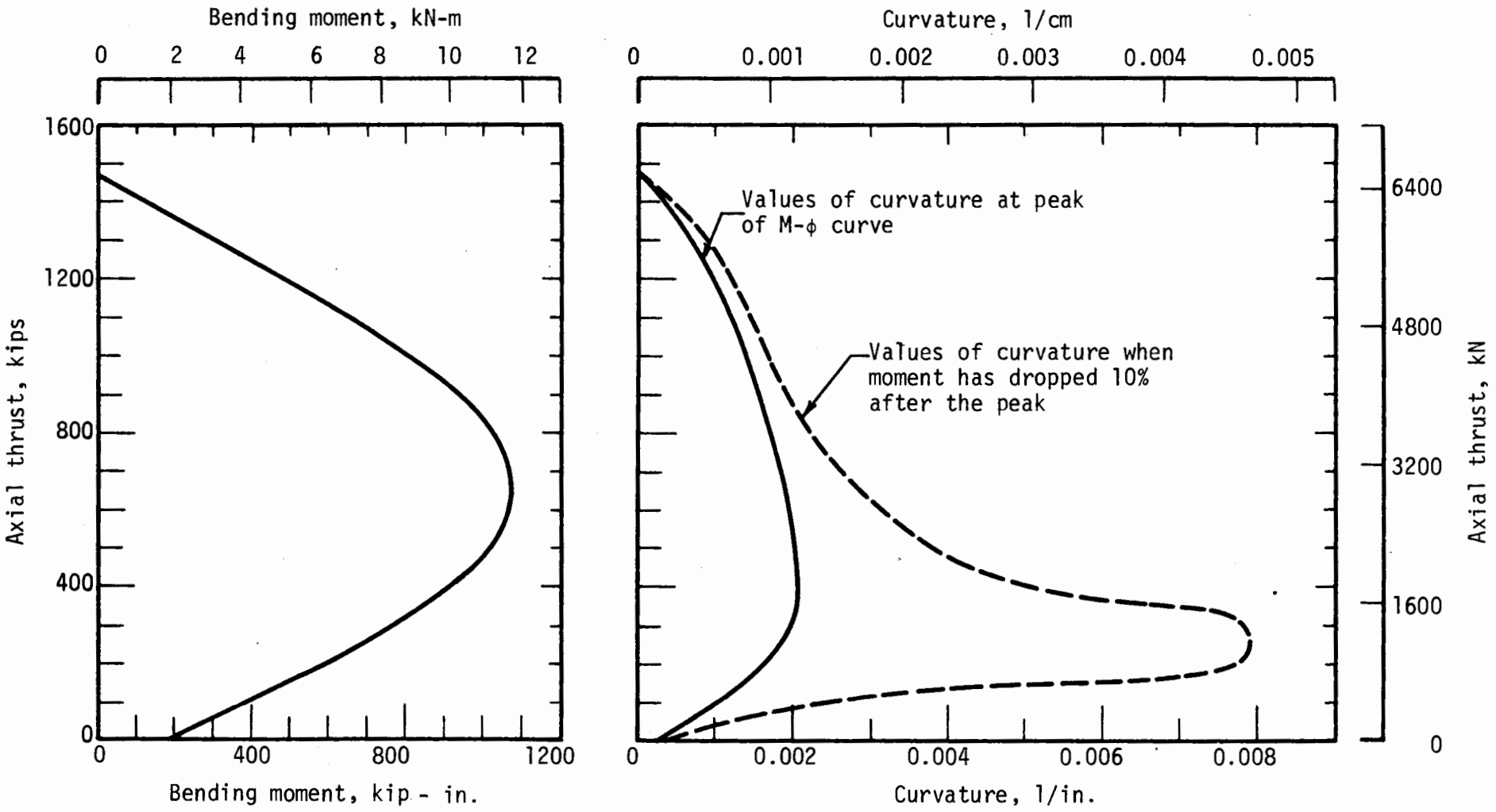

FIGURE 4.6 THRUST-MOMENT FAILURE ENVELOPE AND THRUST-CURVATURE CURVES, TYPICAL FOR HIGH STRENGTH SPECIMENS

The thrust-curvature curve of Fig. 4.6 helps to visualize the section behavior in terms of ductility. The inner curve is the curvature at which moment was maximum and the outer one is the curvature when the moment had dropped 10 percent after the peak. Thus, the separation of the curves is a measure of the flatness of the moment-curvature curves. These thrust-curvature curves are similar to those obtained for conventionally reinforced concrete members when the curvature at the yield point and maximum moment points are plotted and provide a similar visualization. One difference between the outer curve and the one obtained for conventionally reinforced members is the low ductility at low thrust. For conventional members curvature continues to increase as thrust decreases for the outer curve.

The relatively flat portion of the moment curvature curve has an important influence on the structural behavior because it allows the thrust at a section to increase (jump from one curve to another), the curvature to increase (move to the right in Fig. 4.5), and the moment to increase also.

The moment-thrust failure envelopes are shown in Fig. 4.7 for the concrete in the liner specimens tested. The stress-strain curves described in Section 4.1.2 for flexural tension were used. The shapes of the compression stress-strain curves described in Section 4.1.1 were used, but the magnitude of stress was increased proportionally so that the peak stress agreed with the average values obtained from the control cylinder tests. The envelopes are also shown in the moment-thrust curves of Section 3.3.2 that show the test results (Figs. 4.29-4.32). These envelopes

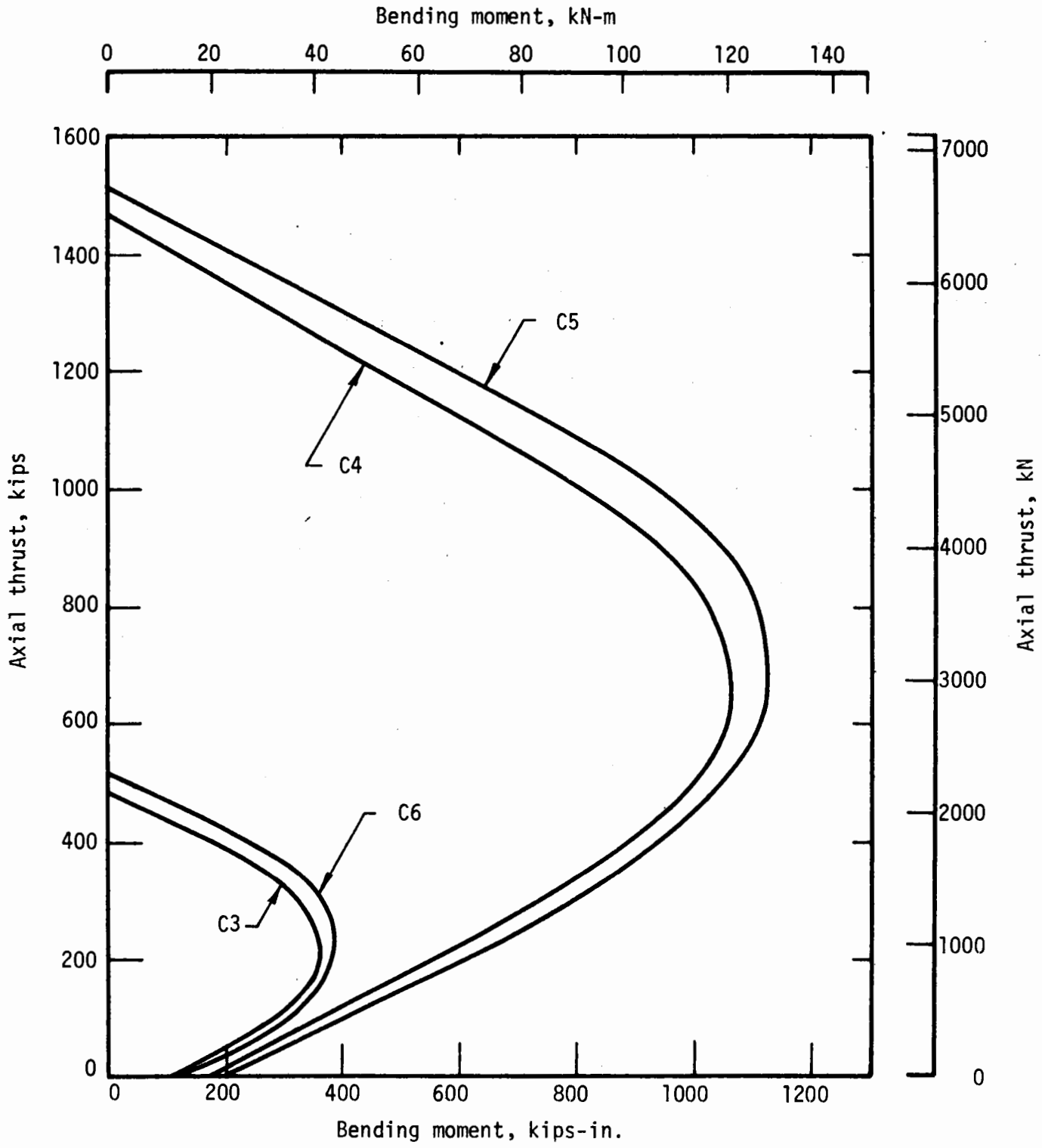

FIGURE 4.7 THRUST-MOMENT FAILURE ENVELOPES FOR THE LINER TEST SPECIMENS

may not be entirely representative of the sections in the liner because the stress-strain curves for the concrete in the liner may be different. This difference can result from different fiber distribution, concrete curing conditions, normal variation in behavior of cylinders vs structures, loading rate, etc.

CHAPTER 5

DISCUSSION AND RECOMMENDATIONS

5.1 TEST RESULTS

The purpose of the liner tests was to study the behavior and failure mechanism of the specimens in order to develop an analysis and failure criterion for this type of structure. One specimen tested under given conditions may not be representative of this specimen and loading condition because of the variability of concrete and uncertainty of loading. For this reason two nearly identical tests were performed for each concrete strength. The low-strength concrete tests C3 and C6 and the high-strength concrete tests C4 and C5 were each intended to be as similar as possible.

The two low strength concrete specimens behaved similarly with tension cracking detected first on the inside, near north and south, at P = 19 to 22 kips (84 to 97 kN). Most of the additional distress occurred in the south half of the specimens. Additional sections of distress were observed near the midpoints between loads, at the maximum negative moment regions, causing crushing on the inside and tension cracks on the outside, but these developed at high loads from P = 73.4 kips (327 kN) and higher. Though the tension cracks at north and south were detected at relatively low loads, crushing outside at north and south occurred at 117.1 kips (521 kN) and higher.

Failure occurred at different locations in the two specimens, but

the appearance of the two failure regions was similar. The failure plane in C3 occurred between 168 and 176 deg, and the initial distress was a tension crack on the inside, where the moment was positive, at the 176 deg section. The failure surface extended through the section at about 25 deg from the liner axis and flattened a little near the outside (Fig. 3.3b). The failure plane occurred in specimen C6 between 228 and 236 deg, and the initial distress was a tension crack outside, where the moment was positive at the 228 deg section. The failure surface generally made about the same angle with the liner axis as for specimen C3 (Fig. 3.6b), and it also flattened near the outer liner surface. In each specimens there was great distress, consisting of compression crushing on one side and tension cracking opposite to it, at the location where the other specimen failed. Thus the section that did not fail completely was near failure in each case and provides an indication of the conditions just prior to failure.

Moment in general is negative or near zero between loads and positive at the load points, so the moment gradients are steep. The failures can extend across regions in which the moment changes sign, so it is difficult to determine the cause of failure. Shear also acts on the section and may influence formation of the failure surface.

Tensile cracking was detected on the inside near north and south in tests C4 and C5 at about one-half the load (9.4 to 11.7 kips (41.8 to 52.0 kN)) that it was detected in tests C3 and C6 as shown in Figs. 3.7 and 3.10. The reason is the smaller passive stiffness for tests C4 and C5 that allowed larger deformation. Crushing was detected opposite these cracks at a load (74.4 kips (331.0 kN) for specimen C4) much higher than

the cracking loads. In both specimens tension cracks on the outside occurred midway between the east load point and both adjacent loads at a load of 19.4 to 27.7 kips (86.2 to 123.0 kN), and some crushing occurred opposite these cracks later in the test. Tension cracks occurred in tests C3 and C6 at about those same locations but at much higher load.

Failure occurred in the same locations in tests C4 and C5 just north of the west load point and the formation and appearance of the failure surfaces were similar. Tension cracks opened on the outside (negative moment) at 23.5 to 27.7 kips (104.4 to 123.1 kN) load, and crushing was detected on the inside about 4 in. (10.1 cm) north of these cracks at 78.3 to 94 kips (348.0 to 418.0 kN) load. The tension cracks traveled into the section, perpendicular to the surface, and then bent toward north; at a load of 103.8 to 124.9 kips (461.0 to 555.0 kN) crushing on the inside became so extensive that the tension cracks closed and compression was transferred to the outer edge of the liner because the inner edge could no longer resist compression. At failure, the compression zone, now on the outside, sheared a wedge of concrete off the outer surface that allowed the parts of the liner on each side of the crack to slip past one another. This closing of the tension crack and breaking off a wedge of concrete on the outside surface did not occur in the failure of specimens C3 and C6 because the tension cracks did not open nearly as much in these low-strength concrete tests.

The difference in failure mechanism between the specimen of different strength appeared to be dependent on the stiffness of the passive forces. High stiffness leads to small cracks opening throughout the test and

a rather sudden failure along an inclined sliding plane late in the test. Low stiffness lead to a larger crack opening from the beginning of the test that caused larger compression distress in the form of crushing, and then crack closing before final failure.

Deformation of the liner depends primarily on the passive mechanism stiffness, and deformation influences the failure. The load-diameter change curves show that the north-south diameter change at failure for the high-strength concrete specimens (Figs. 3.19 and 3.20) was about twice that for the low-strength concrete specimens (Figs. 3.17 and 3.18). This is shown in Table 3.1 where the diameter change at failure divided by the diameter is tabulated. The maximum loads are not greatly different, so the passive stiffness must account for this difference in deformation at failure. The east-west diameter changes for the higher strength concrete specimens is about 3 times that for the low-strength ones while the difference was a factor of 2 for the north-south diameter change as mentioned above. That is, the difference between the north-south and east-west diameter changes is larger for the low-strength concrete specimens because the axial shortening is larger due to a lower Young's modulus for the material. The ratio of north-south to east-west diameter change was 1.90 and 1.85 for specimens C3 and C6, while it was 1.34 and 1.42 for C4 and C5. The influence of this on the failure mechanism is shown by the difference between the mechanisms in the high- and low-strength concrete specimens. The larger deformation in the high-strength specimens reduced the compression area on the inside in the failure region.

Thrust at failure was on the order of 250 kips (1110 kN) for all specimens. For the low-strength concrete liners the compressive strength (f'_c) of the concrete would be developed if 3 in. (76 mm) or about one-half the section depth resists compression uniformly. The corresponding depth to develop the high-strength concrete capacity is about 1 in. (2.54 cm). The greater deformation allowed by the less stiff passive forces reduced the compression area and explains the low ultimate load of the high-strength concrete specimens.

In all the tests the east-west diameter change curves were almost linear because they were influenced heavily by the passive forces while the north-south deflection increased more rapidly than linearly. In all tests a short plateau was reached at peak load, though in test C6 this is not well defined because failure occurred before the next set of deformation measurements could be taken, but the last load was recorded to be essentially the same as the previous one.

The passive load distribution around the specimens is shown by the passive-active force ratio curves of Figs. 3.25 to 3.28. Clearly there was a change in the distribution of load as cracking progresses. At low load, when the specimen was intact, the passive loads were much lower than later after cracking was fully developed. The curves are somewhat erratic during the initial cracking phase and depend on the location and sequence of crack formation. After this phase the relationship was nearly linear up to the failure range, and again became erratic in the last load increment. There was considerable difference between the load distribution in

the high- and low-strength concrete specimens at low load, but they became nearly the same near the failure load.

The internal moment and thrust at sections of distress help to understand how the liner redistributes moments due to cracking and nonlinear structural behavior and will help develop failure criteria.

In the moment-thrust curves of Figs. 3.29 to 3.32 there are basically two types of curves, those that curve gradually upward and inward, and those that remain almost linear to failure of the specimen or remain linear for a time and turn inward sharply near filure. In all tests there were some sections that turned inward, corresponding to a decrease in moment as thrust continued to increase. When moment decreased at these sections, it increased at others and the mechanism of resistance changed.

Predicted moment-thrust failure envelopes for the liner section of each specimen are shown on the moment-thrust graphs and were calculated as described in Chapter 4. Paths for the liner test specimen sections generally remain within the envelopes and in many cases parallel it. It is possible for the moment-thrust path for a ductile section to remain on the failure envelope for some load range and then to leave it traveling inward. This probably occurred for these sections, but the real failure envelope for the section is not the one shown. If the concrete properties at a section of the liner varies because of different fiber distribution or orientation, concrete segregation, etc.,then the failure envelope will change for that section. Undoubtedly the failure envelope changes around the liner.

A parameter study was performed to determine how the moment-thrust

failure envelope changed as the tension and compression stress-strain curves vary. The stress-strain curves that were typical of a low strength concrete were used as the base, and the tension curve was kept the same while the compression stresses were changed to ±15 percent of the original curves. A second set of problems was run in which the compression stress-strain curve was maintained while the tension stresses were varied ±30 percent. Also the case of no tensile stress was considered. The stress-strain curves are shown in Fig. 5.1 and the moment-thrust failure envelopes in Fig. 5.2. The procedure used to obtain the envelopes is described in Chapter 4.

It is clear from Fig. 5.2 that the compression stress-strain curve influences the failure envelope more than the tension curves. Also, the compression stress-strain curve shows a large influence in the compression failure region, i.e., that part of the failure envelope above the balance point (point of maximum moment), but the influence extends well into the tension failure region also. The tension stress-strain curves influence the part below the balance point of the envelope most, but its influence extends into the compression failure region above the balance point as well.

The effect the stress-strain curves would have on the structural behavior of the liner depends on the moment-thrust paths of critical sections in the liner. If the passive lateral resistance in the ground is high, such as in a rock tunnel, moment would be low and the path would be steep, going toward the compression failure region. In that case the tension stress-strain curve would have little influence on structural response or failure. Also, in that case failure would occur when the envelope was

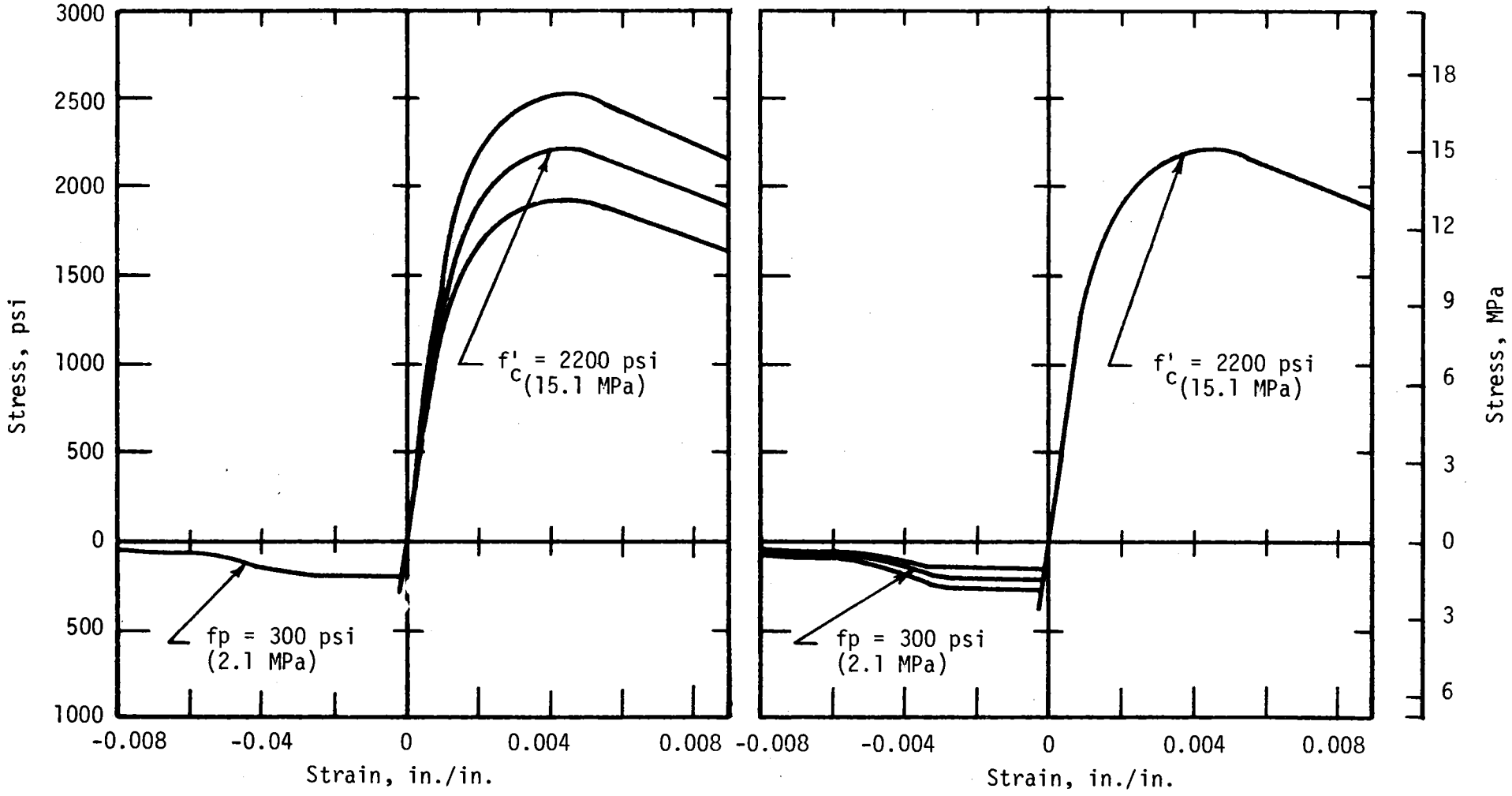

FIGURE 5.1 STRESS-STRAIN CURVES USED IN MOMENT-THRUST FAILURE ENVELOPE STUDY

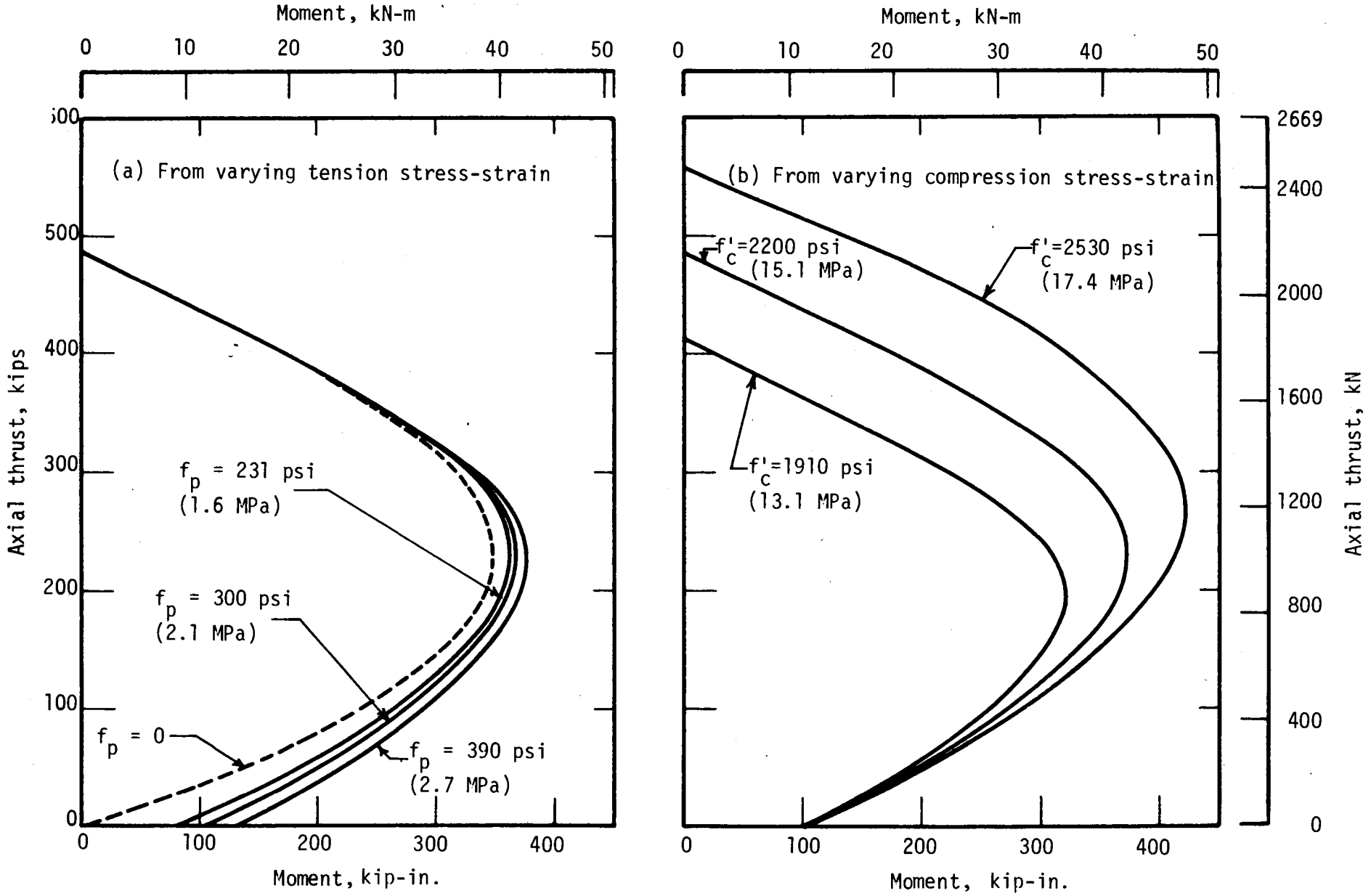

FIGURE 5.2 COMPARISON OF MOMENT-THRUST FAILURE ENVELOPES RESULTING FROM VARYING STRESS-STRAIN CURVES

reached. If the passive resistance in the ground were low, the tension failure region of the envelope would be reached first, but if the moment-thrust path followed the envelopes, then failure would not occur immediately. Maximum load would be reached after the path was forced to leave the envelope, and this depends on the section ductility. The envelope drawn for a section without tension stress shows that tension stress in the material is not required to have considerable capacity when there is substantial thrust present.

This study shows that the moment-thrust failure envelope can vary a great deal with reasonable variation of material properties, so those obtained from tests other than the liner test itself, provide only a guide for the shape and approximate magnitude. Nevertheless, the calculated envelope appears to represent the actual one for some sections and to represent the shape rather well for others.

Loads on the liners at failure are summarized in Table 3.1 and show about the same ultimate loads. The average of the loads for the low strength concrete specimens is higher than for the high strength specimens. This shows the large influence of the passive stiffness, because the lower passive stiffness offset the much greater strength of the high-strength concrete. The low-strength specimens developed a thrust that was about equal to that at the balance point on the moment-thrust failure envelopes, while the thrust in the others was only about 30 percent of that at balanced conditions (Fig. 4.7).

5.2 ANALYSIS

Structural tests of tunnel liners of the type described in this report have two shortcomings. They cannot simulate exactly the behavior of a liner in the ground, and it would be too costly to perform a sufficiently large number of tests to cover the complete range of all important variables. An analysis that will adequately predict the structural response of the liner can help to overcome these shortcomings. The adequacy of the analysis can be shown by comparison with a limited number of tests. Once this is done, more realistic active loading distributions and passive resisting systems can be studied, Also large numbers of solutions can be obtained in which changes of parameters are studied. In this section, an analysis is described based on NASTRAN, the general purpose structural analysis program developed by NASA, and then the analysis results are compared with the test.

5.2.1 DESCRIPTION OF MODEL

To model a structural member with NASTRAN that will resist thrust, shear and moment so that the nonlinear material properties of steel-fiber-reinforced concrete are represented in a reasonable way, it is necessary to build a beam element with rods and shear panels. The beam elements are then put together to form the tunnel liner. A model of this type is described in a previous report (Paul, et al., 1974); the model described in this section contains a larger number of rods and shear panels in a beam

The stress-strain curve for each rod may be assigned by defining points on the curve. A linear relationship is assumed between points. The stress-strain curve can be different in tension and compression, but the curve cannot have a descending branch or stress cut-off.

With this model of one quarter of the specimen the boundary conditions were selected on the assumption of symmetry about the north-south and east-west axes. Nodes at the north section were restrained to move only in the north-south direction and nodes at the east only in the east-west direction. The effect of nonsymmetry of loads about these axes cannot be studied with this model, though it can be with a similar model of the entire liner.

Studies were performed previously with a model constructed in the same way except that the beam element contained 7 longitudinal rods and the liner consisted of 2 beam elements in each 30 deg segment between forces. Results of a liner analysis with the old model are compared with results from the new model in Fig. 5.4 in terms of the moment-thrust path for critical sections. The same stress-strain curves are used for the longitudinal rods. The new model will represent the actual structural response of the liner more accurately than the old one. The two moment-thrust paths are so close that it would appear that further refinement of the model with a larger number of elements is not justified for better definition of overall behavior. However, it may be desirable to use a larger number of elements to represent the liner to obtain a better representation of the variation of internal forces.

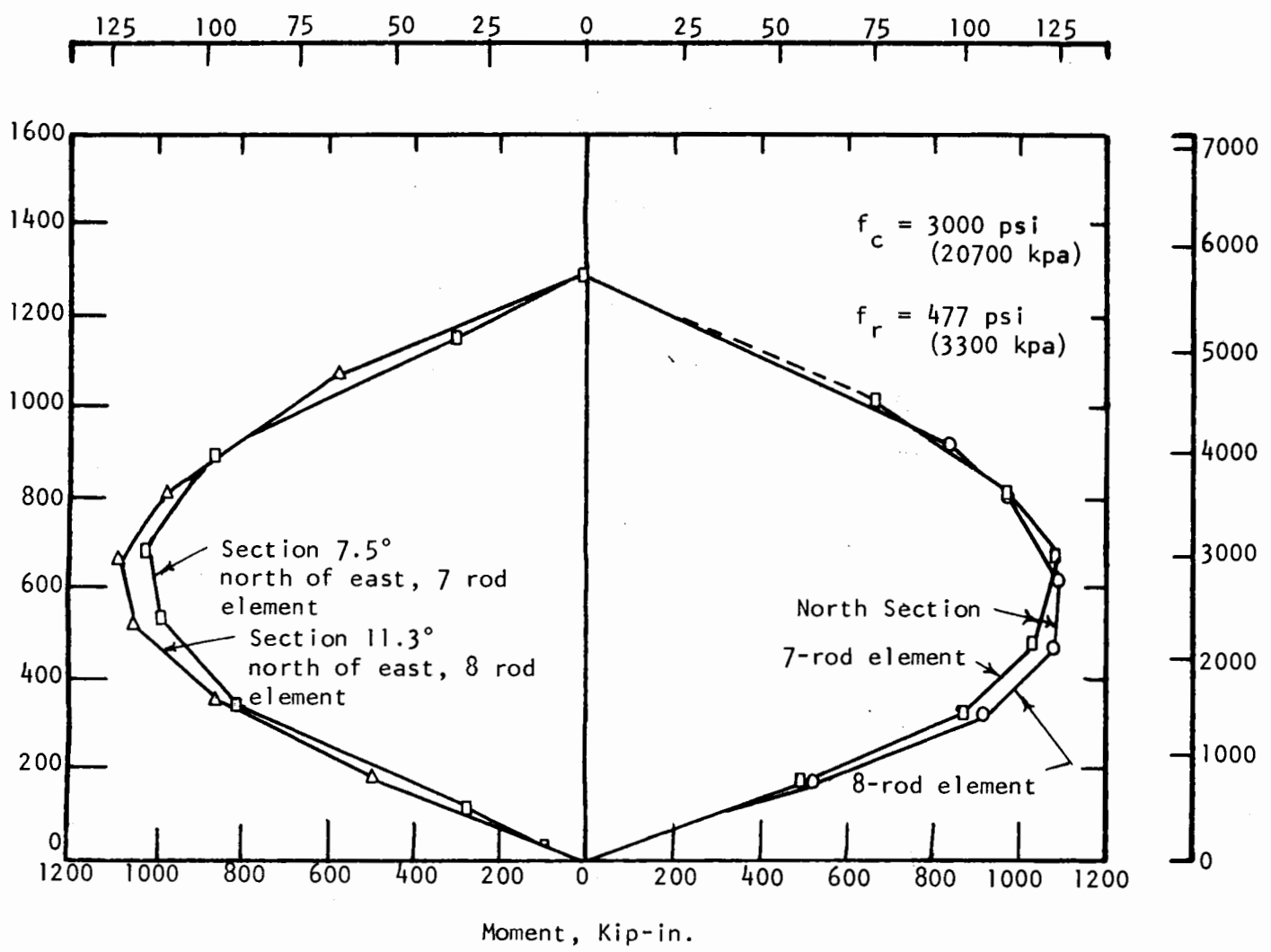

FIGURE 5.4 COMPARISON OF MOMENT-THRUST FOR 7 ROD AND 8 ROD ELEMENTS

5.2.2 COMPARISON WITH TEST RESULTS

The compression stress-strain curve obtained from testing standard cylinders from the concrete representative of the low-strength specimens was approximated up to the peak stress for representation in the analysis as shown in Fig. 5.5. Beyond the peak, the stress must remain constant in the analysis. A maximum stress of about 80 percent of the modulus of rupture was assumed for the maximum tension stress with a constant stress beyond the peak. The initial modulus of elasticity was taken to be the same in tension and compression.

The load-deformation curves for test C3 and the analysis are compared in Fig. 5.5 where the deformation is measured by the north-south diameter change; load is the active load P that occurs at each active load point. Initial slopes of the curves are the same, but the analysis shows smaller deflection above 30 kips (130 kN) of load. Also the analysis shows a maximum load much larger than the maximum test load. This occurs because the analysis does not allow the representation of a descending stress-strain curve, so the thrust continues to increase until a fully plastic stress is obtained and the moment resistance becomes zero. In reality, failure must occur at a lower load because of the descending stresses in the stress-strain curves. The computed moment-thrust path of the north section is compared with the computed moment-thrust failure envelope in Fig. 5.6.

The computational element and stress-strain curves described above were used to obtain this failure envelope. Load increment 5 of the analysis agrees closely with the load at failure of the test specimen.

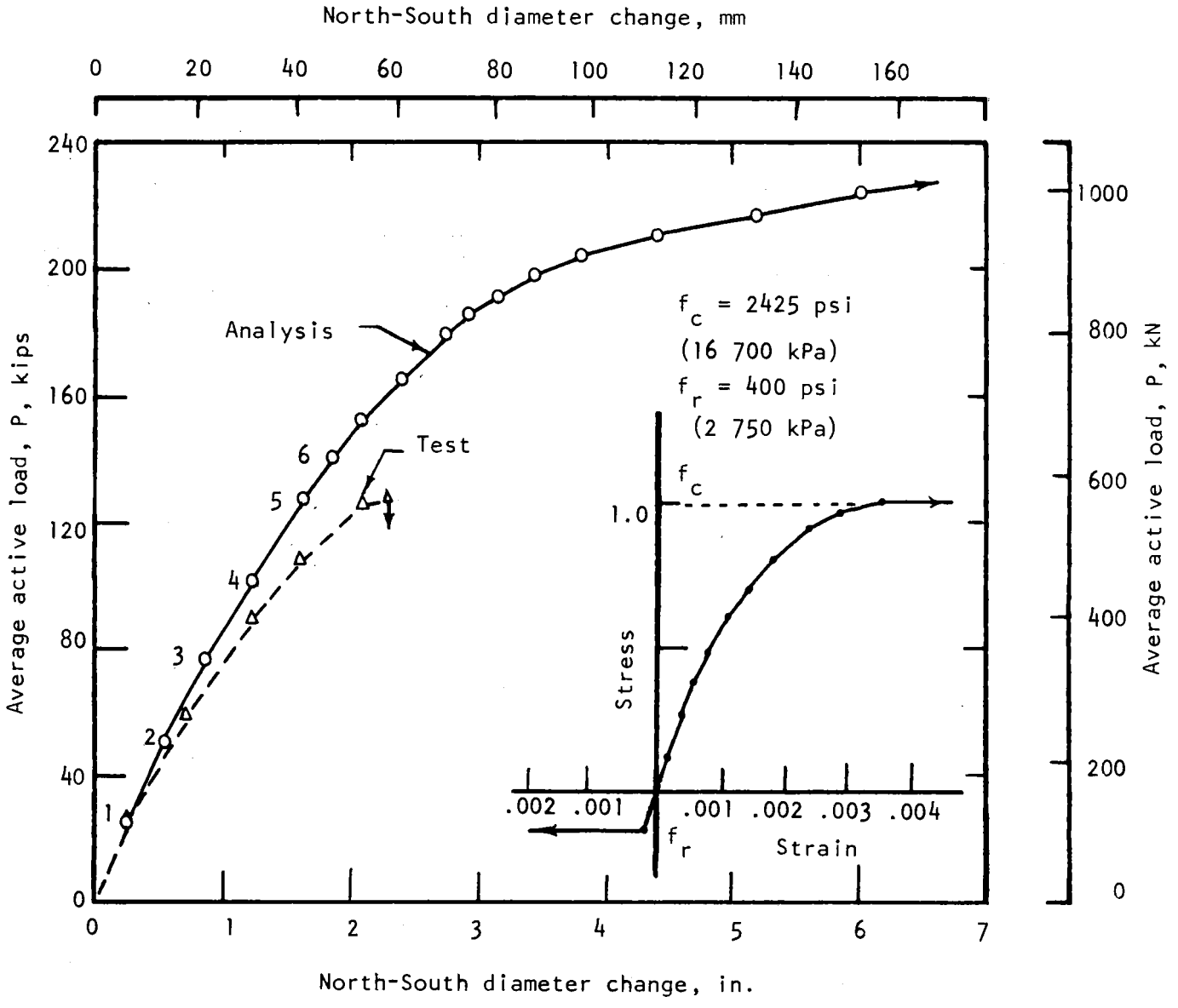

FIGURE 5.5 COMPARISON OF LOAD-DEFORMATION FROM ANALYSIS AND TEST

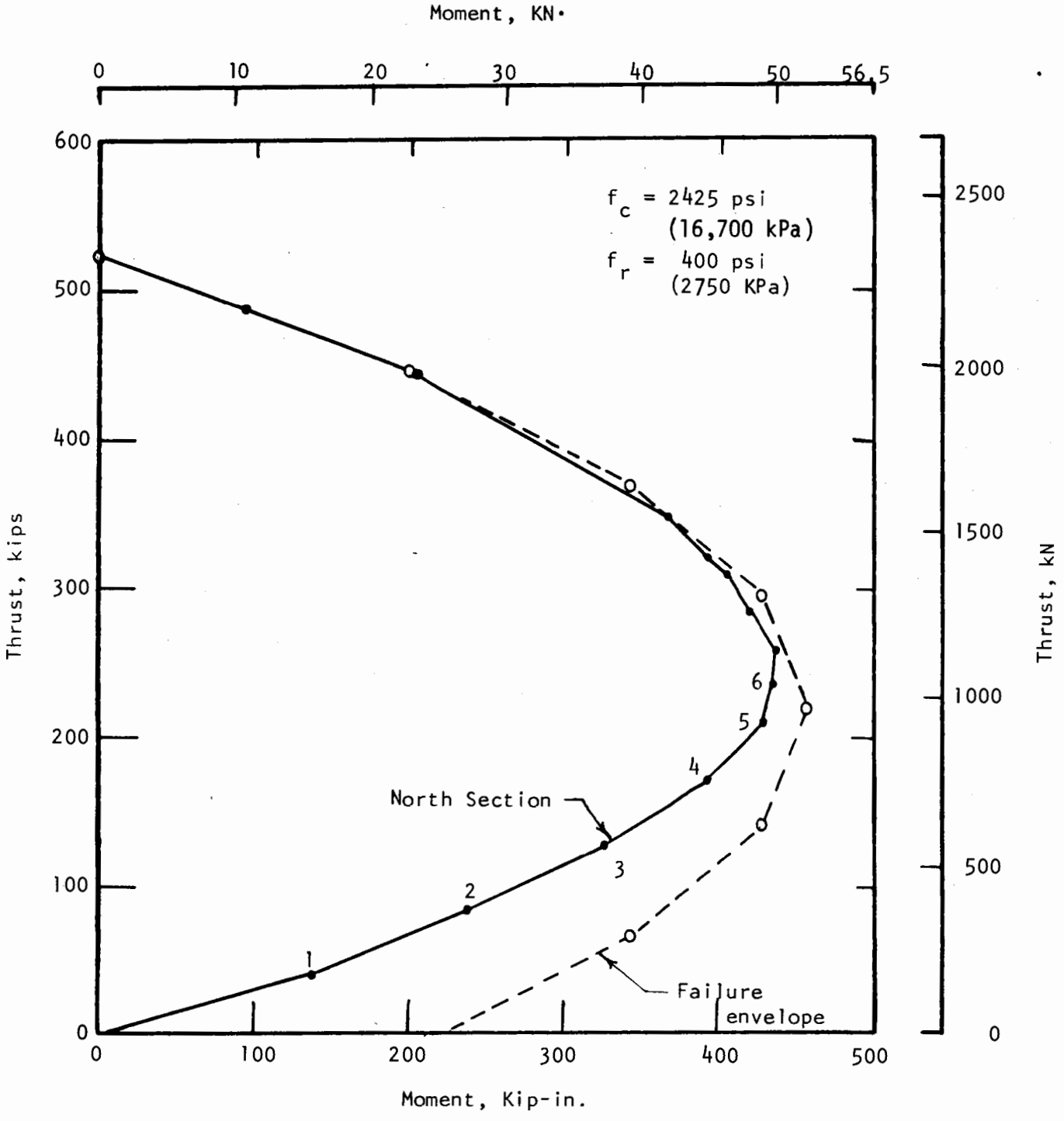

FIGURE 5.6 MOMENT-THRUST PATH AND FAILURE ENVELOPE FROM THE ANALYSIS

At load increment 5 (Fig. 5.5 and 5.6) the analysis shows an active load on the specimen of 128 kips (570 kN) while the failure load in the test was 129 kips (574 kN) (Table 3.1).

An approximate procedure to predict failure of a section of the real liner that is cracked, by comparing calculated stresses at a point, for a psuedo homogeneous region of the liner, with the material strength properties may be feasible. The stress distribution in the liner can be predicted, at least approximately, with the analysis described in Section 5.2.1. In Fig. 5.7 the longitudinal stress in the bars is shown through the depth of the section of the three elements east of north in the analysis model. The analysis assumes symmetry so this segment is the same as the segment between 150 and 180 deg where the failure occurred in test C3. The stresses are shown for the section at the center of the element so the first one labeled (1) is 5 deg clockwise from north. This section is very close to the edge of the load spread beam where the shear is largest. At the bottom of Fig. 5.7 are shown the principal stresses calculated from the bending stress for section (1) and the shear stresses at the edge of the load spread beam. The shear panel does not have a shear stress distribution as the shear is resisted by forces concentrated at its corners. Therefore, a parabolic shear stress distribution given by the conventional formula for shear stress in beams was used.

As shown in Fig. 5.7(c), the maximum compression stress had reached 2425 psi (16700 kPa) for this particular computer analysis (Fig. 5.6) so crushing of the concrete in this region is indicated because f'_c

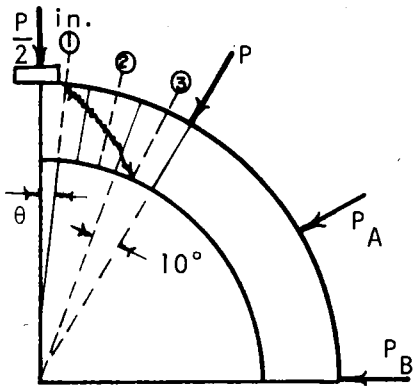

Note: Failure occurred near the south section, but it is shown at the corresponding location at the north in the analysis model.

C = compression
T = tension

(a) Beam elements in the failure region

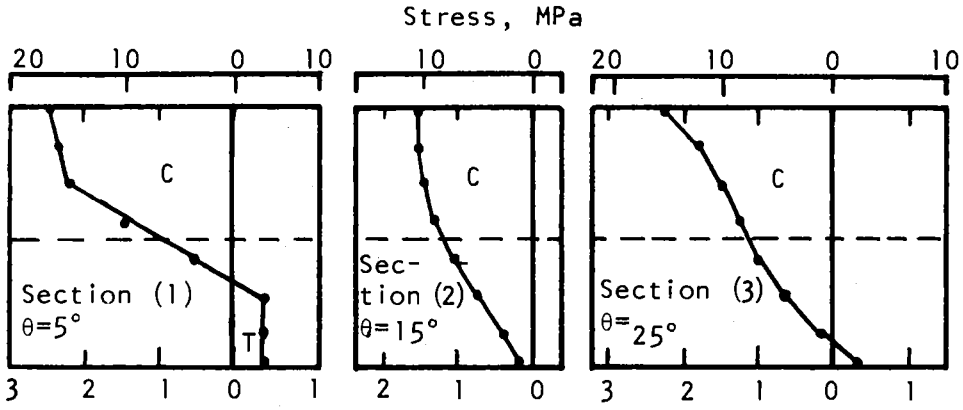

(b) Stress distribution in the longitudinal rods

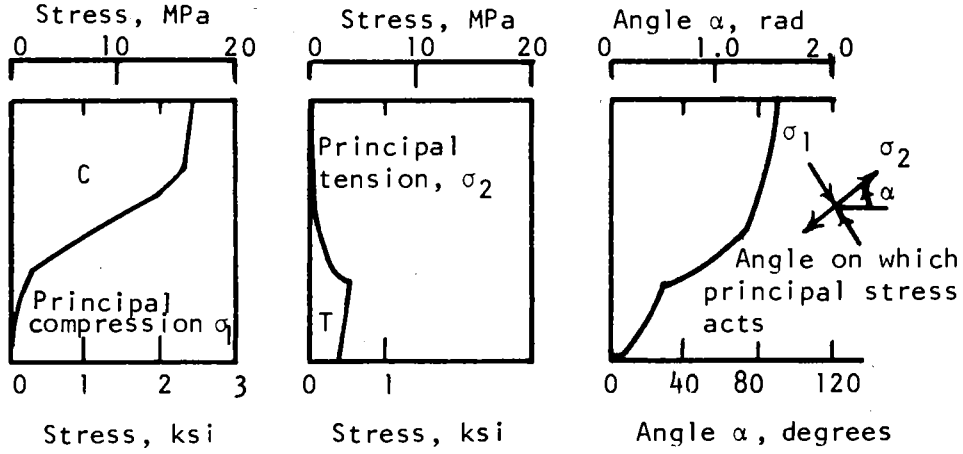

(c) Principal stresses at section (1)

FIGURE 5.7 STRESS DISTRIBUTION THROUGH THE SECTION FROM THE ANALYSIS

from cylinder tests was 2200 psi (15 150 kPa). Crushing of the concrete adjacent to the load spread beam was observed prior to failure of the liner.

The principal tension stress in Fig. 5.7(c) has a maximum value of about 500 psi (3451 kPa) and occurs at about 1.7 in. (43.2 mm) from the inside surface of the liner. This value is about equal to the modulus of rupture of the concrete (Table 2.2) and larger than the splitting tensile strength. Thus a possible diagonal tension failure is indicated, but the inclination of the actual failure surface does not agree with the plane on which the principal tension occurs. In the figure the plane of failure (perpendicular to the principal tensile stress) occurs at an angle of 63 deg, clockwise from the liner axis, while the measured angle for the test is about 25 deg.

This analysis is approximate and the conclusion that compression in the concrete caused the failure is tentative. However, the approach presented for using the principal stresses resulting from moment, shear and thrust at a section to predict failure appears feasible and allows the consideration of all internal forces at the section. The analysis described requires further refinement in order to describe the variation in moment, shear and thrust circumferentially around the liner.

5.3 CONCLUSIONS

The tests on circular liners provided good data on the overall behavior and failure mechanism of circular liners made of steel-fiber reinforced concrete. The measurements made during the tests provide an

adequate description of the overall response to external loads with a passive resisting mechanism, and they also allow the computation of internal forces. Therefore, these internal forces can be computed for the failure region and for other regions of distress to help define the conditions that cause failure. Duplicate tests for two widely varying concrete strengths also give reasonable assurance that the behavior observed during the tests are representative of the true behavior of this type of structure.

An analysis is needed that will accurately represent all aspects of the liner behavior including cracking, deformations and failure. Such an analysis would allow the study of both servicability and safety aspects of tunnel liners and parameter studies could be performed to determine the effect of the major variables that influence design. These variables include liner material properties, geometry of the liner and opening, and properties of the ground that provides the passive resistance. A more realistic ground loading rather than the test loading could then be used. These studies would allow the proportioning of liners on a more rational basis. The determination of stress-strain properties of steel-fiber-reinforced concrete and computation of moment-curvature curves described in Chapter 4 are an essential first step in the development of such an analysis that must allow the descending branch of the stress-strain curves, include the effect of geometry change, and permit the representation of interaction with a nonlinear passive resisting mechanism. The commercial programs available will not satisfy these requirements.

Conventionally reinforced and unreinforced liners cast with conventional concrete are used in practice, so the testing and analysis should

be extended to include them. Tests would provide data for comparing performance among the various types and verification of the analysis. The analysis could be used for parameter studies to help the designer select the best liner system for the conditions.

Randomly distributed steel fiber in the concrete mix adds some ductility and moment capacity to the liner section. This effect is not nearly as great as if the same steel were concentrated and properly oriented in the tension region of the section, but steel fibers provide other advantages of steel placement and concrete toughness. The procedure described to determine an equivalent stress-strain curve for a cracked beam element containing fibers is effective for determining section behavior which can in turn be used to determine overall structural behavior of a liner. The procedure is also useful for comparing various types and amounts of fibers among themselves and with conventional sections. It has been shown elsewhere that steel fibers in the mix increase the shear strength of conventionally reinforced beams so it is reasonable to assume that they also increase the shear capacity of liner sections with only steel fiber reinforcement.

Stiffness of the passive forces on the liner test specimen was the primary parameter influencing liner deformation. In turn the deformation strongly influenced the failure load. In the tests the failure loads for the strong and weak concrete specimens were similar though the strength differed by a factor of about 3. The strong concrete specimen did not resist a larger load because the passive stiffness was smaller by a factor of 5, allowing greater deformation. The influence of passive stiffness and concrete strength

on liner capacity are not related linearly, and a good nonlinear analysis is required to study the influence of all the important parameters throughout their practical range.

REFERENCES

"Building Code Requirement for Reinforced Concrete" (1971). ACI Std. 318-71, American Concrete Institute, Detroit, Michigan.

Herring, K. S. and Kesler, C. E. (1974). "Concrete for Tunnel Liners: Behavior of Steel Fiber Reinforced Concrete Under Combined Loads," University of Illinois at Urbana-Champaign, Report No. FRA ORDD 75-7 for Federal Railroad Administration, Department of Transportation.

Hognestad, E., Hanson, N. W. and McHenry, D. (1955). "Concrete Stress Distribution in Ultimate Strength Design," Journal of the American Concrete Institute, ACI, December; Proceedings, Vol. 52, pp. 455.

"NASTRAN User's Manual (Level 15)," (1972). Edited by C. W. McCormick, National Aeronautics and Space Administration, Washington, D. C., June.

Parker, H. W., Deere, D. U., Peck, R. B., Birkemoe, P. C. and Semple, R. M. (1973). "Testing and Evaluation of Prototype Tunnel Support Systems," Report No. FRA-ORDD 74-11, Federal Railroad Administration, Department of Transportation (Order No. PB-231-912/AS from NTIS).

Paul, S. L., Kesler, C. E., Gaylord, E. H., Mohraz, B., Hendron, A. J. and Peck, R. B. (1974). "Research to Improve Tunnel Support Systems," University of Illinois at Urbana-Champaign, Report No. FRA ORDD 74-51, for Federal Railroad Administration, Department of Transportation, PB-235-762/AS, June.

Pfrang, E. O., Siess, C. P. and Sozen, M. A. (1964). "Load-Moment-Curvature Characteristics of Reinforced Concrete Cross Sections," Journal of the American Concrete Institute, ACI, July; Proceedings, Vol. 61, No. 7, pp. 763.

☆ U.S. GOVERNMENT PRINTING OFFICE: 1976-211-173/485